

UNIVERSITÄT WÜRZBURG
FAKULTÄT FÜR PHYSIK UND ASTRONOMIE

DIPLOMARBEIT

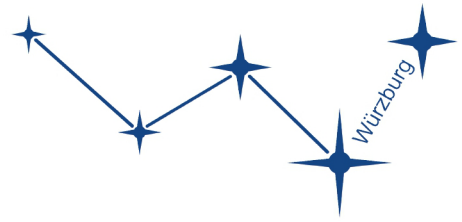
**Hard X-ray Properties of
Radio Selected AGN**

Autor:
Marcus Langejahn

Betreuer:
Prof. Dr. Matthias Kadler



Januar 2013



Hard X-ray Properties of Radio Selected AGN

Diplomarbeit

im Studienfach Physik

an der Julius-Maximilians-Universität Würzburg

vorgelegt von Marcus Langejahn,

geboren am 02. Oktober 1985 in Wernigerode

Verantwortlicher Hochschullehrer und Erstgutachter:

Prof. Dr. Matthias Kadler

Zweitgutachter:

Prof. Dr. Jörn Wilms

eingereicht am 15. Januar 2013

With increased distance, our knowledge fades, and fades rapidly. Eventually, we reach the dim boundary - the utmost limits of our telescopes. There, we measure shadows, and we search among ghostly errors of measurement for landmarks that are scarcely more substantial. The search will continue.

— *Edwin Hubble*

Zusammenfassung

In dieser Diplomarbeit wird die Röntgen-Charakteristik eines Samples von Aktiven Galaxienkernen (AGN) beschrieben. Die Quellen dieser Gruppe, die aus den 135 radio-lautesten AGN am Nordhimmel und zum Großteil aus Blazaren besteht, werden regelmäßig durch Radiointerferometrie mit langen Basislinien (VLBI) im Rahmen des MOJAVE-Programms beobachtet. Mittels eines harten Röntgen-Surveys über 70 Monate von *Swift*/BAT konnten aus den entsprechenden Spektren Informationen über die harten Röntgeneigenschaften der AGN abgeleitet werden. Die Erstellung der spektralen Eigenschaften von einem vollständigen Sample an Blazaren im Bereich von 20–100 keV wird in dieser Form zum ersten mal durchgeführt. Typischerweise sind Blazare in diesem Bereich durch eher schwache spektrale Energieverteilungen gekennzeichnet. Das direkte Fitten der Spektren war nur für 53 Quellen möglich, die hell genug sind bzw. genügend hohen Zählraten aufweisen. Für die Bestimmung der Flüsse und Leuchtkräfte der restlichen Quellen wurde bei der Berechnung der gemittelte Photonenindex der hellen Quellen adaptiert.

Neben dem Ergebnis, dass ein Großteil der MOJAVE-Quellen als harte Röntgenemitter eingestuft werden kann, werden die Fluss- und Leuchtkrafteigenschaften für die verschiedenen AGN-Unterklassen Quasar, Radiogalaxie und BL Lac aufgelistet. Wegen zu geringer Zählraten in den Spektren von 29 Objekten wurden diese mit konservativer Abschätzung als Upper Limits gekennzeichnet. Untersuchungen zu korreliertem Verhalten zwischen Radio- und Röntgenemission zeigen einen eher schwachen Zusammenhang für Flüsse, jedoch einen signifikanten für die intrinsischen Leuchtkräfte. Für die Klassen der Radiogalaxien und BL Lacs konnte nicht mit Sicherheit festgestellt werden, ob diese Korrelation ebenfalls existiert oder verworfen werden muss. Die Verteilung der Flüsse und Leuchtkräfte als Diagramm der Anzahldichte für Röntgen- und Gamma-Emission lässt darauf schließen, dass die vorliegende Gruppe von AGN starken Auswahleffekten seitens der Radioflüsse unterworfen ist.

Unter Einbeziehung von Photonenindices im Gamma-Bereich, gemessen von *Fermi*/LAT, konnte weiterhin festgestellt werden, dass die spektrale Position der Emissionskurve der inversen Compton-Streuung mit der Röntgenleuchtkraft korreliert. Dieses Verhalten bestätigt in erster Näherung das Modell der Blazar-Sequenz, welche auf diesem Weg das erste mal mit Röntgenleuchtkräften auf einem großen, radio-selektierten und vollständigen Sample von Blazaren beobachtet wurde.

Abstract

In this thesis the X-ray characteristics of a sample of Active Galactic Nuclei (AGN) are analysed. The sources of this sample, which are the 135 radio-loudest AGN in the northern hemisphere, are regularly monitored by Very Long Radio Interferometry (VLBI) as part of the MOJAVE program. The sample is mainly composed out of blazars. With the X-ray spectra, accumulated by the 70-month survey by *Swift*/BAT, basic properties of the sample in the hard X-ray regime were determined. Deriving the spectral properties of a complete set of blazars in the energy range of 20–100 keV is being conducted for the first time in this manner. Typically, blazars are characterized in this range by a rather weak spectral energy distribution. Spectral fitting was only feasible for 53 objects, which are bright enough or feature sufficiently high count rates, respectively. For the calculation of the fluxes and luminosities of the remaining sources, the averaged photon index of the bright sources has been adapted.

Beneath the result, that the majority of the objects in the MOJAVE-sample can be classified as hard X-ray emitters, the flux and luminosity characteristics are listed for the different AGN classes, i.e. quasars, radio galaxies, and BL Lacs. After a conservative estimation, the number of 29 objects from the sample were found to be flux related upper limits. A correlation analysis showed that the fluxes in the hard X-ray regime are only mildly correlated to VLBI radio fluxes, whereas significant correlations for the luminosities have been determined, except for the classes of radio galaxies and BL Lacs. The source count distributions for the different wavelengths of the sample suggest considerable selection effects regarding radio fluxes.

Using gamma-ray photon indices, measured by *Fermi*/LAT, it was determined that the position of the Inverse-Compton emission peak is correlated with the X-ray luminosity. In the first approximation this behaviour supports the model of the blazar sequence, which has been verified for the first time in a radio-selected complete sample of blazars.

Contents

1	Introduction	1
1.1	Active Galactic Nuclei	3
1.1.1	The Astronomical Object	3
1.1.2	The AGN Zoo	5
1.1.3	The Unification Model	7
1.1.4	AGN Surveys: Selections Effects	10
1.2	Radio Interferometry and MOJAVE	11
1.3	The <i>Swift</i> Satellite and its Instruments	11
1.3.1	Burst Alert Telescope (BAT)	12
1.3.2	X-ray Telescope (XRT)	14
2	Theory	15
2.1	Emission Processes in AGN	15
2.2	The Spectral Energy Distribution of AGN	17
2.3	Radio Jets and Relativistic Beaming	20
3	The AGN Sample(s)	23
3.1	The MOJAVE-1 Sample	23
3.2	The BAT Catalogues and Other X-ray Surveys	24
3.2.1	Previous and Concurrent Missions	24
3.2.2	BAT: 58 and 70 month catalogues	24
3.3	The <i>Fermi</i> /LAT Catalogues	25
4	Spectral Processing and Statistical Analysis	27
4.1	Spectral Fitting and X-ray Flux	27
4.1.1	Quality of the X-ray Spectra	27
4.1.2	Bright Sources	27
4.1.3	Faint Sources	29
4.2	X-ray Luminosity	30
4.3	Tests and Correlation Analysis	30
4.3.1	Two-Sample Kolmogorov-Smirnov Test	31
4.3.2	Correlation Coefficient and Partial Correlation	32
5	Results	35
5.1	MOJAVE Sources as Hard X-ray Emitters	35
5.2	Hard X-rays: Statistical Properties of the Sample	38
5.2.1	Photon Indices Γ	38
5.2.2	X-ray Flux and Redshift Distribution	39
5.2.3	X-ray Luminosity	39
5.3	Correlation Studies	42
5.3.1	Radio and X-ray Flux	42
5.3.2	Radio and X-ray Luminosity	44
5.3.3	Jet Velocity and Luminosity	50

6 Discussion	51
6.1 Spectral Shape and Photon Index	51
6.2 X-ray Flux and Luminosity Distribution	52
6.3 Source Count Statistics	54
6.3.1 Log(N)-Log(S) Distribution	54
6.3.2 Log(N)-Log(L) Distribution	57
6.4 Luminosity Dependence of Blazar SEDs	58
7 Conclusion and Outlook	65
A Graphs: Radio and Hard X-ray Relations	67
B Hard X-ray Data for the MOJAVE-1 Sample	71
C Partial Kendall's Tau - SLANG Program	79
D BAT Spectra of the MOJAVE-1 Sample	85
List of Figures	109
List of Tables	111
References	113

1 Introduction

THE first question one could ask is: Why are we even interested in astronomy? Why do we explore the sky and the space, that is almost unreachable for everyone of us? It is because there is far more to see, learn and discover than the few blinking lights in the night sky could seem to offer. The last one hundred years brought us a huge leap forward in this oldest of all natural sciences. Constantly evolving theories together with scientific tools pushed the boundaries of our world view over and over.

The eye, our very own "photon detector", gave us a small glimpse of this first section of the broad electro-magnetic spectrum that was perceived and studied - the optical regime. Since the time of Galileo Galilei and his first scientific observations larger and better telescopes permitted us not only to look deeper into space and into earlier stages of the universe, but also did allow us to see fundamental physical processes under their most extreme conditions. Being an accidental discovery by Karl G. Jansky in 1933, the radio emission of the Milky Way and distinct sources within it widened our perception of the sky that could be seen literally in a different light.

Due to various mechanisms of absorption and scattering of electro-magnetic radiation by the earth's atmosphere, only a small part of the spectrum can be observed, i.e. the optical, certain windows of the infra-red and a large part of the radio regime. Observations throughout the entire infra-red are only possible in places of great height and dryness. Measurements of the remaining parts of the spectrum have to be taken on by other means. This is why the major part of the high energy regime of electro-magnetic waves is being observed by space-borne instruments. Starting in the 1970s, X-ray astronomy satellites began observing sources within and beyond the Milky Way. Current very successful X-ray missions are for instance the *Chandra X-ray Observatory* (Weisskopf et al., 2000) and *Swift* (Gehrels et al., 2004), both launched by NASA, as well as the European satellite *XMM-Newton* (Jansen et al., 2001). Observations in the gamma-ray regime can (for different energy intervals) either be conducted from the Earth's surface, measuring Čerenkov radiation from the atmosphere, or from space with instruments like *INTEGRAL* (Winkler et al., 2003) and *Fermi/LAT* (Atwood et al., 2009).

The reason why studies of the sky at various wavelengths are being done is simple. When we look at the sky at different energies, we can see that all astronomical objects look differently throughout the whole spectrum. Figure 1.1 shows the Milky Way, seen at radio and X-ray wavelengths, illustrated in Galactic coordinates. The upper picture was taken at 408 MHz (Haslam et al., 1982), the lower is a composition of three X-ray bands of the ROSAT PSPC All-Sky Survey between 0.1 and 2.0 keV (Freyberg & Egger, 1999). We see different regions of the sky radiating at different energies. The most prominent feature being the Galactic plane in the middle, one notices several smaller regions and objects that radiate more intensely at certain wavelengths. Since the whole spectrum, from the lowest detectable radio frequencies to the very-high energy band of gamma-rays, spans from μeV to TeV, different observations at specific frequencies account for sometimes radically different physical processes. Using simultaneous multi-wavelength measurements of astronomical objects tells us a great amount of information regarding the nature of the object.

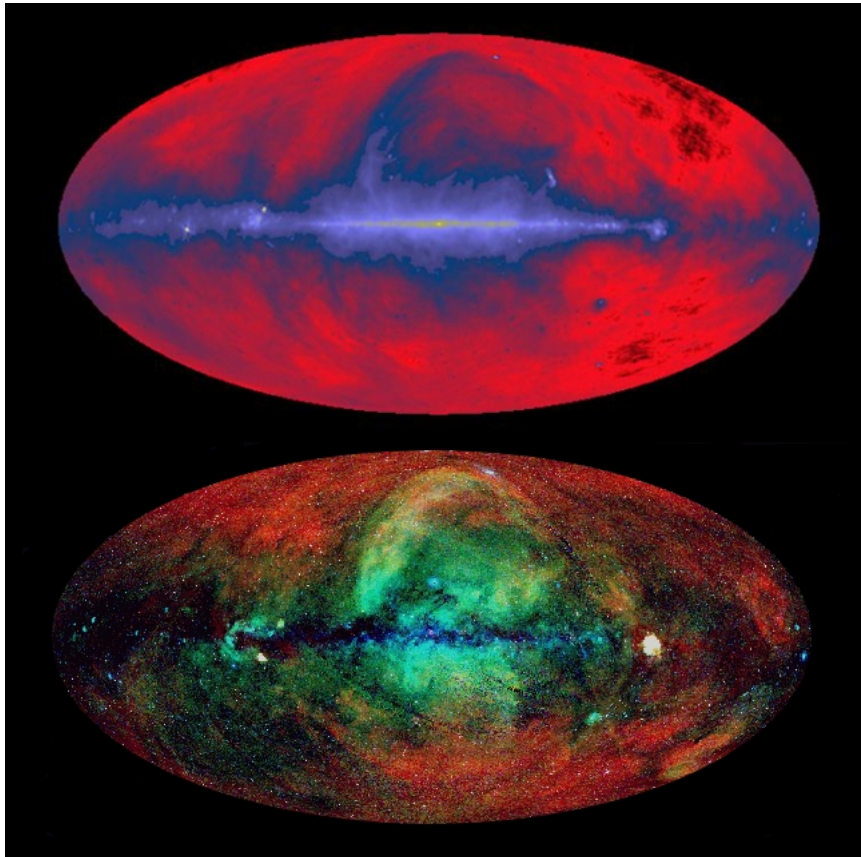


Figure 1.1: The sky in Galactic coordinates. Upper picture: radio survey at 408 MHz (Haslam et al., 1982). Lower picture: ROSAT PSPC All-Sky Survey of 0.1-0.4 keV (red), 0.5-0.9 keV (green) and 0.9-2.0 keV (blue) (Freyberg & Egger, 1999)

One of the most fascinating and yet enigmatic phenomena in astronomy that has been focussed on by entire multi-wavelength campaigns for some decades now are the Active Galactic Nuclei (AGN), including the most luminous and farthest objects ever detected. Their astounding ability to emit enormous amounts of energy and matter at relativistic velocities made them one of the most interesting and important research topics in modern-day astronomy. Estimations show that about 10% of all galaxies are AGN (Peterson, 1997).

Because of their great distances, the detailed structure of the majority of all AGN cannot be observed. Although using radio interferometry with long baselines, for certain objects it is possible to create resolved images on scales of milli-arcseconds. One of the largest observing programs using the radio telescopes of the Very Long Baseline Array is the MOJAVE program (Lister & Homan, 2005), short for Monitoring Of Jets in Active Galactic Nuclei with VLBA Experiments. Its aim is the long-term monitoring of a sample of relativistic jets associated with AGN. Trying to understand such a complex and intriguing class of objects requires to analyse and compare the measurements in the different wavelength regimes.

In this thesis, a comparative analysis of various observed properties of the first MOJAVE sample (135 objects) is done using radio and hard X-ray data. The latter are provided by spectra taken by the Burst Alert Telescope BAT (Barthelmy et al., 2005) of the satellite *Swift*, launched by NASA in 2004. One of *Swift's* main objectives is the search for Gamma

Ray Bursts (GRB) via the continuous survey of the sky at high energy levels. The detecting range of the coded mask system BAT lies within 14-195 keV, providing hard X-ray spectra accumulated over years.

With the results of the analysis, a complete data set of hard X-ray fluxes and luminosities can be presented for the first time for the statistical complete MOJAVE sample. This builds the basis for further correlation studies of the sample, which consists largely out of blazars, highly variable sources. The discussed issues include current research topics like the relation of apparent jet velocity to luminosity in different energy bands and the systematic behaviour of the spectral shape of blazars depending on luminosity, i.e. the blazar sequence.

The following chapter is based on textbooks by Krolik (1999), Schneider (2008), and Kitchin (2007), as well as the introductory lecture *Extragalactic Jets* (Kadler, 2012).

1.1 Active Galactic Nuclei

1.1.1 The Astronomical Object

When we look at the spectra of normal galaxies, we see the result of thermal emission from the stars' atmospheres which are essentially in thermal equilibrium. The temperature of the most stars of a galactic population varies from about 3000 K to 40000 K. Hence, the measured "normal" galactic spectrum can be described as an overlay of Planck spectra in the first approximation. Because Planck spectra have a relatively narrow distribution around their maximum value at $h\nu \sim 3k_B T$, the spectrum of the galaxy is basically limited from about 4000 Å to 20000 Å.

Active Galactic Nuclei, in the following abbreviated by AGN, possess a much broader energy spectrum. Some AGN show significant emission from the radio up to the very-high energy gamma-ray regime, which is explained by non-thermal emission (Sect. 2.1). There are various properties that define the term AGN, although not all objects show all features. One of their main properties is the very small angular size. AGN often rival or surpass the measured flux of their hosts, although depending on wavelength and the specific object.

AGN possess a luminosity of about $10^{42} - 10^{48} \text{ erg s}^{-1}$, which ranges from 0.01 to 10^4 times the luminosity of a typical galaxy. However, it has to be taken into account that Active Nuclei with much lower luminosity than their galaxy are more difficult to detect than their bright counterparts. On the other hand, obscuration of the nucleus by dust as well as relativistic beaming (see Sect. 2.3) interferes with a more or less simple isotropic picture of a light emitting galactic centre. A photograph of a well observed example of the nearby AGN NGC 4151 is shown in Fig. 1.2 (Morgan, 1968). The three photographs of increasing exposure time demonstrate the difference in luminosity to the host galaxy.

Beneath their continuum spectra which can easily be distinguished from normal galaxies, AGN exhibit very prominent emission lines which often have equivalent widths of $\sim 100 \text{ \AA}$. The observed lines are remarkably unique from one object to the other. Almost every time emission lines are observed, we see Ly α , the Balmer series, several weaker lines and often the FeK α line in the X-rays near 6.4 keV. Regarding the distribution of line widths, there are objects that have lines with broader and narrower wings, corresponding to several thousand to few hundred km s^{-1} , respectively (Schneider, 2008).

Another typical feature of AGN is their variability. Most AGN show small optical variability of about 10% on large time scales such as years, whereas the variability amplitude

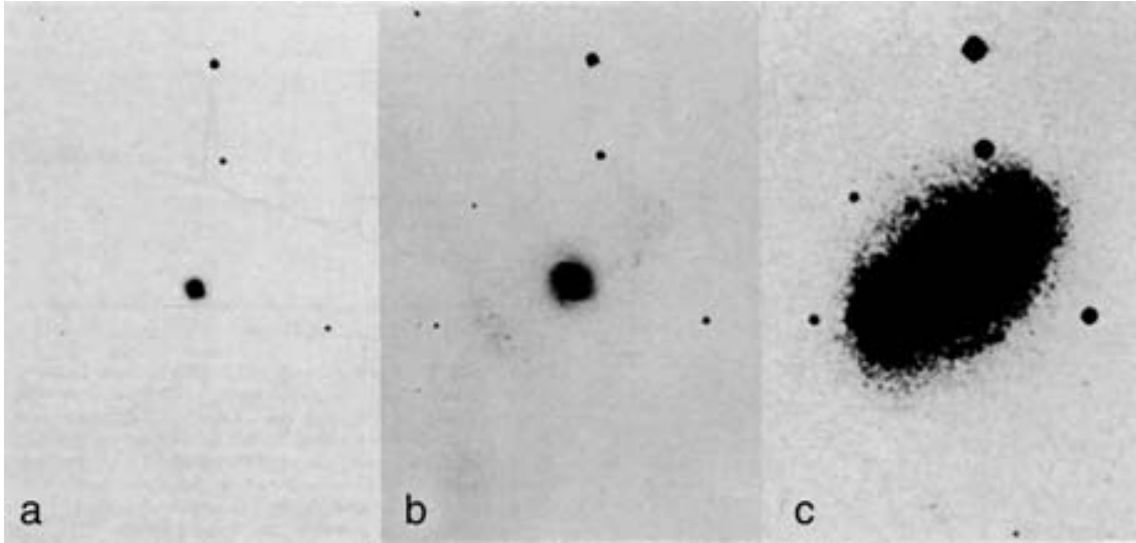


Figure 1.2: Photographs of the Seyfert Galaxy NGC 4151, increasing exposure time from left to right (Morgan, 1968).

increases towards shorter wavelengths, whereas different AGN types exhibit typical variability timescales (Ulrich et al., 1997). A small number of AGN even feature fluctuations on the timescale of days (Hartman et al., 2001). When determining the variability or variance of a lightcurve the result strongly depends on the timescale and the sampled intervals. Hence, the corresponding amplitude can be very difficult to measure. Correlated properties of highly variable AGN are a compact radio structure, strong high-energy gamma-ray emission and strong polarization.

Historically, the first characteristic attribute of AGN, their strong radio emission, was detected to originate from these objects and in some cases from double lobes on each side of the galaxy itself. The cause for this phenomenon was seen as a non-stellar process (Krolik, 1999). In the early 1950s, large radio telescopes were built and the first catalogue, the 3C catalogue (Bennett, 1962) containing about 500 objects detected at 178 MHz and brightnesses greater than 9 Jy, was assembled. In 1963 the Dutch astronomer Maarten Schmidt realized that one of these radio sources by the designation of 3C273 and associated with a bright point source had a very high redshift of 0.158 Schmidt (1963). From this point on, the optical sources that were associated with sources of the 3C catalogue became astronomical objects whose spectra could be analysed and their distances and luminosities determined.

Until today, radio astronomy represents a cornerstone and a vital tool for AGN observation. Only in the radio regime, milliarcsecond imaging via interferometry techniques (see Sect. 1.2) is available at this moment, which allows us to make the highest resolved images of the inner parts of active galaxies. Current efforts in the (sub)millimetre wavelength region are carried out using the Atacama Large Millimeter/submillimetre Array (ALMA). Among other goals it will be one aim of this new instrument to image detailed kinematics of obscured AGN and quasars on scales of 10 to 100 pc which will help testing emission models of Seyfert Galaxies (Casasola & Brand, 2010).

However, samples of astronomical objects, AGN in this case, are always subjected to detection biases. This becomes crucial when detecting different AGN types in surveys in

different energy ranges. The fact, that only about 1% of the bolometric luminosity and often significantly less is due to radio emission, demands the involvement of studies at other wavelengths. With the help of space-borne instruments, X-ray astronomy allows us to take another approach to the detection and understanding of AGN.

1.1.2 The AGN Zoo

Various subclasses of AGN have been defined that differ in a number of properties such as radio loudness or width of the emission lines. Many of these classes and their names come from a historical point of research. It has to be emphasized that the following categories do not necessarily represent the entire list of Active Galactic Nuclei that may exist.

Quasars. "Quasi-stellar radio sources" were the found by identifying sources of radio emission with point-like optical objects. Regarding the fraction of radio to optical luminosity, one distinguishes radio-loud and radio-quiet quasars (Kellermann et al., 1989). Both types emit electro-magnetic radiation throughout the entire spectrum and feature flux variability at almost every frequency. The optical band is very blue with broad emission lines while the overall continuum spectrum can often be described in intervals via a simple power-law (see Sect. 2.2). The complex radio morphology depends on the observed frequency and shows a compact source and the two radio lobes on each side. In many cases the lobes are connected to the central component by a narrow jet which is assumed to transport matter and energy towards the lobes. In radio images, those structures can measure up to 1 Mpc (Schneider, 2008).

Radio Galaxies and Fanaroff-Riley Classification. These (elliptical) galaxies were the first sources, that could be associated with optical sources in early radio surveys. They can be categorized into galaxies with broad emission lines (Broad Line Radio Galaxy, "BLRG"), and without them (Narrow Line Radio Galaxy, "NLRG").

Following Fanaroff & Riley (1974), widespread radio sources can be sorted into two groups: Galaxies of the Fanaroff-Riley type I (FR I) are brightest near the center and the surface brightness decreases with distance from it. Their typical luminosities amount to $L_\nu(1.4 \text{ GHz}) \lesssim 10^{32} \text{ ergs}^{-1} \text{ Hz}^{-1}$. In contrast, the surface brightness of FR II increases going from the inner to the outer parts. With luminosities of $L_\nu(1.4 \text{ GHz}) \gtrsim 10^{32} \text{ ergs}^{-1} \text{ Hz}^{-1}$ they are significantly brighter than FR I galaxies. Both types possess jets that end in radio lobes. Figure 1.3 shows the exemplary objects M84, a FR I type (left panel) and 3C175 (right panel) a FR II type AGN. If both jets are visible, one is often relatively weak and called the "counter-jet". The huge difference in brightness of jet and counter-jet is caused by relativistic beaming and greatly influenced by the angle towards the observer. Since the intensity of the components differ due to diverse spectral indices, radio catalogues are highly biased towards the observed frequency.

QSOs. Since quasars feature a very blue optical spectrum, the search for these objects was also approached by looking for point-like sources with a very blue color index. The results of photometric surveys showed that the majority of found sources held no or only little radio emission. Hence the name "quasi stellar object" or QSO, which are the most luminous group

¹see also <http://www.jb.man.ac.uk/atlas/other/3C272P1.html>

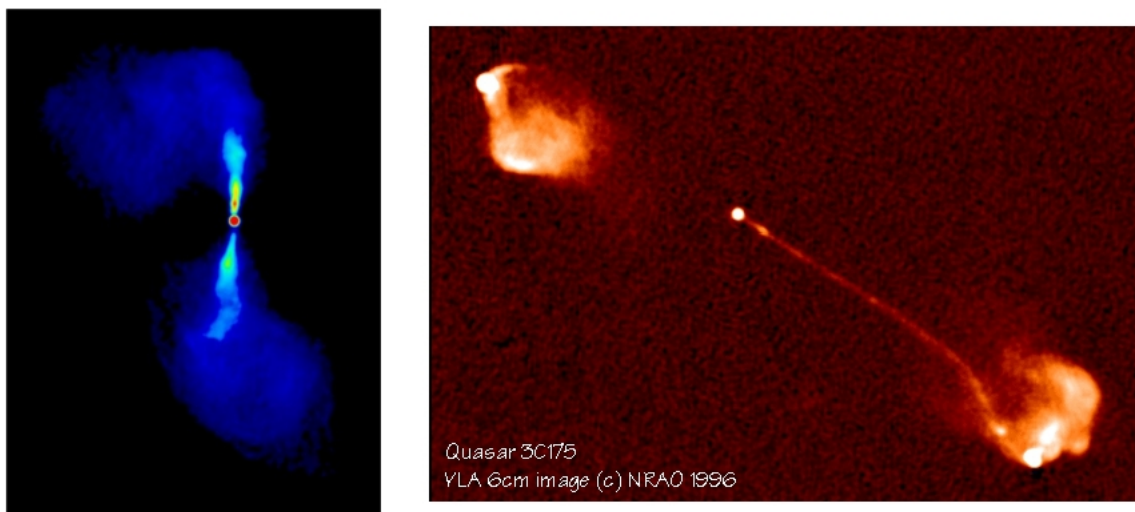


Figure 1.3: Radio image at 6 cm: M84 (left panel), Laing & Bridle (1987)¹; 3C175 (right panel), Credit & Copyright: Alan Bridle (NRAO Charlottesville).

of AGN and are able to overshadow their host galaxy. When differentiating quasars on the basis of radio emission, QSOs are also called radio-quiet quasars which account for about 90% of that population (Kukula et al., 1998).

Seyfert Galaxies. The AGN class that has been discovered first was the group of Seyfert Galaxies, although much less luminous than the bright QSOs. Historically, the first thing that was noticed about Seyfert galaxies were the emission lines that were very similar to those of a planetary nebula (Seyfert, 1943). The original selection criteria - a small very bright nucleus and a spectrum containing strong, broad emission lines - still provides the basic definition of this group. There are two main types of Seyfert galaxies: type 1 and type 2, as well as several classes in between with mixed properties. The hydrogen and other allowed lines in the spectra of Seyfert 1 galaxies are wide, corresponding to Doppler broadening velocities of up to 10 000 km/s. The forbidden lines are with ≤ 1000 km/s much narrower but are still significantly broader than in normal galaxies. Overall, the optical spectra of Seyfert-1 galaxies are very similar to that of QSOs. This distinction is conditioned historically and the only basic difference is core luminosity.

Blazars. The designation blazar summarizes radio-loud objects showing nuclear emission from structures on the scale below arcsec as well as large and rapid variability. This group includes three subclasses of sources: BL Lacertae objects (BL Lac), Optically Violent Variables (OVV), and Flat-Spectrum Radio Quasars (FSRQ). The name of the first source type is derived from the object BL Lacertae (2200+420), which has first been falsely classified as a star. In many cases BL Lacs show no emission lines above the continuum. Hence, it can be difficult or even impossible to determine a redshift for a BL Lac. The optical spectrum of BL Lacs is highly polarized (Vermeulen et al., 1995, and references therein). In some cases, the optical luminosity can vary by several magnitudes over years. Within a phase of low luminosity, emission lines may be observed so that the BL Lac appears as an OVV,

which also shows weaker radio emission than BL Lacs. Beneath their optical luminosity, the emission varies at other frequencies as well, with shorter time scales and higher amplitudes towards higher frequencies, up to highly energetic and erratic gamma-ray emission (Schneider, 2008). BL Lacs can further be divided according to the position of their spectral peaks (see Sect. 2.2). The group of FSRQs can be described as a more luminous version of BL Lacs with broad emission lines.

LINERs. These galaxies, dubbed "Low-Ionization Nuclear Emission Region" can also be divided into type 1 and 2 objects, that are found relatively nearby. LINERs of type 1 have strong H α and possibly other Balmer lines in their optical spectra and are powered by low luminosity AGN. Type 2 LINERs are likely to have more than one sort of energy source. While some objects show evidence of the presence of an AGN, others are seen to be powered by stellar processes (Terashima & Wilson, 2003). LINERs also show hardly any variability and even no radio emission.

1.1.3 The Unification Model

All mentioned classes of Active Galactic Nuclei partially share common observational features and can also be radically different in some of their characteristics at the same time. The different types have been classified on the basis of phenomenological properties. In the past decades it has been a large effort to develop a model, that describes all types in equal measure while being elegantly simple. The following scheme of the Unified Model of AGN is based, among others, on works by Antonucci & Miller (1985), Antonucci (1993), Lawrence (1987) and Urry & Padovani (1995).

The approach for a universal physical model for AGN distinguishes between radio-loud and radio-quiet objects. Both models share a major part of components. The following description of the AGN structure is also illustrated in Fig. 1.4. Active galactic nuclei emit a very high amount of energy all throughout the spectrum.

An explanation for the extraordinary energy output by stars or supernovae is not feasible. The most efficient way of releasing energy by radiation is by accretion of massive amounts of matter (i.e. gas and dust) onto a central object as for example discussed by Salpeter (1964) or Zeldovich (1964). This idea is realized by a super massive black hole (SMBH) with masses of about $10^6 - 10^9 M_{\odot}$ in the center of the active galaxy, surrounded by a hot accretion disk with a radius $r \approx 10^{-3}$ pc. The relatively thin disk is embedded in a hot gas with $T \approx 10^9$ K called corona. Outside of the accretion disk, at $r \approx 0.01 - 0.1$ pc the Broad Line Region (BLR) is located. It is composed out of dense, fast moving gas clouds. The designation BLR is assigned due to the model assumption that observed spectra with highly broadened lines (Doppler broadening because of high velocities) must originate from this part of the nucleus. The previous components are surrounded by a large dust and gas torus with a radius to the SMBH of $r \approx 1$ pc up to the order of a few 10 pc and relatively low temperature. Below and above this rotationally symmetric structure, the Narrow Line Regions (NLR) are located more distant at about $r \approx 100 - 1000$ pc. The medium in these regions is characterized by low velocities in the order of a few 100 km s^{-1} as opposed to a few 1000 km s^{-1} in the BLR, resulting in significantly narrower emission lines.

The difference between the radio-quiet and radio-loud AGN is the existence of a massive particle outflow from the SMBH, perpendicular to the plane of the accretion disk, called

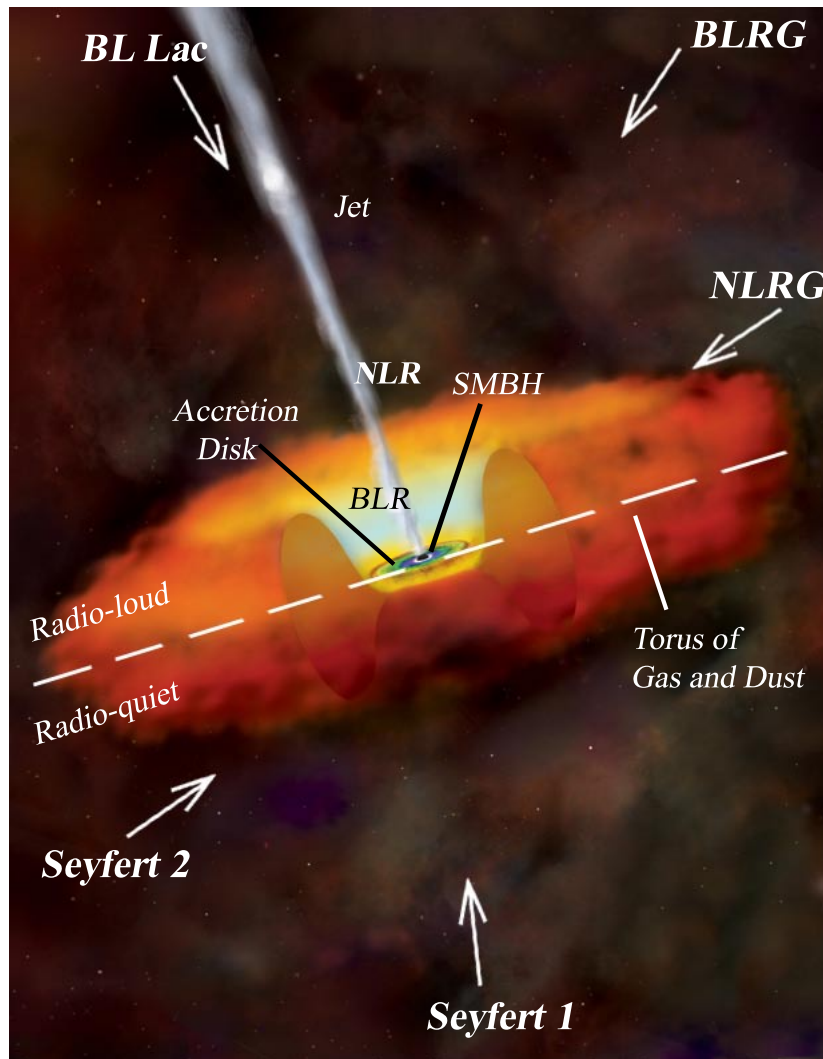


Figure 1.4: Unification model for radio-loud (upper side) and radio-quiet AGN (bottom side). Labels indicate the AGN components and the definition of the AGN type depending on the viewing angle. Adapted from NASA/CXC/M. Weiss.

jet. This structure is detectable at wavelengths from radio up to X-rays, whereas different emission processes are responsible (see Sect. 2.1). Jets always exist in pairs, i.e. a jet and counter-jet above and below the nucleus, respectively. Through relativistic beaming effects (Sect. 2) the jet is greatly increased in luminosity while the counter-jet is only visible when facing the AGN nearly edge-on, called a two-sided jet morphology. Otherwise one speaks of a one-sided jet. At the end of each jet, large and often asymmetric radio lobes are formed by the interaction with the intergalactic medium.

Figure 1.5 shows a vivid example of the large-scale morphology of a radio-loud AGN. The left panel shows a composite image of optical and radio measurements of the FR I radio galaxy NGC 4261 on a scale of about 3×10^4 pc. The radio jets and lobes are depicted in orange and red, easily distinguishable from the galaxy itself. The right panel provides a zoomed-in view of the central region of the galaxy, observed by the *Hubble Space Telescope*

(HST). Inside the bright ring, which is composed out of stars, a dark absorbing disk with a diameter of about 130 pc is located. Although not direct evidence of a torus surrounding the inner region of AGN, it shows that in the center of AGN disks can form.

This AGN model is able to explain the general properties of the phenomenological determined AGN types simply by taking into account the angle at which the AGN is observed. One defines the inclination angle of an AGN as the angle between the normal of the accretion disk/torus and the line of sight of the observer. For larger inclination angles (edge-on view), the dust and gas torus obscures the radiation from the centre up to the X-ray regime and the BLR, respectively. The differentiation of BLRG and NLRG as well as Seyfert 1 and Seyfert 2 for the radio-quiet AGN now becomes a simple matter of low or high inclination angle. The division into two types for both radio galaxies and Seyferts dependent on emission line width is explained by the obscuration of the BLR by the torus. Depending on the absorption of radiation it can be roughly estimated how large the inclination angle is, together with further parameters like the density of the torus or the metal abundance. Furthermore, Type 1 (small inclination angles) and Type 2 AGN (large angles) both feature "forbidden" emission lines, that are not strictly forbidden, but only can be observed from a low density medium (NLR). Figure 1.4 also shows the viewing angle under which the AGN is classified. Quasars and QSOs belong to the radio-loud and radio-quiet AGN model, respectively. The class of blazars however are explained by taking into account another component: the jet itself. Since blazars feature a great measure of variability, they are thought to be observed under very small inclination angles for the jet is not a static but itself a very dynamic and complex structure (e.g. Lister & Homan, 2005).

When being confronted with the issue of compiling AGN surveys, one has to take into account that weakened radiation from optical up to soft X-ray wavelengths may lead to strong biases in the detection process. A much more suitable way to obtain an unbiased survey of these sources is a hard X-ray survey above an energy of about 10 keV. Furthermore, it has been shown (Madau et al., 1994; Hasinger & Zamorani, 1997), that the observed 30 keV bump in the Cosmic X-ray Background (CXRB) can be explained by a large population of highly absorbed AGN, which also amount to about the half of all AGN (Gehrels et al., 2004).

However, the described AGN model only works as a first general approach and is not account for all characteristics that have been observed. Bianchi et al. (2012) argue, that the model of a simple toroidal shaped obscuring medium is not sufficient. Instead, the obscuring material must be distributed on smaller and larger scales than a torus surrounding the BLR. The hypothesis of a uniform distribution of the obscuring material has been replaced by a more clumpy structure of the medium in many newer models which are strongly supported by X-ray observations. An analysis of a sample of nearby AGN showed for example variations the column density N_H for a majority of Seyfert galaxies. Therefore, the circumnuclear absorber has to be of clumpy structure (Risaliti, 2002; Bianchi et al., 2012). Hard X-ray observations by early missions like *Exosat*, *ASCA*, and *BeppoSAX* implied nevertheless a model of a central engine with absorbing material in the line of sight (e.g. Smith & Done, 1996; Turner et al., 1997; Maiolino et al., 1998). Although more complex models for AGN will be developed in the near future, the simple picture of the AGN structure as described here will be of sufficient use for this work.

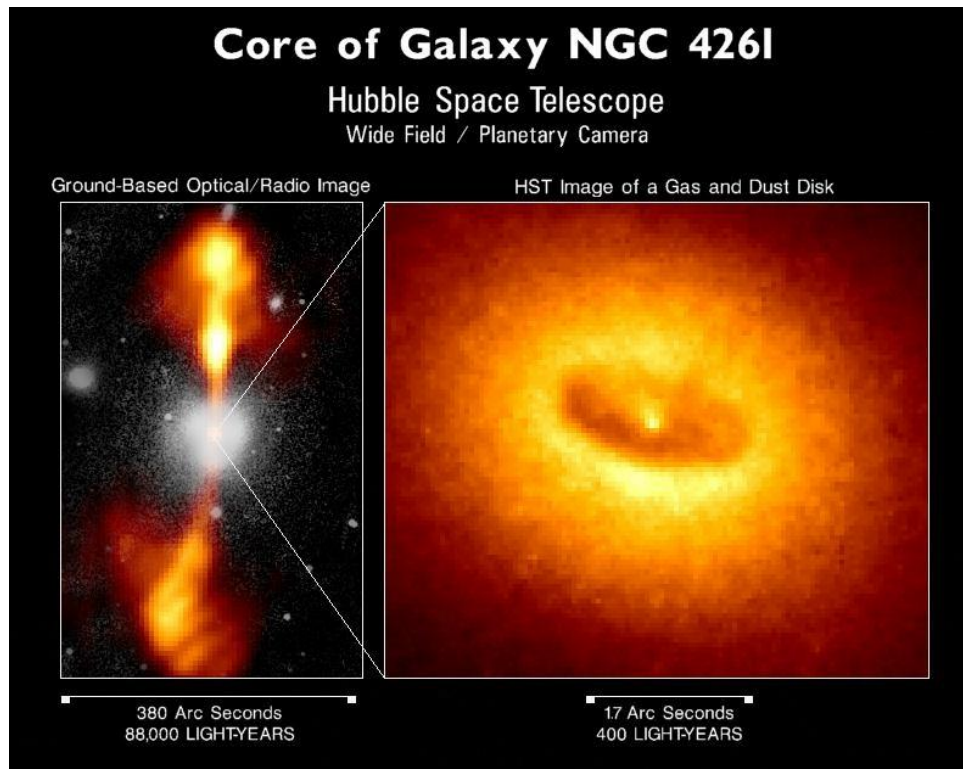


Figure 1.5: FR I radio galaxy NGC 4261 as a composite image of optical and radio (orange jets and lobes) observations (left panel), and an image taken by the HST of the core region (right panel). The darker inner region is surrounded by a ring of more luminous stars. Image credit: NRAO, Caltech, Walter Jaffe / Leiden Observatory and Holland Ford/JHU/STScI/NASA

1.1.4 AGN Surveys: Selections Effects

All surveys of AGN are subjected to selection effects. Observational biases occur especially for sources with complex spectral energy distributions and variability such as AGN, creating considerable differences between samples that have been assembled for different frequencies, observed areas, time intervals, lower flux limit, and a couple of other instrument-based factors. Although no measurement at a specific energy range is able to obtain an all-inclusive list of AGN, it is always desirable to obtain samples that are as complete as possible.

One important effect that has to be taken into account for the results of this work follows from the combination of measurement errors and the method of the sample selection. If the measured observable, after which the sample is selected, is correlated with the quantity whose distribution is sought, then for the latter one an effect called Malmquist bias may apply. This bias (Malmquist, 1922), applied to the issue of measured flux values and the derived distribution of luminosities, is created by the preferred detection of bright sources at large distances, while faint sources are not detected at all if they are below the flux detection threshold of the observation. This leads to a distribution of too few low-luminosity objects with increasing distance to the observed sources or volumes, respectively. A more detailed discussion of this effect can be found in Landy & Szalay (1992).

1.2 Radio Interferometry and MOJAVE

The setup of modern radio detectors for astronomical purposes differs regarding the observation wavelengths. Instruments for long wavelengths are realized by large dipole antennas and operate in the MHz regime, such as the recently build Low Frequency Array (LOFAR). Higher energies, that correspond to GHz frequencies, are typically measured by a movable parabolic dish that focusses the radio emission into the receiver. Since the angular resolution θ depends on the wavelength λ as well as the used diameter D , also known as the Rayleigh criterion

$$\sin(\theta) \approx 1.22 \frac{\lambda}{D} \quad (1.1)$$

one can easily determine, that the resolution of a 100 m dish at 15 GHz is about 1 arcmin, which about equals the resolution of the naked eye in the optical regime. A huge improvement in the fields of radio astronomy was the mechanism of interferometric measurements by an array of telescopes. Currently operating radio arrays are for example the EVLA in New Mexico, USA, or the newly-build Atacama Large Millimeter/Submillimeter Array (ALMA) in Chile. The worldwide largest arrays span over more than an entire continent. This arrangement of instruments is also called Very Long Baseline Interferometry (VLBI). The very successful Very Long Baseline Array VLBA (Kellermann & Moran, 2001), with ten technically identical antennas distributed over the USA, possesses a maximum baseline of about 8000 km. As a result, one obtains a radio telescope with virtually the diameter of this longest baseline. Even though the "missing" telescopes in between create disturbing effects that have to be accounted for, the resulting resolution of milli-arcsec is the highest ever achieved with any kind of instrument (e.g. Müller et al., 2011).

This work characterizes hard X-ray properties of a radio-selected sample of AGN, which is defined as the 135 brightest/loudest active galaxies and jets at 15 GHz on the northern hemisphere. The sample is being monitored by the MOJAVE² program (Monitoring Of Jets in Active Galactic Nuclei with VLBA Experiments). For the exact definition and further properties of the used sample see Sect. 3.1. MOJAVE is a large VLBA program for investigating the statistical properties of AGN jets (Lister & Homan, 2005). Sources are being observed regularly on time scales from a few months to a year. Via interferometric observations it is possible to track individual jet components over longer time periods and measure polarization and the distribution of spectral indices along the jet.

1.3 The Swift Satellite and its Instruments

The following section regarding *Swift*, its mission and observation scheme, its technical specifications as well as a description of the scientific instruments onboard *Swift* is based on The *Swift* Technical Handbook, Version 4.1³ and The SWIFT BAT Software Guide (Markwardt et al., 2007).

The main purpose of the *Swift* mission (Gehrels et al., 2004) is the study of gamma-ray bursts (GRBs) with three instruments that each observe a different wavelength range from the lower gamma-ray to the soft X-ray and UV/Optical regime. As part of NASA's Medium-Class-Explorer program, *Swift* was launched in November 2004 into a low-Earth

²<http://www.physics.purdue.edu/astro/MOJAVE/>

³<http://heasarc.nasa.gov/docs/swift/proposals/appendix.f.html>

orbit. The search for GRBs is triggered by the detection of the Burst Alert Telescope BAT (Barthelmy et al., 2005), that pinpoints the detection in its large observational field within $1' - 4'$. Consequently, the satellite slews into the observed direction, so that all instruments can begin the measurement, providing SEDs and light curves for the afterglow of the burst. This process works autonomously and interrupts the normal observation schedule. Beyond the study of GRBs, another aim of the *Swift* mission is a hard X-ray survey of the sky. The two X-ray instruments XRT (Burrows et al., 2005) and BAT are described further in the following subsections. The third instrument, the Ultraviolet/Optical Telescope UVOT (Roming et al., 2005), is co-aligned with XRT and operates in the wavelength range of $1600 \text{ \AA} - 6000 \text{ \AA}$.

1.3.1 Burst Alert Telescope (BAT)

The BAT is large field-of-view telescope with very high sensitivity, designed to monitor a large part of the sky for GRBs. While observing GRBs, BAT automatically accumulates data for a hard X-ray survey. Instead of a focussing X-ray optics system, which telescopes like XRT or *XMM-Newton* are using, BAT utilizes a coded mask aperture system on top of the 5200 cm^2 large detector array. However, the entire detector is never fully exposed to one source, due to the coded mask, which consists of a random and unique pattern of 50% open and obscuring $5 \times 5 \text{ mm}^2$ lead elements on an area of 2.7 m^2 . The idea behind a coded mask system is that every source in the field-of-view (FOV) leaves a shadow pattern of the mask on the detector can be reconstructed due to the uniqueness of the X-ray obscuring pattern (see Fig. 1.6). This procedure is additive for multiple sources and results in a very large FOV for the expense of resolution. The setup realized in BAT has a point spread function (PSF) of $22'$ and a half-coded FOV of 100° by 60° or 1.4 sr . A schematic cut-away view of the instrument is shown in Fig. 1.7.

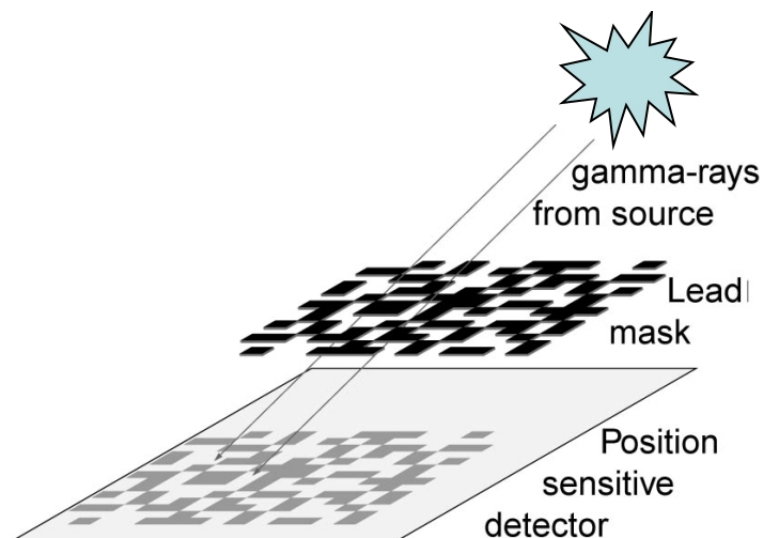


Figure 1.6: Principle of the coded mask aperture system. Incoming gamma-rays / hard X-rays leave a characteristic shadow pattern on the detector. Image credit: Markwardt et al. (2007).

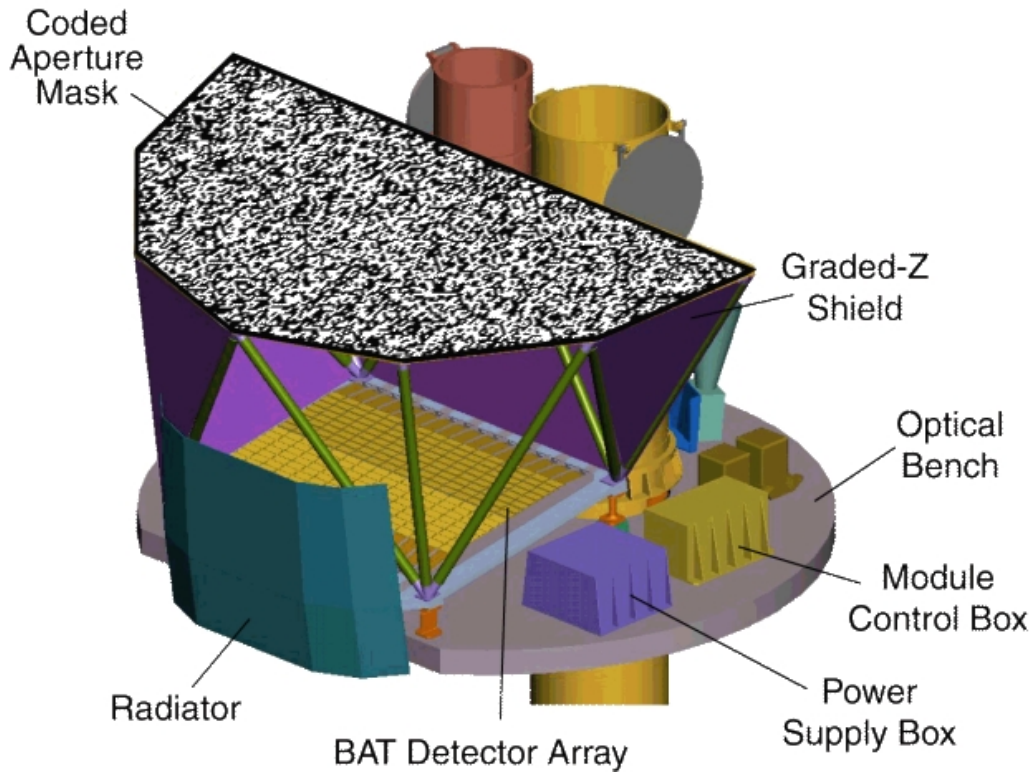


Figure 1.7: Cut-away view of the BAT with the coded aperture mask on top of the detector array. The instruments XRT and UVOT are mounted on the side of BAT (Markwardt et al., 2007).

The detector pane itself is composed of 32,768 elements of CdZnTe (CZT) with each the size of $4 \times 4 \text{ mm}^2$ and thickness of 2 mm, forming a sensitive area of $1.2 \times 0.6 \text{ m}$. Groups of 128 elements are assembled into arrays the size of 8×16 . Two of these arrays are grouped into detector modules, which are further grouped into eight blocks. Due to this hierarchical structure and the forgiving principle of a coded mask system, the loss of individual pixels as well as complete modules can be tolerated while keeping the ability to survey and detect bursts and their positions, although with a decrease in sensitivity. The detector elements operate at room temperature. Gamma-ray or hard X-ray photons are converted into electron-hole pairs which migrate to the anode and cathode of an element. The read out signals are being amplified and transferred to the circuitry behind the detector plane.

The detector has an energy range of about 15–150 keV. This range describes the energy interval over which the effective area is more than 50% of the peak value. The lower end of the range is set by the internal electronic threshold while the upper one by the increasing transparency of the lead mask with increasing energy. Although the detector is able to register energies $> 200 \text{ keV}$, the charge collection in the detector elements becomes less reliable with higher energies.

The Burst Alert Telescope is an instrument that counts individual photons that interact with the detector elements. Because of limited data storage and downlink capacity, *Swift* only sends binned data products or full-event data for special triggers, i.e. gamma-ray bursts. BAT is constantly searching for hard X-ray transients and GRBs while in survey

mode, accumulating energy spectra for every detector in the array on a time scale of about 5 minutes. Sources, that are found in the 5-minute count-rate maps, are compared against an internal object catalogue. If a source is not listed in the catalogue or shows large variability, it is deemed to be transient. Data sets corresponding to the X-ray transients as well as the GRBs are distributed to the astronomical community via the gamma-ray Coordinates Network⁴ (GCN).

1.3.2 X-ray Telescope (XRT)

The X-ray Telescope (XRT) is like UVOT a narrow-FOV instrument. Its purpose is to measure the spectra, fluxes, and light curves of GRBs and their afterglows. The XRT is able to pinpoint the position of GRBs with an accuracy of 5 arcsec within its 24×24 arcmin FOV and begin to study their X-ray counterparts for days up to weeks. The telescope is equipped with X-ray focussing Wolter optics and depending on the frequency in the energy range of 0.2–10 keV a PSF of about 20 arcsec. The focal plane camera contains a single CCD-22 detector consisting of 600×602 pixels, designed for the EPIC MOS instruments on the *XMM-Newton* mission. The XRT operates in multiple different readout modes to cover the range of variability from GRB afterglows and determines autonomously which one to use. The imaging mode for example provides time-integrated image measuring and does not permit spectroscopy, whereas the photon-counting mode provides spectral and limited timing information. In a time interval of 10 ks, the detector reaches a sensitivity of about $2 \times 10^{-14} \text{ erg s}^{-1} \text{ cm}^{-2}$.

⁴<http://gcn.gsfc.nasa.gov/>

2 Theory

ANY object emits thermal radiation. The wavelength of the peak of that emitted spectral distribution shortens as the temperature rises, described by Planck's law. Light emission from fluorescent chemicals or yellow sodium street lights are examples of non-thermal radiation, since the emission does not arise (primarily) from hot objects. In various regions of an AGN, emission, reprocessing, and absorption of radiation leads to a complex energy distribution over the entire detectable spectral range. The following Sect. 2.1 describes the most important non-thermal emission processes in AGN, according to our picture of the internal mechanisms that lead to the broad-band energy distributions, described in Sect. 2.2. The last Sect. 2.3 addresses the effects of relativistic jets and beaming. This chapter is based on the textbooks by Schneider (2008) and Kitchin (2007).

2.1 Emission Processes in AGN

The most important emission mechanisms as well as their role in the unified AGN model (Sect. 1.1.3) are explained as follows. The innermost region surrounding the SMBH is the hot accretion disk. Because of collision processes of the gas and dust particles at high velocity, a broad thermal spectrum is produced with a peak value in the UV regime (Schneider, 2008). The temperature distribution of the accretion disk depends the distance to the SMBH, its mass, and the accretion rate. Wavelengths $\lesssim 912 \text{ \AA}$ cannot be observed since they are being absorbed by photo ionization of neutral hydrogen in the inter stellar medium (ISM). At much higher energies, i.e. the soft X-ray regime ($\gtrsim 0.2 \text{ keV}$), the extragalactic sky becomes observable again.

The X-ray emission of AGN is thought to be originating from the corona of the accretion disk in active or flaring regions. The observed power-law distribution of X-rays is due to thermal Comptonization, i.e. the up-scattering of optical/UV photons by a hot gas of electrons (corona) via the Inverse-Compton (IC) effect (Zdziarski et al., 1994). Beneath this X-ray continuum, one can find multiple prominent spectral absorption and emission lines, the strongest ones from highly ionized iron. The falling soft X-ray spectra at the lower energy end for Seyfert 2 galaxies suggest a soft X-ray absorbing medium for large inclination angles, i.e. the dust and gas torus surrounding the accretion disk.

The lower part of the typical broad-band spectral energy distribution received from an AGN is determined by two major processes: free-free and synchrotron radiation. The basic process here underlying emission of electro-magnetic radiation is that of the acceleration of an electric charge - including changing the direction of motion as well as changing the speed. Electrons are accelerated about 2000 times more efficiently in an electrical (or magnetic) field than protons because the proton's mass is about 2000 times that of the electron while both possess the same absolute amount of electrical charge. Therefore, electrons are thought to be almost exclusively responsible for this kind of radiation. Resulting in free-free radiation, also called "Bremsstrahlung", the electric field of an ion diverts the electron's path, but not sufficiently for a recombination. This process results in a continuous energy distribution that can extend from the radio as far as to the optical regime. In the case of synchrotron

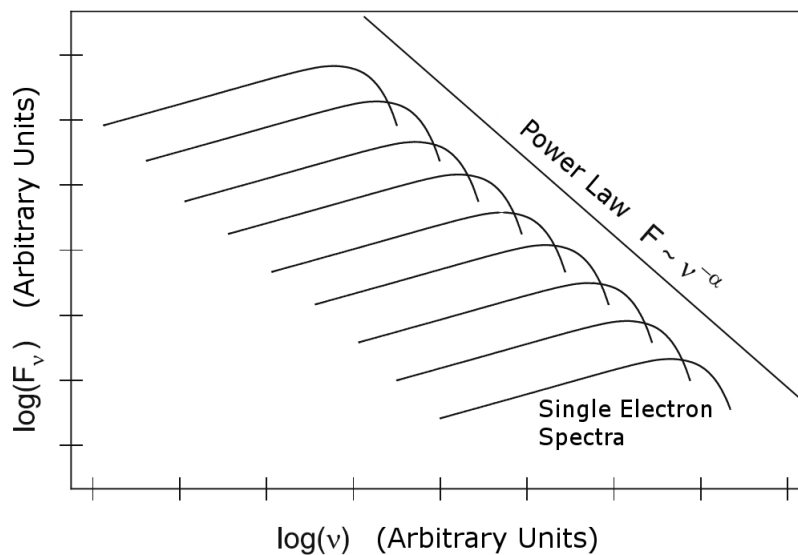


Figure 2.1: Power-law superposition of individual synchrotron spectra of electrons, (adapted from Schneider, 2008).

radiation, the accelerating force is due to a magnetic field. The charged particle's path forms a spiral around the magnetic field line and is described following the Lorentz force:

$$\vec{F}_L = \gamma \frac{q}{c} \vec{v} \times \vec{B} \quad (2.1)$$

with the charge of the particle q , speed of light c , velocity \vec{v} , magnetic field \vec{B} and the Lorentz factor:

$$\gamma = \frac{1}{\sqrt{1 - (\frac{v}{c})^2}} \quad (2.2)$$

While the velocity distribution of electrons can be described by a power-law with index p :

$$n(\gamma) d\gamma = n_0 \gamma^{-p} d\gamma \quad (2.3)$$

the overall spectrum (emitted power) of emitting electrons can be denoted as:

$$P_\nu \sim \nu^{-\frac{p-1}{2}} \quad (2.4)$$

with the spectral index $\alpha = \frac{p-1}{2}$ (Rybicki & Lightman, 1979). The emitted spectrum of the electron power-law distribution is also a power-law, as illustrated in Fig. 2.1. Although the graph does not climb limitless as it gets to lower energies. At lower frequencies, an effect called synchrotron self-absorption takes over. The electrons, responsible for the synchrotron radiation absorb the very same photons that have been emitted. It can be shown that the spectrum behaves like $P_\nu \sim \nu^{5/2}$ for lower frequencies and hereby independent of the spectral index (Rybicki & Lightman, 1979).

Synchrotron emission forms a very prominent broad bump in the AGN spectrum (Sect. 2.2) and is due to magnetic field lines that exist within the jet structure. It has been observed,

that the radio emission from AGN jets is highly polarized, revealing the direction of the magnetic field lines. Fundamental works for modelling jet creation and appearance were done by for example Blandford & Königl (1979) and Blandford & Payne (1982).

To achieve synchrotron-induced radio emission in the range of cm (≈ 10 GHz), magnetic fields of 10^{-4} G at $\gamma \approx 10^5$ are needed. This means, the radiating electrons have to be highly relativistic, and the accelerating processes very efficient. The jet kinematic is also determined by shock waves due to differences in velocity and pressure within the jet (e.g. Lister et al., 2009b).

Although jets are very prominent in radio images, many of them also clearly feature optical and X-ray emission. This implies a connection between the creation of the various emission types. The generation of optical photons can also be explained via the synchrotron mechanism (Schmidt & Smith, 2000). The same relativistic electrons in this process are able to emit X-rays via Inverse-Compton scattering of low energy photons, called synchrotron self Compton scattering (SSC) (Ghisellini & Maraschi, 1989). An initial photon with frequency ν can obtain the frequency $\nu' = \gamma^2\nu$ when scattering with an electron of the energy $\gamma m_e c^2$. With characteristic Lorentz factors of $\gamma \approx 10^4$, the electrons are easily able to up-scatter radio to X-ray photons. Another possible and likely source for photons to scatter with the relativistic electrons is the cosmic microwave background (CMB).

Both quasars and QSOs show within their spectra peaks in the infra-red and optical, called "IR-bump" and "Big Blue Bump", respectively. While the IR-bump is associated with thermal emission from dust, the Big Blue Bump is usually attributed to thermal gas in the accretion disk. About 50% of all radio-loud and radio-quiet AGN feature a soft X-ray excess component, which might be associated with the high energy tail of the Big Blue Bump (Wilkes, 2004).

2.2 The Spectral Energy Distribution of AGN

As mentioned before, AGN own a very broad energy distribution that is produced by different radiation mechanisms which for the most part are non-thermal. If the broad-band SED that is graphed as flux density F_ν against frequency ν is approximately of decreasing shape towards higher energies, then it can roughly be described by a power-law

$$F_\nu \sim \nu^{-\alpha} \quad (2.5)$$

with the spectral index α . An alternative way for graphing the energy distribution is to plot νF_ν against ν , i.e.

$$\nu F_\nu \sim \nu^{1-\alpha}. \quad (2.6)$$

For $\alpha \approx 1$ the spectrum can be described as flat, which also means an equal amount of emitted energy per frequency decade. This is shown for the example of the brightest and historically first detected quasar 3C273 in Fig. 2.2. The upper panel shows the observed energy distribution in flux over 15 orders, while in comparison the distribution in the lower panel over about four orders can approximately be described as flat. Clearly visible are synchrotron and IC peak as well as the Big Blue Bump. Low frequency radiation in the radio regime is produced in the large-scale jet structure, whereas the flatter distribution towards higher radio frequencies originates in the more compact part of the jet.

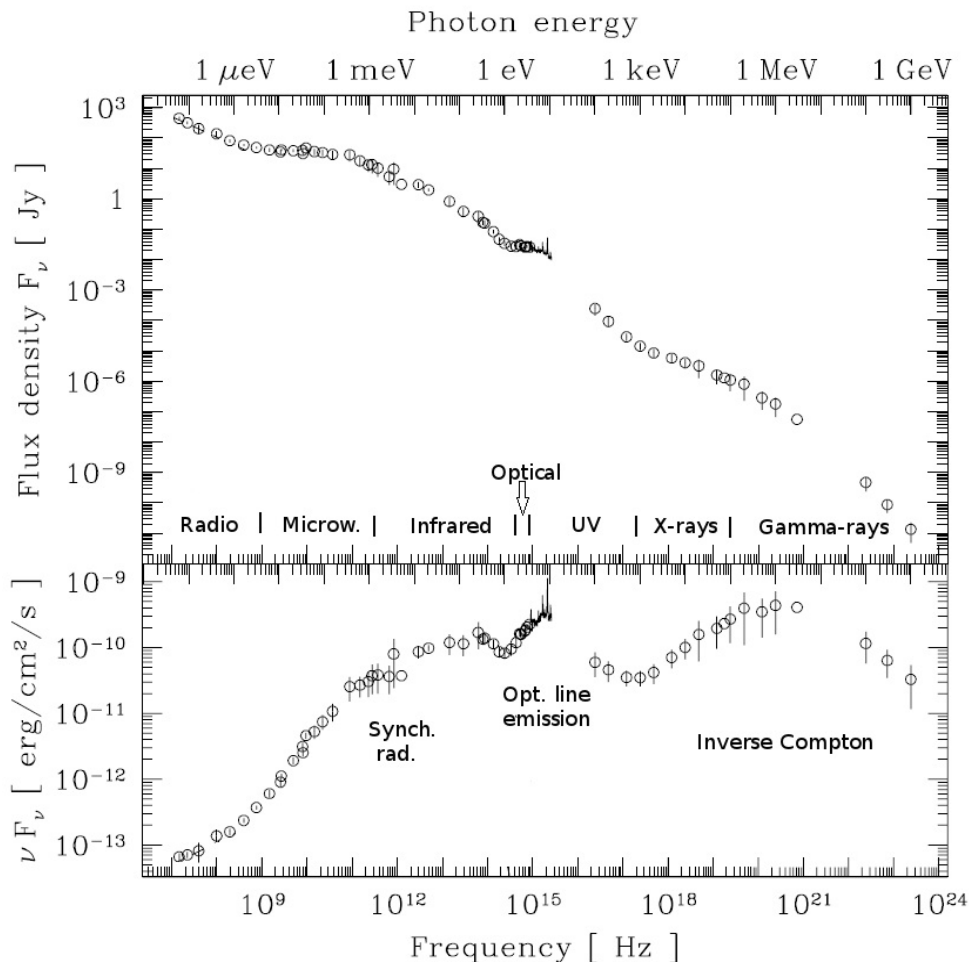


Figure 2.2: Broad-band spectral energy distribution of quasar 3C273 (adapted from Türler et al., 1999). The upper panel shows the distribution of flux F_ν with frequency ν , the lower panel νF_ν , i.e. the transmitted energy at the corresponding frequency.

Figure 2.3 illustrates the SED of another typical blazar, PKS 1510-089. The data points are composed of NED data sets and observations of *AGILE*/GRID and GASP program of the Whole Earth Blazar Telescope (WEBT). The plot shows the contributing emission processes, that are assumed for the modelling of the energy distribution. It is important to mention, that the following emission models as well as their specific parameters in the work of Pucella et al. (2008) for this particular object are just one possibility out of many other model approaches, and only serve as a demonstrative example. The prominent synchrotron and IC peaks give the SED its AGN-typical double-humped shape. The IC emission peak is composed of two different components, i.e. optical/UV photons from the accretion disk that are up-scattered in the corona and the IC reprocessing with the BLR medium. The latter one results in noticeably higher energies for the IC distribution and broadens the entire peak that expands up to very high gamma-rays. Less energetic is the broad distribution of the SSC process from the radio jet. The thermal optical/UV emission from the accretion disk form a relatively narrow peak and falls rapidly in the UV regime.

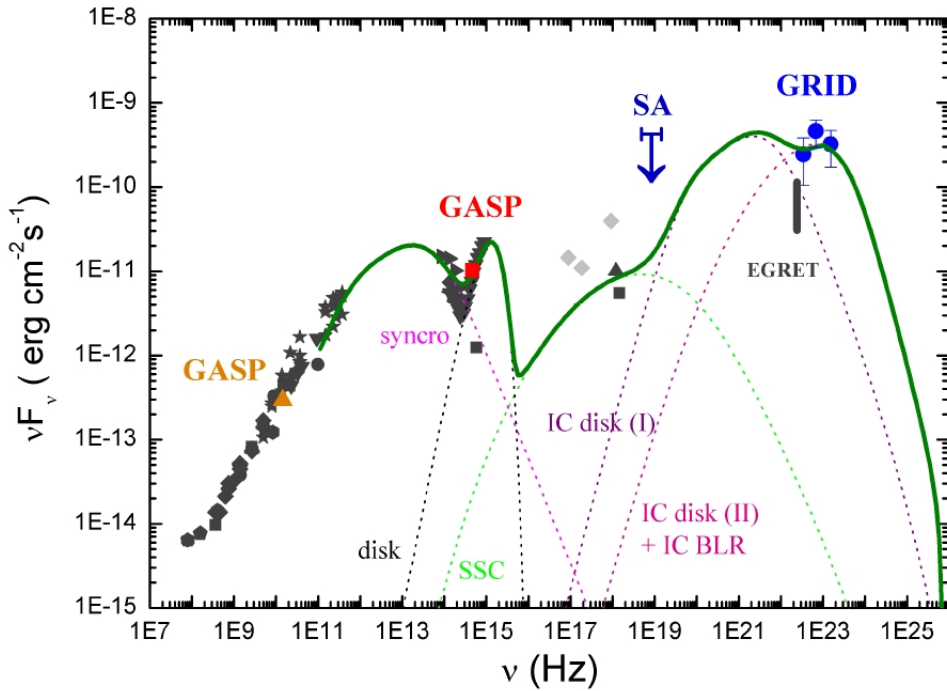


Figure 2.3: SED of blazar PKS 1510-089. Observational data are from August/September 2007 (orange, red, and blue symbols). Grey symbols show non-simultaneous historical data from NED. Image credit: Pucella et al. (2008).

The SEDs of the group of blazars exhibit large variability compared to other AGN types. Fossati et al. (1998) discovered a systematic trend in blazar samples: with increasing luminosity both the synchrotron and IC peak shift to lower frequencies, with the latter one getting more dominant. At the same time, the distance of both peaks in the frequency space stays constant. Later, this behaviour of this type of AGN has been named "blazar sequence". Figure 2.4 shows the original sample, studied by Fossati et al. (1998), i.e. the averaged SEDs in each of five luminosity bins. Depending on the position of the spectral shape, the objects have been classified into high-luminosity sources at low frequencies (LBLs) and low-luminosity sources at high frequencies (HBLs).

The blazar sequence can be interpreted in the framework of relativistic jet modelling, if the physical parameters (magnetic field, critical energy of the electrons) depend on luminosity or whether or not photons outside the jet become more important as IC seed photons in sources of larger luminosity (Fossati et al., 1998). The used blazar sample, however, was derived from radio- and X-ray detected sources and binned only to radio luminosity, possibly leading to biases. Maraschi et al. (2008) studied a X-ray selected sample of radio-loud quasars and found, that the sequence still holds in terms of a parameter sequence, relating spectral shape to emitted luminosity. Based on the 3-month blazar list from *Fermi*, the equivalent sequence could be determined involving the gamma-ray domain by Ghisellini et al. (2009). In addition to the result that more luminous gamma-ray sources have softer *Fermi*/LAT spectra, they found a dividing luminosity between BL Lacs and FSRQs that has been interpreted in terms of a critical accretion rate.

The property of variability for blazars becomes an issue when measuring spectral domains,

whose slopes then greatly depend on the individual object and temporal state of the emission. In this work the hard X-ray measurements in the energy range of 20–100 keV are very close to the spectral position where synchrotron and IC emission peak meet. This has to be considered for the results of spectral slopes and further discussion towards the blazar sequence and other properties of the sample.

In the end, the blazar sequence is still an object of hot debate, issuing the validity for all blazars. For example, recent works by Padovani (2007) or Giommi et al. (2012) question the sequence on the basis of possible selection effects and shallow radio- and X-ray surveys, respectively.

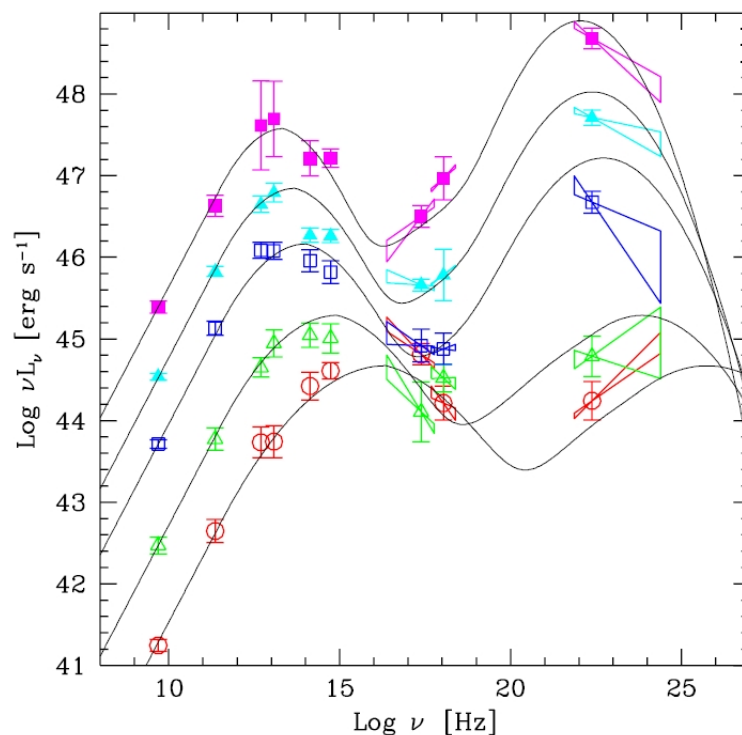


Figure 2.4: Average SEDs of the original blazar sample studied by Fossati et al. (1998), grouped into five luminosity classes. Image credit: Donato et al. (2001).

2.3 Radio Jets and Relativistic Beaming

The following part is based on Kadler (2012) and Cohen et al. (2007) and gives an overview of the relativistic mechanisms that are an issue when observing and understanding extragalactic jets. When detecting the emitted radiation, one has to take into account that the radiating particles inside the jet move with relativistic velocities. The measured radiation from the jet is called a beam, which is characterized by three parameters: intrinsic luminosity L_0 , Lorentz factor γ , and inclination angle θ . Many blazar jets exhibit a striking property, the apparent superluminal motion of compact jet features, also called "blobs". Due to a projection effect of the emitted radiation by blobs that are moving with high velocities, resulting apparent transverse velocities $v_{\text{app}} > c$ (or $\beta_{\text{app}} = v_{\text{app}}/c > 1$) are observable. Values of v_{app}

for the MOJAVE sample are mostly distributed up to ≈ 20 c with a peak value at ≈ 50 c. For relativistic jets, the Doppler factor D , the apparent transverse velocity in units of the speed of light β_{app} , and the luminosity can be calculated (e.g. Kadler, 2012, and references therein):

$$D = \frac{1}{\gamma(1 - \frac{v}{c} \cos \theta)} \quad (2.7)$$

$$\beta_{\text{app}} = \frac{\beta \sin \theta}{1 - \beta \cos \theta} \quad (2.8)$$

$$L = L_0 D^{p-\alpha} \quad (2.9)$$

with spectral index α and the parameter p , which depends on the geometry of the jet. For a smooth jet, $p = 2$ while for a single blob $p = 3$ is used (Lind & Blandford, 1985). Assuming a constant flux, i.e. $\alpha \approx 0$, one obtains the relation $F \propto D^2$. This also means that flux limited samples are highly biased towards sources with small inclination angles, since the measured fluxes are largely boosted.

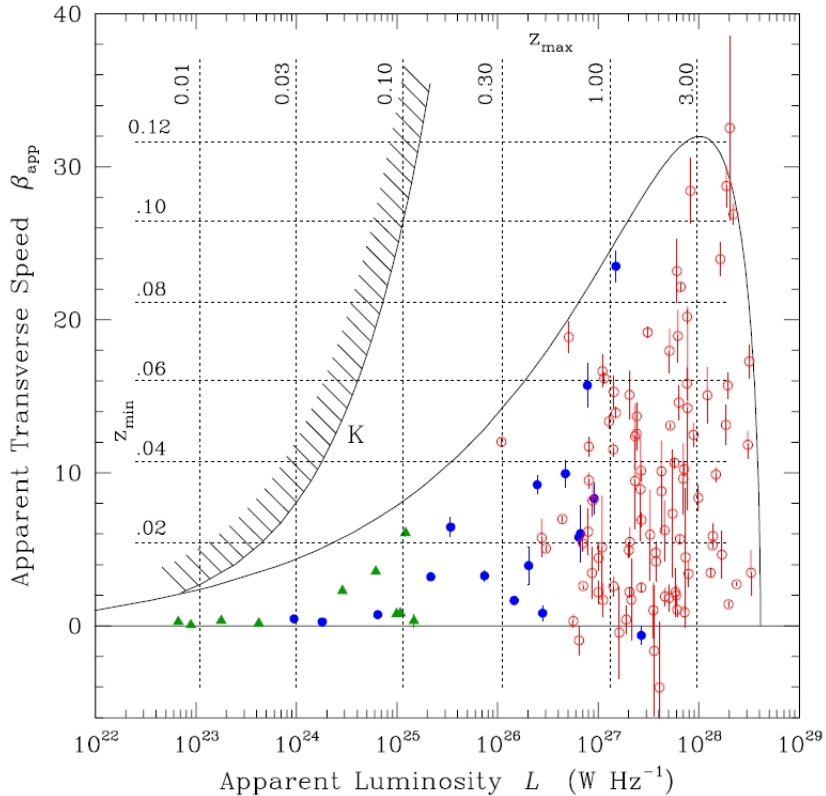


Figure 2.5: Apparent jet velocity vs. apparent radio luminosity. The solid curve is defined by the parameters $\gamma = 32$ and $L = 10^{25} \text{ W Hz}^{-1}$. Only sources right of the curve K are detectable by MOJAVE. Red open circles indicate quasars, blue filled circles BL Lacs, and green filled triangles radio galaxies. Image credit: Cohen et al. (2007)

For 119 of all 135 sources in the MOJAVE-1 catalogue, apparent jet velocities β_{app} and luminosities L at $\lambda = 2\text{ cm}$ were determined by Cohen et al. (2007). Both quantities are plotted against each other in Fig. 2.5. The distribution concentrates towards higher radio luminosities with also larger jet velocities. The solid line indicates a modelled aspect curve with the parameters $\gamma = 32$ and $L = 10^{25}\text{ W Hz}^{-1}$ for a variable inclination angle. The curve envelopes all data points within their uncertainties and defines upper limit values for γ and L . Only sources on the right-hand side of the curve K are detectable by MOJAVE, although no sources have been detected between K and the solid curve. Furthermore, the vertical and horizontal lines in Fig. 2.5 represent a redshift interval, in which a source would be observable. This implies that the absence of luminous sources with low jet speeds is a genuine property of AGN jets and not due to selection effects.

3 The AGN Sample(s)

DURING the past decades, numerous AGN surveys and extragalactic surveys in general have been conducted in the range from the radio regime up to very-high energy gamma-rays, contributing to the overall picture of the broadband emission behaviour of AGN. It is important to notice that surveys of active galaxies strongly underlie selection effects, which are specific for the energy regime, the detector and the variability of the observed source (e.g. Krolik, 1999). The latter one becomes more important when dealing with single measurements or measurements less frequent than the time scale of variability of the object. Surveys that integrate detector counts over long time scales such as months or years provide an averaged picture of the emission properties of the sky in the corresponding frequency range. Long exposure times are especially necessary in the X-ray and gamma-ray regime, where signals from very distant sources are relatively faint. In the following, the used survey catalogues for hard X-rays and gamma-rays as well as the catalogue for the radio observations of the used AGN sample are described.

3.1 The MOJAVE-1 Sample

The radio flux-density limited MOJAVE-1 sample⁵, counting 135 sources, is part of nearly 300 compact AGN in the northern hemisphere, that are continuously monitored by interferometric measurements (see Sect. 1.2). The original MOJAVE-1 sample had the following selection criteria: declination $\geq -20^\circ$, Galactic latitude $|b| \geq 2.5^\circ$, a total 2 cm (15 GHz) flux density greater than 1.5 Jy at any epoch between 1994.0 and 2004.0 and more than 2 Jy for sources below the celestial equator. On the basis of compact radio emission at 15 GHz, the sample is statistically complete. This is crucial when studying blazar samples that are normally subject to selection biases. About 94 % of the sample shows one-sided jet morphologies, which are most likely due to relativistic beaming. Five objects show two-sided parsec-scale jets and three sources are virtually unresolved (Lister et al., 2009a). The apparent speeds of some of the jet components range up to $\approx 50c$, which is explained by a projection effect of relativistically moving matter that emits radiation (see Sect. 1.1.3). Nine sources of the sample lack a redshift, mainly because of featureless spectra that do not allow a redshift determination via measuring the shift of spectral lines.

Following the optical classification scheme of Véron-Cetty & Véron (2003), the 135 AGN of this sample can be divided into 101 quasars, 8 radio galaxies, 22 BL Lacs and 4 unidentified objects (no known optical counterpart). The sample is very much dominated by blazars with overall flat radio spectra, defined as a spectral index α flatter than -0.5 at any frequency between 0.6 and 22 GHz (Lister et al., 2009a).

The later addition of sources to the monitoring program involved new objects with various special properties such as the detection with the gamma-ray instrument EGRET in the VLBA area of sight, AGN with unusual jet kinematics, or newly detected AGN above declination $\geq -30^\circ$ until 2010.0.

⁵<http://www.physics.purdue.edu/astro/MOJAVE/>

3.2 The BAT Catalogues and Other X-ray Surveys

3.2.1 Previous and Concurrent Missions

The following brief historical overview is based on Brandt & Hasinger (2005). First all-sky surveys in the soft X-ray regime (about 0.5 – 10 keV) done by *Uhuru* and *Ariel V* showed that the previously discovered cosmic X-ray background (CXRb) was rather isotropic and constant in time. Observations with improved resolution provided by focussing optics (Wolter telescopes) quickly showed that the CXRB was composed of distinct sources. This was confirmed in the case of already known AGN, that showed to be luminous X-ray emitters (Tananbaum et al., 1979). Observations with *ROSAT* (Truemper, 1982) identified about 75% of the CXRB as distinct sources (Hasinger et al., 1993) with the vast majority of these objects being AGN. Harder X-ray surveys above 2 – 3 keV were conducted by *ASCA* (Tanaka et al., 1994) and *BeppoSAX* (Boella et al., 1997) with considerably less of the CXRB being resolved for higher energies. Two current missions which are performing soft X-ray surveys are *Chandra* (Weisskopf et al., 2000) and *XMM-Newton* (Jansen et al., 2001), both equipped with highly resolving Wolter telescopes and with 50 – 250 times the sensitivity of previous missions.

Hard X-ray detectors with a range up to a few hundred keV are used aboard of *Swift* (Gehrels et al., 2004), *INTEGRAL* (Winkler et al., 2003), and *Suzaku* (Mitsuda et al., 2007). The latter two are performing pointed observations while the Burst Alert Telescope (BAT, Barthelmy et al., 2005) of *Swift* is able to observe the sky at very large angles and hence providing the most uniform coverage of the sky in hard X-rays up to date.

One of the most recent approaches towards a Hard X-ray survey of extragalactic sources and AGN is the *Swift-INTTEGRAL-X-ray* (SIX) survey (Bottacini et al., 2012), combining both *Swift*/BAT and IBIS observations from *INTEGRAL* for increased exposure time. The catalogue includes 113 objects, 86 of them AGN, measured in the energy band of 18–55 keV. Due to *INTEGRAL*'s pointed observation strategy of mostly Galactic sources, and *Swift*'s quasi randomly pointed all-sky observations, the commonly observed area is up to this point about 15% of the entire sky. Bird et al. (2010) reason, that the non-detection of sources by *INTEGRAL* that have been detected by BAT is caused by a too low exposure time in the IBIS/ISGRI instrument.

3.2.2 BAT: 58 and 70 month catalogues

The *Swift*/BAT 58-month catalogue (Baumgartner et al., 2010) consists of 1092 objects in the energy band of 14–195 keV with the majority being AGN. The number of 519 sources have been classified as Seyfert 1 galaxies and 108 as Beamed AGN, including blazars. The number of objects in the catalogue is significantly smaller than the multitude of detected signals that differ from zero flux. To ensure that the final catalogue consists of certain detections, only sources with background-subtracted signal-to-noise ratios (SNR) above 4.8 were allowed. This threshold value was computed so that $\simeq 1$ source of the sample can be expected to be false (Tueller et al., 2008). The identification of the sources with counterparts in other wavelength bands was done with the help of high angular resolution X-ray data from *Swift*/XRT or archival data.

Figure 3.1 shows an Aitoff projection in Galactic coordinates of the BAT sources, divided into various types. The majority of Galactic sources are being accounted for by X-ray Bina-

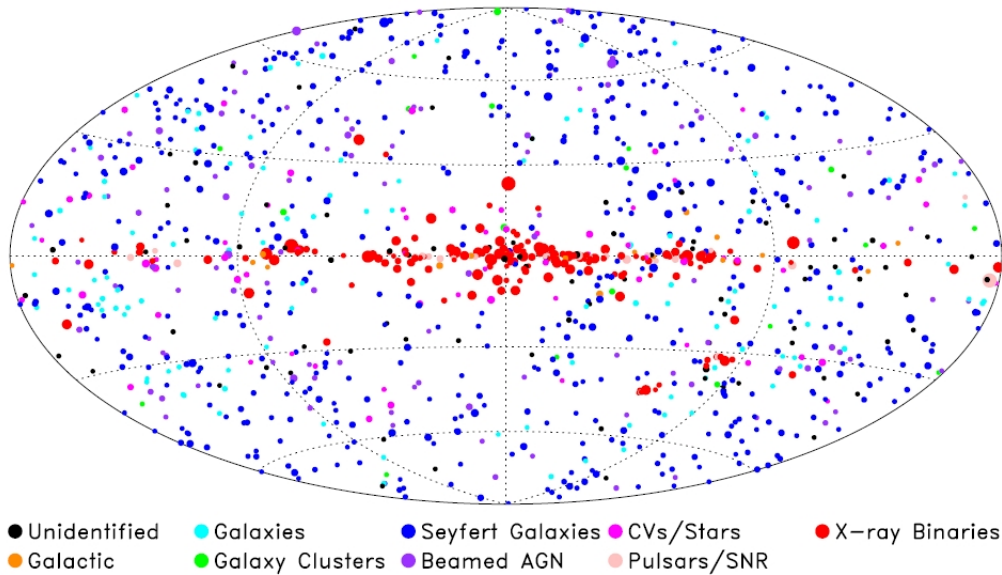


Figure 3.1: Hard X-ray sources of the 70-month BAT catalogue. The symbol size is proportional to the X-ray flux (Baumgartner et al., 2012).

ries, mainly distributed in the Galactic plane. AGN types are distributed rather uniformly, with a minor reduction of detections in the Galactic plane, since exposure times are higher for Galactic latitudes $|b| \geq 15^\circ$ (Tueller et al., 2010). The symbol size of the detections is proportional to the registered X-ray flux.

For this work the recent 70-month BAT survey (Baumgartner et al., 2012) has been used, which features the highest integration time for faint hard X-ray sources compared to previous surveys⁶. This new updated catalogue includes 1171 detected hard X-ray sources down to the threshold of 4.8σ . The majority of new sources in the catalogue continue to be AGN, with over 700 total. Since the analysis encompasses the X-ray properties of radio-selected AGN (MOJAVE-1 sample, see Sect. 3.1), the X-ray spectra of all sources from the sample have been extracted from measurements at the exact radio positions (Tueller, J., priv. communication). The appearance of common AGN in the MOJAVE-1 sample and the 58-month BAT catalogue is discussed in Sect. 5.1.

3.3 The Fermi/LAT Catalogues

In 2008 the *Fermi Gamma Ray Observatory* was launched to detect gamma-ray bursts and monitor the sky at high energies up to the range of GeV. The instrument for the latter operation is the Large Area Telescope (LAT, Atwood et al., 2009), whose main objectives encompass the identification of unidentified EGRET (Kanbach et al., 1988) sources, the analysis of the diffuse emission of both extragalactic and Galactic origin (Atwood et al., 2009). Since its mission start the following object catalogues have been compiled:

- Based on the first three months of LAT measurements, the sources with a significance $\gtrsim 10\sigma$ have been published as the 0FGL catalogue, containing 205 objects in the energy range of 0.1–100 GeV (Abdo et al., 2009).

⁶<http://heasarc.gsfc.nasa.gov/docs/swift/results/>

- Including data from the first 11 months of operation, the *Fermi*/LAT First Source Catalogue, or 1FGL was compiled (Abdo et al., 2010b). The number of 1451 sources have been detected at a significance $\gtrsim 4\sigma$, from which 630 have no clear counterpart at other frequencies. 1043 objects are at high Galactic latitudes ($|b| \geq 10^\circ$). Averaged properties of all objects such as photon index, flux and luminosity are presented as averaged values as well as the intensity with monthly binning.
- Similar in its properties, the *Fermi*/LAT Second Source Catalogue (Nolan et al., 2012), or 2FGL, extended the exposure time to 24 months and comprises 1873 at the same significance threshold of the 1FGL catalogue. Because of the higher integration time, in many cases more complex models than previously used simple power-law fits had to be applied. For the correlation studies in this work the 1FGL catalogue has been used instead, since the time scale of the 2FGL survey surpasses the end of the BAT survey.
- Abdo et al. (2010a) presented the first catalogue of 709 AGN detected by LAT (1LAC), based on the high-latitude 1FGL sources. This includes 300 BL Lacs and 296 flat spectrum radio quasars (FSRQ). Compared to detections from *INTEGRAL*/IBIS and *Swift*/BAT (based on the forth IBIS catalogue (Bird et al., 2010) and the BAT 54-month Palermo catalogue Cusumano et al. (2009)), 50 high-latitude 1LAC sources can be associated with hard X-ray detections of AGN.

4 Spectral Processing and Statistical Analysis

THIS chapter addresses the fitting and processing of the BAT spectra as well as the determination of the photon indices, fluxes and luminosities of the sources in the MOJAVE-1 sample. Furthermore, the used methods for the statistical and correlational analysis are described. If not stated otherwise, the statistics part is based on the textbook "Mathematical Statistics" by Pestman (2009). For the processing of the BAT spectra and the statistical analysis, the *Interactive Spectral Interpretation System* ISIS (Houck & Denicola, 2000) version 1.6.2-3 has been used.

The 135 X-ray count rate spectra as measured by *Swift*/BAT, as well as the response file were provided by J. Tueller and the *Swift* team⁷. The spectra span the energy range of 14–195 keV and are divided into eight energy bins of different sizes.

4.1 Spectral Fitting and X-ray Flux

4.1.1 Quality of the X-ray Spectra

By applying a simple power-law fit over the entire available spectral range, photon indices and X-ray fluxes can be determined for the brightest sources, which are each listed in the 70 month BAT catalogue (Baumgartner et al., 2012). Although BAT observed at 14–195 keV, for the following evaluation and analysis only the data from 20 to 100 keV were used, neglecting the first (14–20 keV) and the last two bins (100–150 keV, 150–195 keV). This reduction is necessary since the measured data in the lowest bin have significantly lower count rates compared to the next bin, especially in the spectra featured by low BAT SNR sources. The highest bins were ignored due to very low count rates at high energies, that are dominated by the background.

Despite of the truncated spectra, for a majority of the sources no simple power-law fit is feasible. Figure 4.1 shows the lower SNR range of the sample, i.e. the result of the fit parameter Γ , the photon index. Because the photon indices of sources below a significance of about 3σ have uncertainties as large as the full range $0 < \Gamma < 5$, estimated to be sensible, the flux and luminosity calculation has to be approached in a different way for this part of the sample. In order to obtain viable values for the X-ray flux, one has to make a certain assumption to minimize the uncertainties, in this case the fixing of the photon index. From this point forward, all sources with BAT SNR $> 3\sigma$ are designated *bright* and all sources below that limit *faint*.

4.1.2 Bright Sources

The X-ray spectra of the bright sources feature uncertainties that are small enough to allow feasible spectral fitting. The used XSPEC V12 (Arnaud, 1996) model *pegpwlw*, implemented

⁷NASA/Goddard Space Flight Center, Astrophysics Science Division, Greenbelt, MD 20771

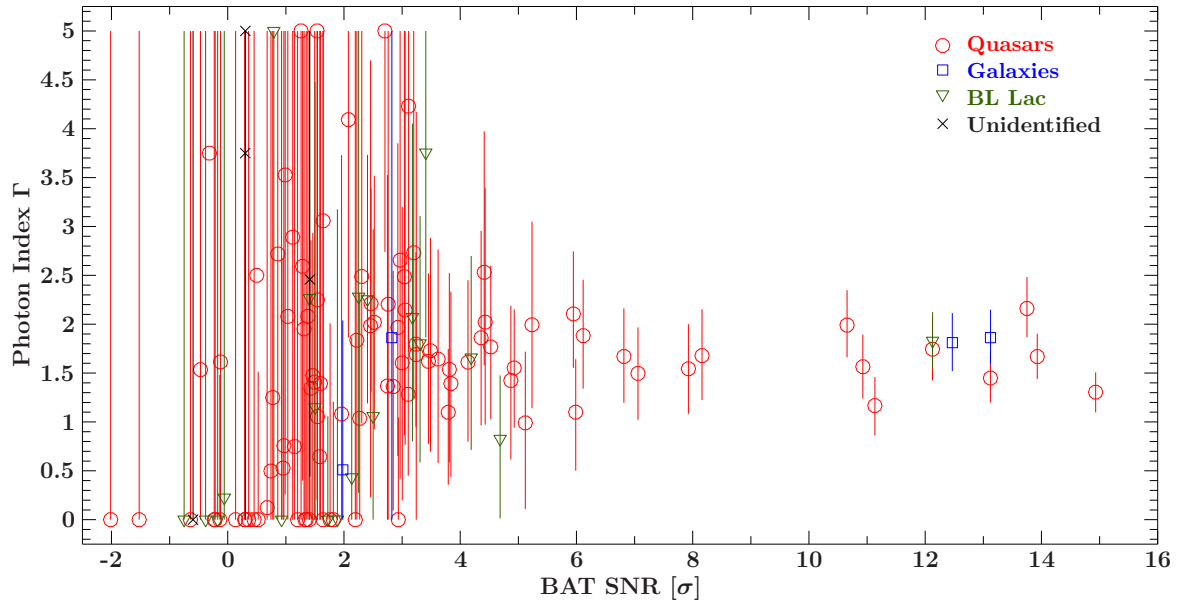


Figure 4.1: Relation of photon index Γ (result of spectral power-law fit) and BAT SNR. For better readability, seven sources at high SNRs have been omitted, with the highest value 177σ .

in ISIS, is a simple power-law with normalization K and photon index Γ for parameters:

$$f(E) = KE^{-\alpha} \quad (4.1)$$

with the spectral index $\alpha = \Gamma - 1$. The used model allows to determine directly the flux in $10^{-12} \text{ erg s}^{-1} \text{ cm}^{-2}$, which equals the normalization K . The fitting process starts by comparing the data of the spectrum to the model. How well the data fits to model, i.e. the goodness-of-fit is expressed by the resulting χ^2 statistics. For an optimal fit of the data, the parameters of the model are systematically varied to obtain the best-fit parameters. A χ^2 test reveals the quality of the fit and is described by:

$$\chi^2 = \sum_{k=1}^n \frac{(E_k - T_k)^2}{T_k} \quad (4.2)$$

with E_k for the empirical and T_k for the expected frequentness of the class k , i.e. count rates in the different energy bins. As a measurement for a good model fit, the reduced χ^2 is used, which takes into account the number of free parameters ν_p and the number of energy bins ν_b :

$$\chi_{\text{red}}^2 = \frac{\chi^2}{\nu} \quad (4.3)$$

with the number $\nu = \nu_b - \nu_p$, called degrees of freedom. The closer χ_{red}^2 is towards 1, the better the model fit. Values between 0 and 1 can be described as "over fitted". In these cases, large uncertainties in the spectrum result in a great range of possible fits.

An example for of the BAT spectra of rather bright sources is shown in Fig. 4.2 (left panel), the BL Lac object 2200+420 (BL Lacertae itself) at $\text{SNR} = 12.1\sigma$. The fit results in a photon

index $\Gamma = 1.83_{-0.28}^{+0.29}$ with $\chi_{\text{red}}^2 = 0.61$, where all data points are covered. Fainter sources, meaning detections with lower SNR, have lower count rates and larger relative uncertainties (see Sect. 4.1.3). On the other hand, very bright sources tend to have very small relative uncertainties, which may lead to poorer fit statistics. For example the brightest object in the sample, 1226+023 (3C273) at $\text{SNR} = 177\sigma$ and with $\chi_{\text{red}}^2 = 2.07$. When modelling a spectral fit for a single bright source like 1226+023 or 0316+413 (3C84) with poor fit statistics, a more complex fitting model is appropriate. For the purpose of determining values for flux and luminosity, especially for fainter sources, the fit method used here is estimated to be of sufficient use.

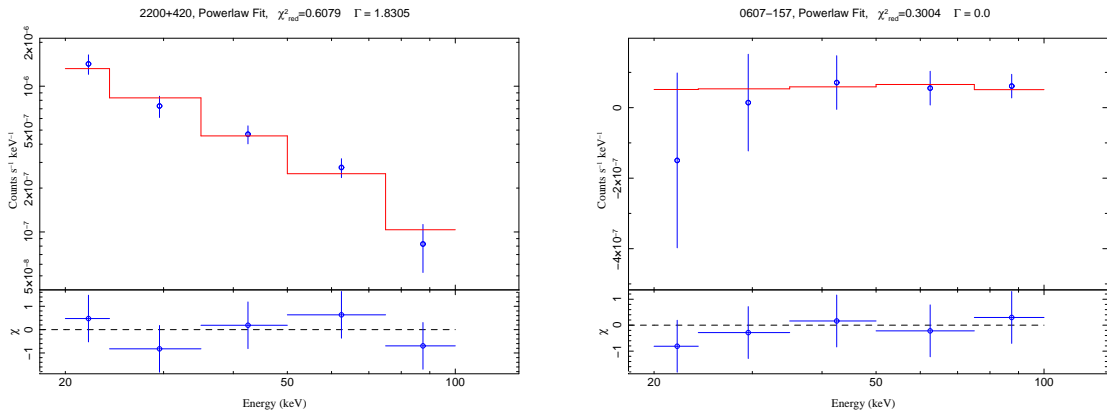


Figure 4.2: BAT spectrum of 2200+420 (left panel) and 0607-157 (right panel) in the energy range of 20-100 keV with power-law fits. The lower panels show the residuals of the fits.

4.1.3 Faint Sources

Determining the X-ray fluxes and luminosities of fainter sources has to be approached in another way. An example for a spectrum of a faint source is shown in Fig. 4.2 (right panel), here the quasar 0607-157 at $\text{SNR} = 0.52\sigma$. A simple power-law fit results in $\Gamma = 0.0_{-0.0}^{+5.0}$ because of the weak spectrum and the relatively large uncertainties of the data points. As mentioned before, the restriction of a frozen photon index in being made. It is assumed that the faint objects have a similar spectral shape than the brighter sources. The photon index Γ for all faint sources is assumed to be the averaged value of all bright sources with the same optical classification after Véron-Cetty & Véron (2003), that is quasars, radio galaxies, BL Lacertae objects (BL Lacs) and unidentified sources (no known optical counterpart). These averaged photon indices Γ_{av} with the uncertainty of one standard deviation as well as the number of all object types are shown in Table 4.1. In general, the fluxes are proportional to the count rates integrated over the energy bins. A simulated spectrum in the same energy range with frozen photon index Γ_{av} is used to calculate the flux of the real spectrum:

$$F_{\text{spec}} = F_{\text{sim}} \frac{R_{\text{spec}}}{R_{\text{sim}}} \quad (4.4)$$

with the F for the X-ray fluxes and R for the count rates. For comparative reasons, it

AGN Class	Bright Sources	Faint Sources	$\Gamma_{\text{av,bright}}$
Quasar	41	60	1.76 ± 0.54
BL Lac	6	16	1.99 ± 0.96
Galaxy	6	2	2.18 ± 0.66

Table 4.1: Number of optical classifications of MOJAVE-1 sources (Véron-Cetty & Véron, 2003). All sources with a BAT SNR > 3.0 are called bright, else faint. Average values for Γ refer to the subsample of bright sources.

is furthermore assumed that the small group of unidentified sources has the same spectral shape, i.e. averaged photon index as quasars.

The estimated uncertainties of the flux values are derived from the uncertainties of Γ_{av} and the count rates of every energy bin by Gaussian error propagation. All faint sources with flux uncertainties that are compatible with negative flux values are classified as upper limits. For the calculation of the upper limit flux, the integrated count rate of the faintest valid source (2121+053) was used.

Figure 4.3 shows the relation of the flux to the SNR value of sources. Thirteen upper limits at negative SNRs have been omitted due to logarithmic scaling. The dashed line indicates SNR = 3σ , which splits bright and faint sources. As for the bright sources, the X-ray flux increases with the signal and forms a power-law in linear scaling. The relative uncertainties grow significantly with decreasing SNR, a trend that approximately applies for the faint sources, too. Upper limits range up to about 1.6σ .

4.2 X-ray Luminosity

The luminosity L , being the total energy of a source emitted per time, is calculated by the flux multiplied by the area on which it equally distributes at a luminosity distance d_L given by Lister et al. (2009b). Since the spectra of very distant objects have a cosmological redshift, the luminosity is altered. The factor involving the redshift z and the photon index Γ , the K-correction, extrapolates the spectral shape as described by Ghisellini et al. (2009):

$$L = \frac{1}{(1+z)^{2-\Gamma}} 4\pi d_L^2 F \quad . \quad (4.5)$$

The assumed cosmological constants are the following: $H_0 = 71.0 \text{ km s}^{-1} \text{ Mpc}^{-1}$, $\Omega_M = 0.27$ and $\Omega_\lambda = 0.73$ (Lister et al., 2009b). Luminosity values for the 15GHz radio measurements, as obtained by Kovalev et al. (2005), are also calculated for the X-ray correlation studies (see Sect. 5.3). It is assumed that the radio spectra of core dominated extragalactic jets are typically flat, meaning a photon index of $\Gamma \approx 2$. Hence, a K-correction is not necessary for the radio data.

4.3 Tests and Correlation Analysis

This section shows the statistical methods and tests for significance of correlations of various data sets. The methods are being applied to the properties of samples of objects

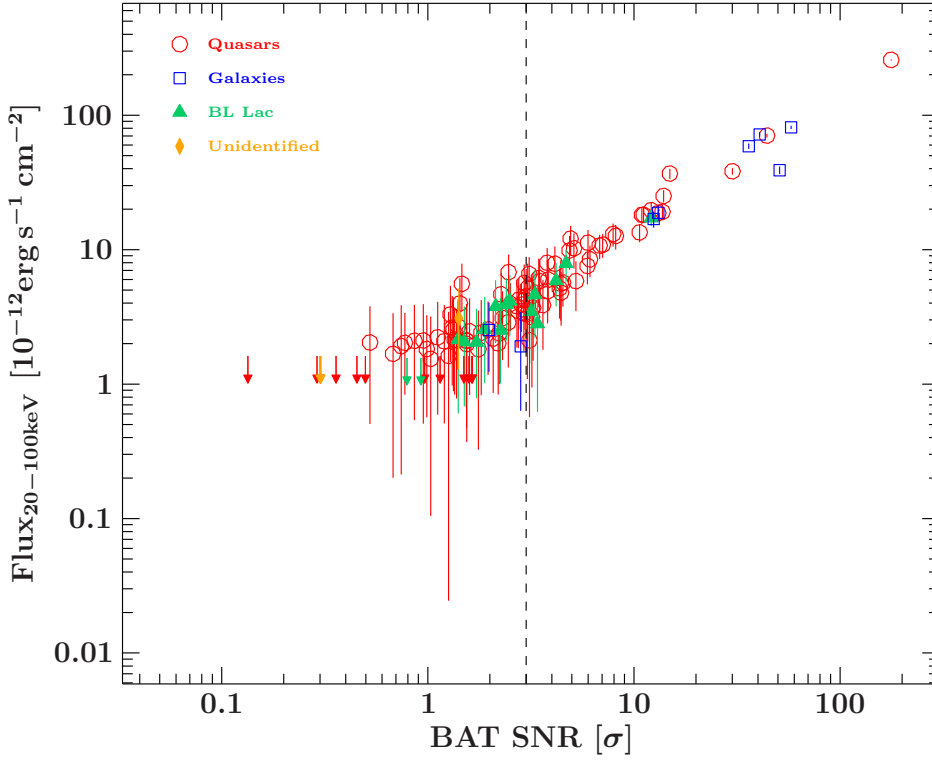


Figure 4.3: Relation of hard X-ray flux to BAT SNR. The dashed lines represents the SNR value of 3.0σ .

and allow to make statements about the correlation behaviour between for example flux and luminosity measurements.

4.3.1 Two-Sample Kolmogorov-Smirnov Test

A Two-Sample Kolmogorov-Smirnov test (KS test) is a version of the One-Sample KS test, that checks a one-dimensional set of data whether or not it follows a compared distribution function at a given confidence level. The Two Sample KS test compares two data sets that do not need to have the same length. The result of the test is the p -value for the null hypothesis that both sets share the same underlying distribution. Let X_1, X_2, \dots, X_n with n elements be sample A and Y_1, Y_2, \dots, Y_m with m elements be sample B with the distribution functions F_A and F_B , respectively. It is tested if the null hypothesis

$$H_0 : F_A(X_i) = F_B(Y_i) \quad (4.6)$$

or the alternative hypothesis

$$H_1 : F_A(X_i) \neq F_B(Y_i) \quad (4.7)$$

is correct. The test statistic if the 2-sample KS-test is the amount of the largest difference between both distributions:

$$D = \sup |F_A(x) - F_B(x)| \quad (4.8)$$

for every item x in both datasets. It follows that the hypothesis that the data originates from a common distribution function has to be rejected if the value of D is too large. Critical values for D at which one has to reject the hypothesis at a given level α are listed in common tables. The p -value is determined based on the probability that D is smaller than its critical value. A detailed derivation of the test can be found for example in Pestman (2009).

4.3.2 Correlation Coefficient and Partial Correlation

A dimensionless measure of correlation between two data sets can be described by the correlation coefficient. For the use of physical quantities that in most cases have a power-law relation to another set of quantities, the Spearman correlation coefficient, or rank correlation coefficient r_S is being calculated. The data set is composed of pairs of values that each belong to the two sets of quantities and are called ranked values. The coefficient r_S is generally expressed as

$$r_S = 1 - 6 \sum \frac{d^2}{n^3 - n} \quad (4.9)$$

where n is the number of pairs of values and with $\sum d^2 = \sum_{i=1}^n d_i^2$, with d being the ranked difference between the i th measurements of the pair of values (Zar, 1972). The coefficient is in the range of $-1 < r_S < 1$, representing a negative or positive correlation with respect to the sign. The higher the absolute value of r_S , the more correlated are the two data sets.

While the correlation coefficient is used for sets of information that were acquired independently from each other, the comparison of two different data sets have to be handled in another way, if the calculation of the data sets involves a common parameter. For example, this is the case when looking for a correlation of the luminosity of distant objects in different energy domains. Since the determination of the luminosity depends on the same redshift z , the resulting correlation is misleadingly high. Graphing the two luminosity data sets for a sample of objects against each other produces a stretched out distribution of data points (see discussion in Sect. 5.3.2). To avoid this effect, one has to conduct a test for partial correlation, eliminating the influence of a third parameter, in this case the redshift. This method, based on Kendall's rank correlation coefficient τ (Kendall, 1938) has been presented by Akritas & Siebert (1996) for the case of censored data, i.e. upper limits or partial knowledge of a data set. Partial Kendall's τ is defined as:

$$\hat{\tau}_{12,3} = \frac{\hat{\tau}_{12} - \hat{\tau}_{13}\hat{\tau}_{23}}{\sqrt{(1 - \hat{\tau}_{13}^2)(1 - \hat{\tau}_{23}^2)}} \quad (4.10)$$

with the variables $\hat{\tau}_{kl}$ as the censored data version of Kendall's τ . The indices 1 and 2 stand for the compared data sets and 3 indicate the spurious parameter. For a detailed derivation of $\hat{\tau}_{12,3}$ and the estimated variance $\hat{\sigma}^2$ see Akritas & Siebert (1996). One can reject the hypothesis for zero partial correlation at a level α , if

$$\left| \frac{\hat{\tau}_{12,3}}{\hat{\sigma}} \right| > z_{\alpha/2} \quad (4.11)$$

with $z_{\alpha/2}$ as the $100(1 - \alpha/2)$ -th percentile of the standard normal distribution. For example, if the relation 4.11 applies at a level of $\alpha = 0.05$, i.e. for $z_{\alpha/2} = 1.96$, the null hypothesis of zero partial correlation between the compared data sets has to be rejected. Meaning, both data sets are correlated under the probability of error of 5%.

A generic FORTRAN program, implementing this method, can be found under http://www2.astro.psu.edu/statcodes/cens_tau.f. For this work, the program has been implemented in SLANG for the use in ISIS for the use of ascii files that contain the corresponding data sets. It is listed in Appendix C. The method for a partial correlation analysis is also being applied to averaged SEDs of the used AGN sample to find a possible correlation of the slope in the X-ray and the gamma-ray regime that might depend on the X-ray luminosity as the third parameter (see discussion regarding the blazar sequence, Sect. 6.4).

5 Results

IN this chapter the results from the statistical and correlation studies as described in Sect. 4 are presented. It is structured as follows: in 5.1 the statistical estimation of the minimum number of hard X-ray emitters in the MOJAVE-1 sample is described. The general hard X-ray properties are presented in 5.2, as well as the results of the calculation regarding possible correlation behaviour to radio and gamma emission in 5.3. Additional plots and tables are shown in the Appendices A and B. Basic statistical results of this work are being published in Langejahn et al. (2013).

5.1 MOJAVE Sources as Hard X-ray Emitters

Comparing the sources in both the MOJAVE-1 sample and the *Swift*/BAT 58-month catalogue, 29 sources could be associated by a positional offset analysis. However, since the BAT catalogue features a signal to noise (SNR) threshold value of 4.8σ , the majority of all MOJAVE-1 objects lies below this limit.

The distribution of the background-subtracted BAT SNR confirms this assumption. Figure 5.1 shows the distribution of the MOJAVE-1 sources (cut at 15σ for better readability), in relation to the distribution of SNR values of a blank sky survey of 615 random positions. The positions have been selected to have 30 arcmin distance to any known source detected by MOJAVE, *Swift*/BAT, *Fermi* and *INTEGRAL* (Tueller, J., priv. communication). The panels show: (a) the distribution for a blank sky survey, (b) the renormalized blank sky distribution relative to (c) the MOJAVE-1 sample, and (d) the subtracted distribution of the renormalized blank sky and MOJAVE histogram (c-b). Negative SNR values result from local signals recorded on the BAT detector that are weaker than the subtracted background.

The SNR distribution of the MOJAVE sources shows a clear positive offset with a tail of highly significant sources. The solid line indicates 0σ , the line at 4.8σ the 58-month threshold value, that corresponds to ≈ 1 false source in the catalogue (Tueller et al., 2008). The re-scaling factor for the distribution in panel b) is estimated by calculating the ratio of the bin -1σ to 0σ in a) and c). Because the MOJAVE distribution has a significantly smaller amount of sources below -1σ compared to b), it is estimated the re-scaling and therefore the subtraction of both distributions to be rather conservative. Subtracted by the 37 sources of the rescaled blank sky survey, the MOJAVE-1 sample still holds 98 sources that can be considered hard X-ray emitters, although most of them are at very low signal to noise ratios.

Figure 5.2 shows the distribution of the BAT SNR values for different source types. Hatched areas represent sources for which only upper limits for the X-ray fluxes could be determined. The highest value at about 177σ belongs to the quasar 3C273 and has been omitted in the histogram. Additional to the classification into bright and faint sources (see Sect. 4.1.1), they can be divided into four groups concerning the specific SNR range:

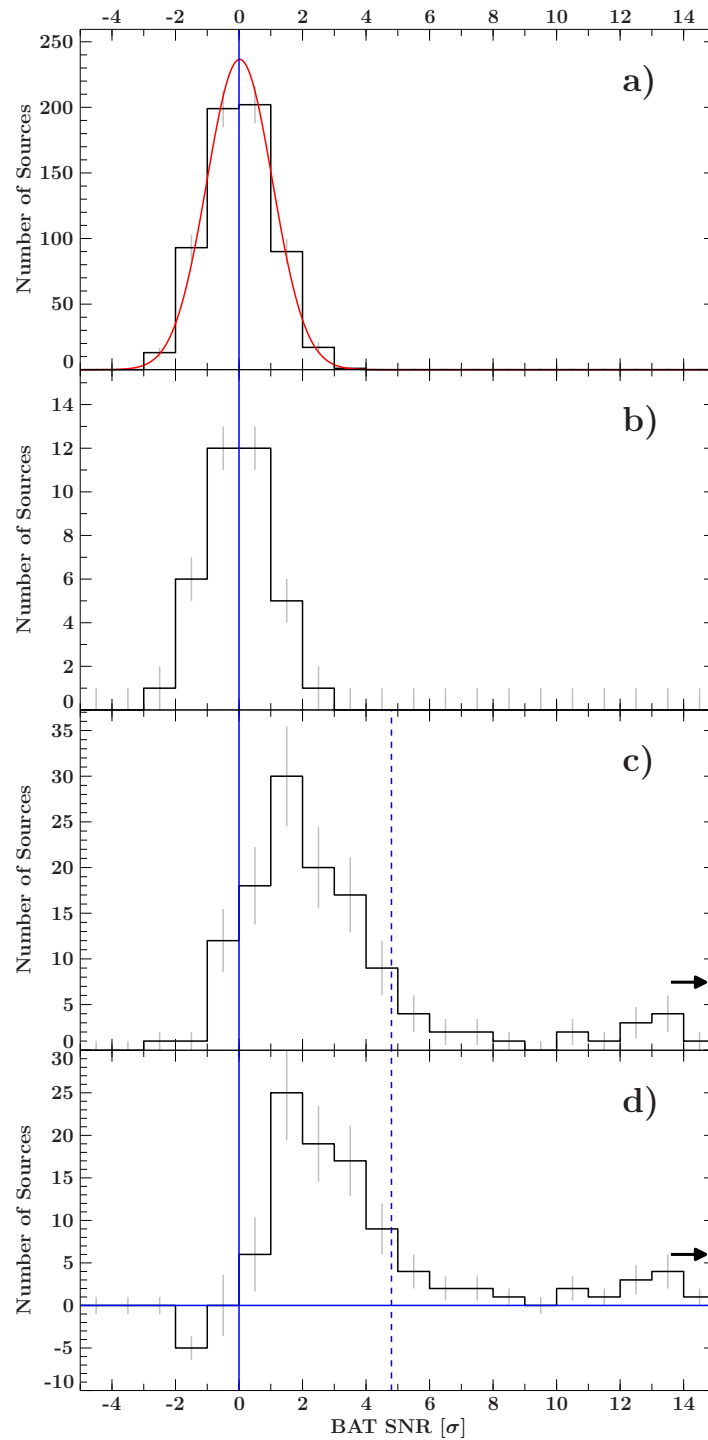


Figure 5.1: Distribution of *Swift*/BAT SNRs: a) blank sky distribution, fitted by a Gaussian curve, b) rescaled blank sky histogram, c) MOJAVE-1 sources, d) subtracted distribution c - b. Solid lines indicate 0σ , the dashed line 4.8σ , the cutoff value of the BAT 58 month catalogue. Arrows indicate the cutoff at 15σ .

- The brightest objects with SNR values roughly greater than 4.8σ , which significantly differ from the blank sky distribution. Six of all eight radio galaxies, 22 quasars, and one BL Lac are above this limit.
- Sources between 3σ and about 4.8σ that are still bright enough to use spectral fitting.
- Weak sources with positive SNR values that are designated as *faint*. One exception is the source 0422+004 at -0.06σ .
- Upper limits regarding flux calculation in the range of -2.0σ – 1.6σ . The subsample of upper limits consists of 21 quasars, five BL Lacs and three unidentified sources.

The number of quasars in the first category differs from the number detected in the 58-month BAT catalogue since the SNR value for the integrated time of 70 months changed below the 4.8σ limit for two quasars (1334-127 and 1458+718) and above the limit for one quasar (0552+398). The second and third category include the majority of all BL Lacs, with none of them registered in the 58-month BAT catalogue. A Kolmogorov-Smirnov test (KS test) revealed a p -value of 0.491 for the hypothesis that the BL Lacs originate from the same SNR distribution than the entire sample and a value of 0.601 compared to the subsample of quasars. The hypothesis of the same parent distribution for all sources and radio galaxies can be excluded with a p -value of 0.002.

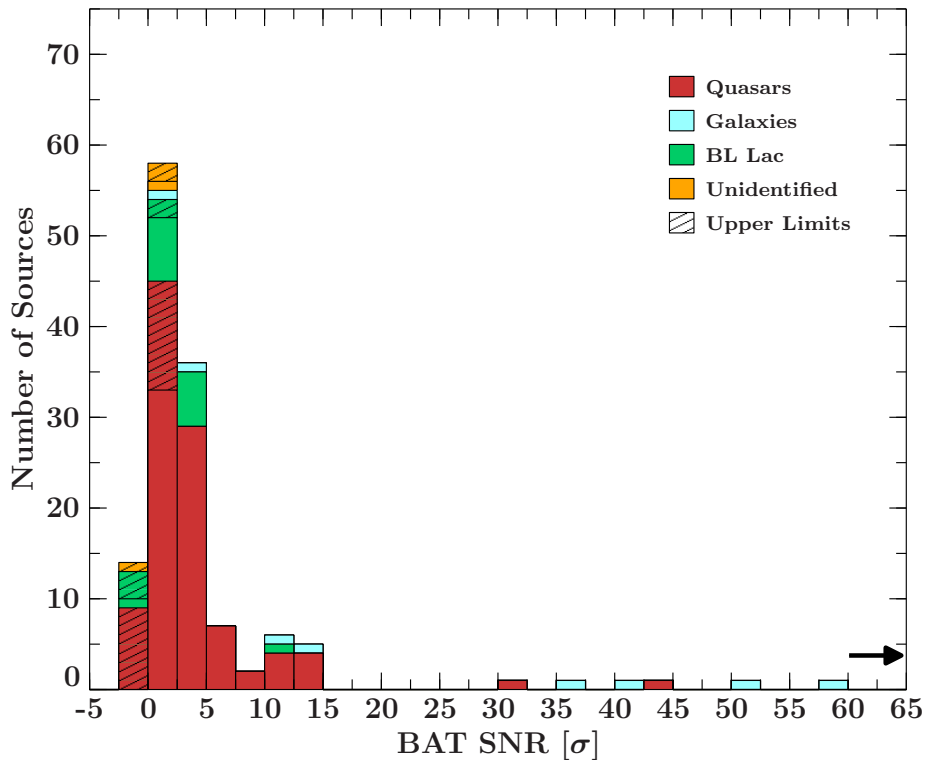


Figure 5.2: BAT SNR distribution of the MOJAVE-1 sample for different source classes. One source at 177σ has been omitted.

5.2 Hard X-rays: Statistical Properties of the Sample

This section comprises general properties of the entire sample and the distributions for the computed quantities flux and luminosity for the energy range 20–100 keV. The sets of data for photon index, fluxes and luminosity of every MOJAVE-1 source can be found in Table B.

5.2.1 Photon Indices Γ

The distribution of photon indices Γ is shown in Fig. 5.3, including only sources that have been classified as *bright*, i.e. with a BAT SNR $> 3.0\sigma$ (see Sect. 4.1.2). This distribution is the result of power-law fits of the corresponding X-ray spectra at 20–100 keV. Quasars form a bell-shaped distribution around 1.6, with minimum and maximum values of about 0.8 and 2.6, respectively. A greater range of photon indices is found for BL Lacs (about 0.8–3.6), while the minimum value diverts stronger from the mean compared to the group of quasars. BL Lac 0716+714 exhibits an extraordinary steep index of $\Gamma = 0.83^{+0.65}_{-0.81}$. The quasar 0917+624 and BL Lac 0754+100 above $\Gamma = 2.8$ are rather faint and very close to a SNR of 3.0σ with uncertainties well within the averaged corresponding photon index. Radio galaxies concentrate around $\Gamma = 2$ with the largest value at 3.54, belonging to the source 3C84 (0316+413).

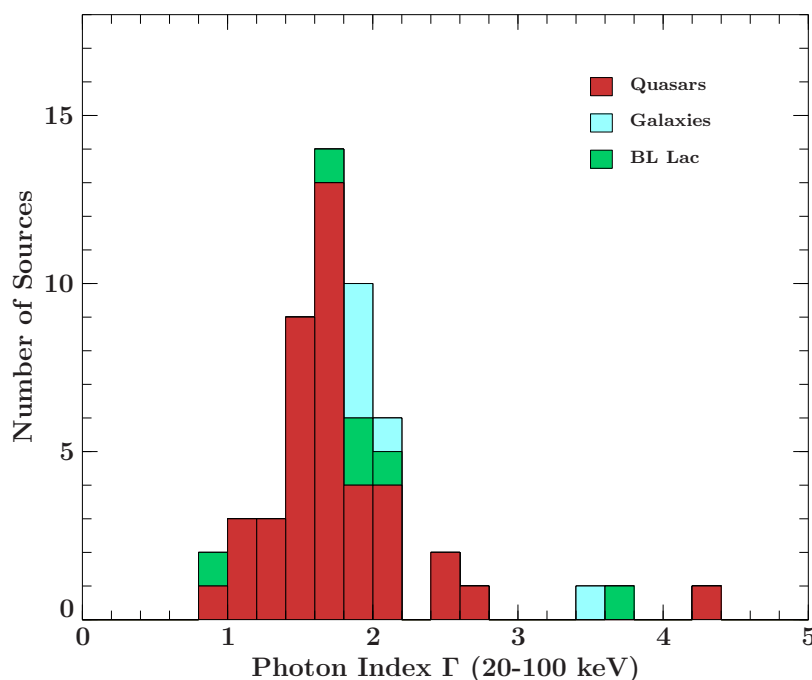


Figure 5.3: Distribution of photon index Γ of all bright MOJAVE-1 sources (BAT SNR > 3).

For all sources below a BAT SNR of 3.0 it is assumed that the sources have the average (mean) photon index of the corresponding AGN class of the bright subsample (see Sect. 4.1.1). The error is derived from the standard deviation of the type-specific photon index (Table 4.1).

The assumed photon indices for quasars and BL Lacs are 1.76 ± 0.54 and 1.99 ± 0.96 , respectively. Radio galaxies feature an averaged index of 2.18 ± 0.66 , including the source 3C84 with its deviant photon index of 3.53. Excluding this source results in an averaged index for radio galaxies of 1.91 ± 0.08 . For comparative reasons it is furthermore assumed, that the unidentified sources share the same averaged photon index as quasars.

5.2.2 X-ray Flux and Redshift Distribution

The histogram for the hard X-ray flux measurements is presented in Fig. 5.4. The method of determination for the flux of faint sources as described in Sect. 4.1.3 results in 29 upper limits, which is about 21% of the sample. The vast majority of 126 out of 135 sources lies below $20 \times 10^{-12} \text{erg s}^{-1} \text{cm}^{-2}$, with five quasars and four radio galaxies above this limit. Most of the sample, and especially BL Lacs and unidentified sources concentrate towards very low fluxes. The unidentified object 0446+112 shows a X-ray flux of $(3.15 \pm 0.12) \times 10^{-12} \text{erg s}^{-1} \text{cm}^{-2}$ which is comparable to most objects in the sample and significantly brighter than the other unidentified sources in the catalogue.

By applying a KS-test, it cannot be excluded that quasars and BL Lacs share the same parent distribution (p -value of 0.287). Performing the test for quasars and galaxies, the result of 0.003 shows a very high probability of a different distribution.

Figure 5.5 shows the redshifts of the sample with the different AGN types marked. For nine sources no information about the redshift is available, including all four unidentified objects in the sample. Nearby sources at low z , that can be resolved, are mostly radio galaxies, while quasars span over the entire range of observed redshifts. BL Lac objects feature redshifts < 1.2 . The entire sample peaks at $z \approx 0.7$, where the flux-related upper limits reach up to about 2. Radio galaxies, which have the highest X-ray fluxes in the sample, are amongst others the nearest objects.

5.2.3 X-ray Luminosity

The intrinsic K-corrected luminosities of the MOJAVE-1 sample in the hard X-ray band minus nine sources (no redshift and luminosity distance available) are graphed in Fig. 5.6. The missing sources are mainly BL Lacs and unidentified objects.

As opposed to the fluxes distribution, the luminosities do not clearly drop towards increasing values, and peak distinctively in the case of quasars. This bell-shaped distribution in $\log L$ centres around 10^{46} – $10^{47} \text{erg s}^{-1}$, with all BL Lacs and radio galaxies below $10^{46} \text{erg s}^{-1}$. The brightest sources are exclusively quasars with luminosities up to $10^{48} \text{erg s}^{-1}$ and upper limits up to $4 \times 10^{46} \text{erg s}^{-1}$. Radio galaxies possess lower luminosities around 10^{41} – $10^{45} \text{erg s}^{-1}$, while BL Lacs have minimum values of about $10^{43} \text{erg s}^{-1}$. In contrast to the flux distribution, the group of radio galaxies meets to be the least X-ray luminous type, an effect of the low redshift.

At this point, it is not clear, if the distribution of upper limits is still in agreement with the distribution of measured fluxes. Applying a KS-test for the luminosity, p -values of 0.274 for quasars and 0.328 for BL Lacs are found. Besides this, the different AGN classes most definitely do not follow a common distribution respectively shown by p -values of the order of 10^{-6} .

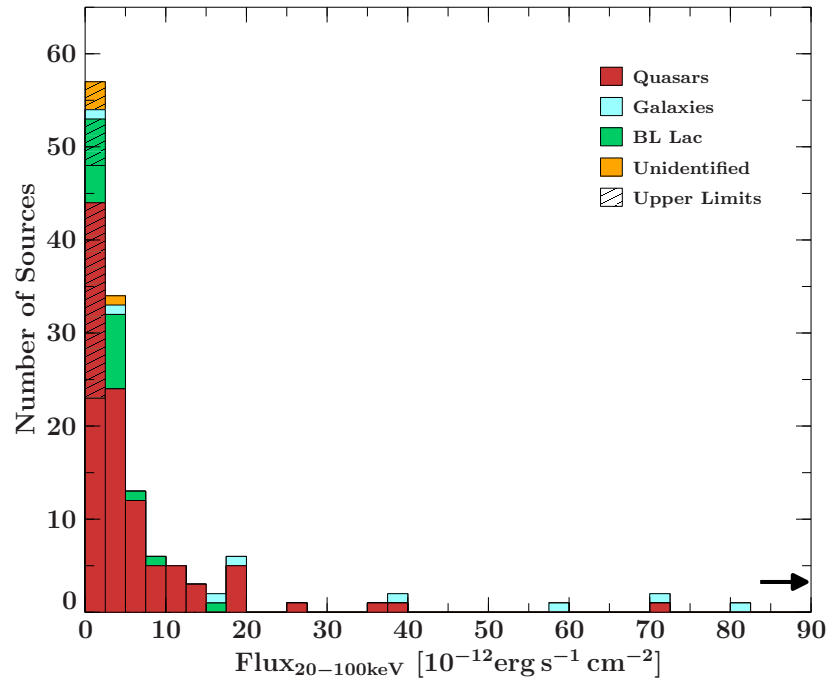


Figure 5.4: Distribution of hard X-ray flux of MOJAVE-1 sources with BAT SNR > 3 . One source at $258 \times 10^{-12} \text{ erg s}^{-1} \text{ cm}^{-2}$ has been omitted.

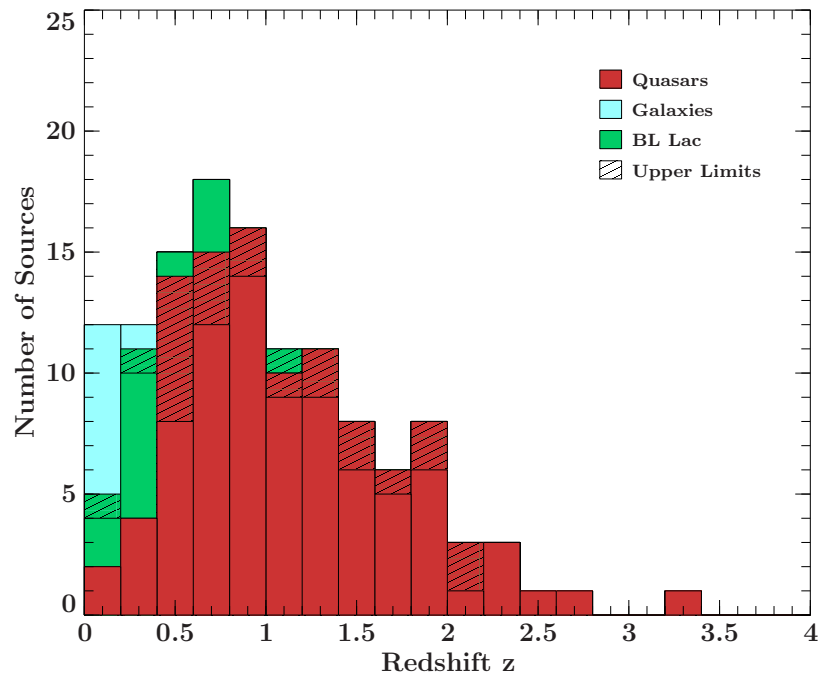


Figure 5.5: Distribution of Redshift z (126 of 135 sources of the MOJAVE-1 sample shown).

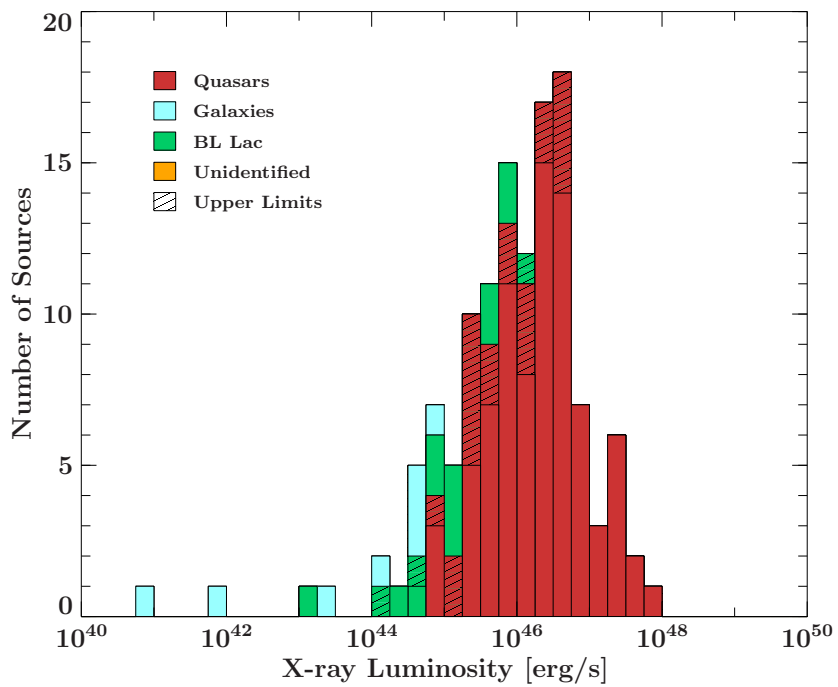


Figure 5.6: K-corrected X-ray luminosity distribution of the MOJAVE-1 sample for the energy range of 20 - 100 keV. The upper limits correspond to X-ray flux calculation.

5.3 Correlation Studies

In this section, the results of correlation tests between the hard X-ray band of *Swift*/BAT and the MOJAVE radio properties are presented. Results of different observational techniques for the radio band are compared to the X-Ray features. The concerning radio measurements as published in Kovalev et al. (2005) are:

- Total: Single dish measurement of the object.
- VLBA: Equals the sum of the flux densities of all jet components of the map.
- Unresolved: Defined as a limit of the visibility function amplitude S_C with 90% of all visibilities below at baselines $r_{uv} > 360 \text{ M}\lambda$.
- Core: Flux density of the core component at the end of the jet.
- Jet: Flux measurements $F_{\text{VLBA}} - F_{\text{core}}$. Corresponds to the flux density of the AGN's jet.

In the following, studies relating to the correlation behaviour of the MOJAVE-1 sample are divided into results for the entire sample as well as for the subsamples quasars, radio galaxies, BL Lacs and unidentified sources after Véron-Cetty & Véron (2003).

5.3.1 Radio and X-ray Flux

Figure 5.7 displays the flux relation of the MOJAVE-1 sample for hard X-rays and the radio VLBA measurement in logarithmic scaling. The dashed line represents a linear regression for all types of sources without taking into account the upper limits:

$$\log(F_X) = a + b \cdot \log(F_R) \quad (5.1)$$

with the y-intercept a and the slope b , which corresponds to a power-law relation in the form of

$$F_X = 10^a + F_R^b \quad (5.2)$$

The lower panel of Fig. 5.7 shows the residuals in units of standard deviation σ regarding data points and linear regression. For a representative linear regression, a symmetrical distribution around 0σ would be expected, forming a Gaussian curve when graphed as a histogram. The corresponding distribution is presented in Fig. 5.8, showing the majority of the sources located at -2 – 1σ and an excess of a small number of sources up to about 3.4σ . Objects of the latter group are generally very bright AGN with small uncertainties and a high portion of radio galaxies. The histogram also features a small gap closely below 0σ , indicating a slight separation of X-ray brighter and fainter sources along the regression line.

The graphs for all other radio quantities are shown in the Appendix in Fig. A.1. Different groups corresponding to their optical classification can be recognized to have a significant positive correlation in terms of hard X-ray to radio flux. Table 5.1 shows the correlation coefficient and parameters for the linear regression for X-ray and radio fluxes. With the exception of the quasar 0420-014 that exhibits a strong radio flux at about 10 Jy in all but the jet measurement, all the upper limit sources lie below 3.5 Jy. Since the group of unidentified objects is composed of three out of four upper limits, no linear regression and correlation coefficient has been calculated.

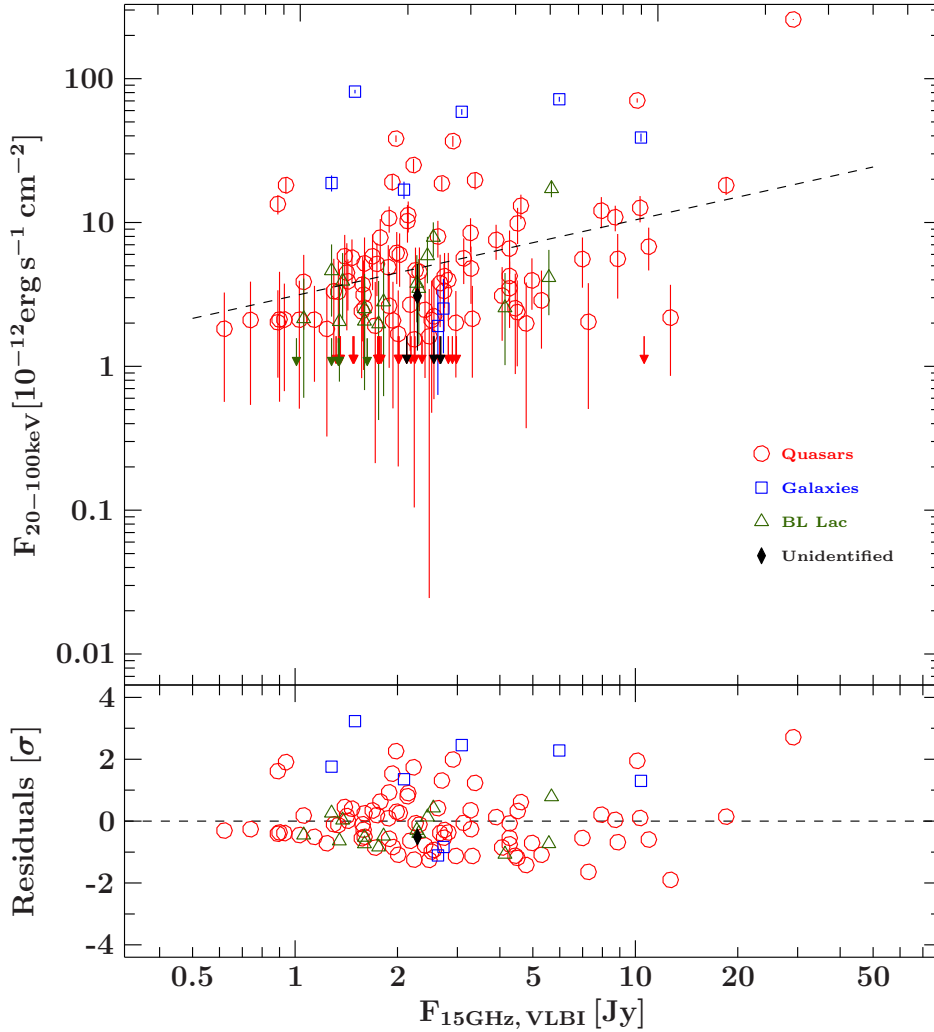


Figure 5.7: The Relation of hard X-ray (20–100 keV) to VLBA radio flux is shown in the upper panel. The dashed line indicates a linear regression for all sources except upper limits. The lower panel shows the residuals for the sample regarding the linear regression.

Overall, the slope of the linear regression for the entire sample is dominated by the distribution of quasars, which is steeper for the total and VLBA observations. The slope of galaxies features very large relative errors due to their small sample size. Differences of the slopes of total (single-dish) and VLBA observation are only prominent for galaxies, changing from 0.20 to 0.41 . Looking at the data of the unresolved measurement, one sees that the slopes of the entire sample, quasars and galaxies tend to be flatter while BL Lacs stay about the same. Going from VLBA to core measurements, the slopes are even flatter except for galaxies with 1.88 ± 1.60 in contrast do 0.41 ± 0.84 (VLBA). However, the reduced sample size from 8 to 5 due to unavailable data for the core leads to a even higher uncertainty. The lowest values for the slope of the X-ray radio flux relation have been determined for the jet observations, i.e. the VLBI flux subtracted by the core flux, again with the exception of galaxies.

To estimate the correlation behaviour of X-ray to radio flux, the Spearman correlation

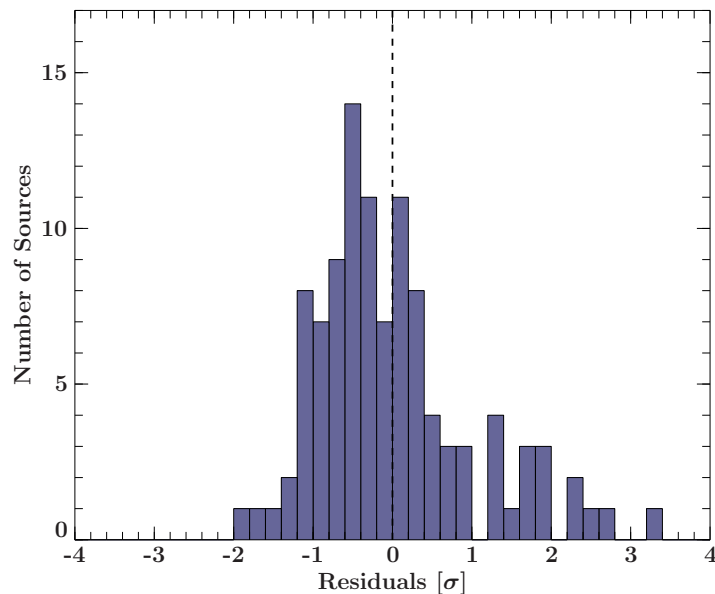


Figure 5.8: Distribution of residuals for the linear regression of Hard X-ray and radio flux (see also Fig. 5.7).

coefficients ρ have been calculated for every AGN classification and radio measurement (Table 5.1). The complete sample as well as the subsample of quasars exhibit a similar behaviour for ρ throughout all radio measurements. With values of about 0.22–0.34, the entire sample and the group of quasars seem to have a moderate correlation between hard X-ray (20–100 keV) and radio (15 GHz) emission which is assured by a relatively large sample size of 135 and 103 sources. In contrast, the low sample sizes of galaxies (eight sources with no information about core and jet emission for three) features the greatest fluctuations of ρ . galaxies seem to be significantly correlated for core and jet measurements with $\rho \approx 0.6$ and weakly for single dish and VLBA ($\rho \approx 0.15 - 0.36$). With 15 sources, the class of BL Lacs are the strongest correlated AGN type in the sample with $\rho \approx 0.5$ for all radio measurements, except the jet component with very little correlation therein. Eventually, the validity of the determined correlation coefficients can only be assumed for the entire MOJAVE-1 sample and the set of quasars.

5.3.2 Radio and X-ray Luminosity

The X-ray luminosity values were determined for 126 of 135 sources because of missing data for the redshift of nine sources. In addition, missing measurement values for three radio galaxies for the core observation reduce the number of galaxies in this case to five. Measurement values for the jet component are only determined by four galaxies since the flux for VLBA and core are equal for the source 0007+106. Like the previous section concerning the X-ray fluxes, this part encompasses the results regarding linear regressions and correlation coefficients for the relation X-ray (20–100 keV) to radio (15 GHz) luminosity. Furthermore, the results of a partial correlation analysis after Akritas & Siebert (1996) are shown. The exemplary plot of X-ray luminosity against VLBA radio luminosity is shown in Fig. 5.9, while the plots for the remaining radio measurements can be found in Fig. A.2 in the Appendix.

	Number of Sources	Correlation Coefficient	a (y-intercept)	b (slope)
Total				
All Sources	106 / 135	0.34	0.47 ± 0.16	0.55 ± 0.11
Quasars	82 / 103	0.31	0.48 ± 0.18	0.51 ± 0.13
Galaxies	8 / 8	0.36	1.11 ± 0.64	0.20 ± 0.41
BL Lacs	15 / 20	0.47	0.33 ± 0.52	0.65 ± 0.28
VLBA				
all sources	106 / 135	0.30	0.50 ± 0.16	0.55 ± 0.13
Quasars	82 / 103	0.28	0.49 ± 0.18	0.51 ± 0.13
Galaxies	8 / 8	0.14	1.10 ± 0.68	0.41 ± 0.84
BL Lacs	15 / 20	0.54	0.34 ± 0.47	0.67 ± 0.26
Unresolved				
all sources	106 / 135	0.22	0.68 ± 0.12	0.24 ± 0.13
Quasars	82 / 103	0.27	0.62 ± 0.13	0.39 ± 0.13
Galaxies	8 / 8	0.24	1.31 ± 0.36	0.26 ± 0.86
BL Lacs	15 / 20	0.49	0.44 ± 0.39	0.51 ± 0.31
Core				
all sources	103 / 132	0.31	0.62 ± 0.13	0.36 ± 0.14
Quasars	82 / 103	0.28	0.62 ± 0.15	0.31 ± 0.14
Galaxies	5 / 5	0.60	0.81 ± 0.88	1.88 ± 1.60
BL Lacs	15 / 20	0.46	0.45 ± 0.37	0.46 ± 0.28
Jet				
all sources	103 / 132	0.24	0.83 ± 0.12	0.28 ± 0.07
Quasars	82 / 103	0.22	0.81 ± 0.14	0.23 ± 0.07
Galaxies	5 / 5	0.40	0.95 ± 0.83	1.07 ± 1.29
BL Lacs	15 / 20	0.14	0.66 ± 0.41	0.16 ± 0.15

Table 5.1: Spearman correlation coefficient and parameters for linear regression of X-ray and radio fluxes in logarithmic scaling after $\log(F_X) = a + b \cdot \log(F_R)$. The notation for numbers is: number without / with upper limits.

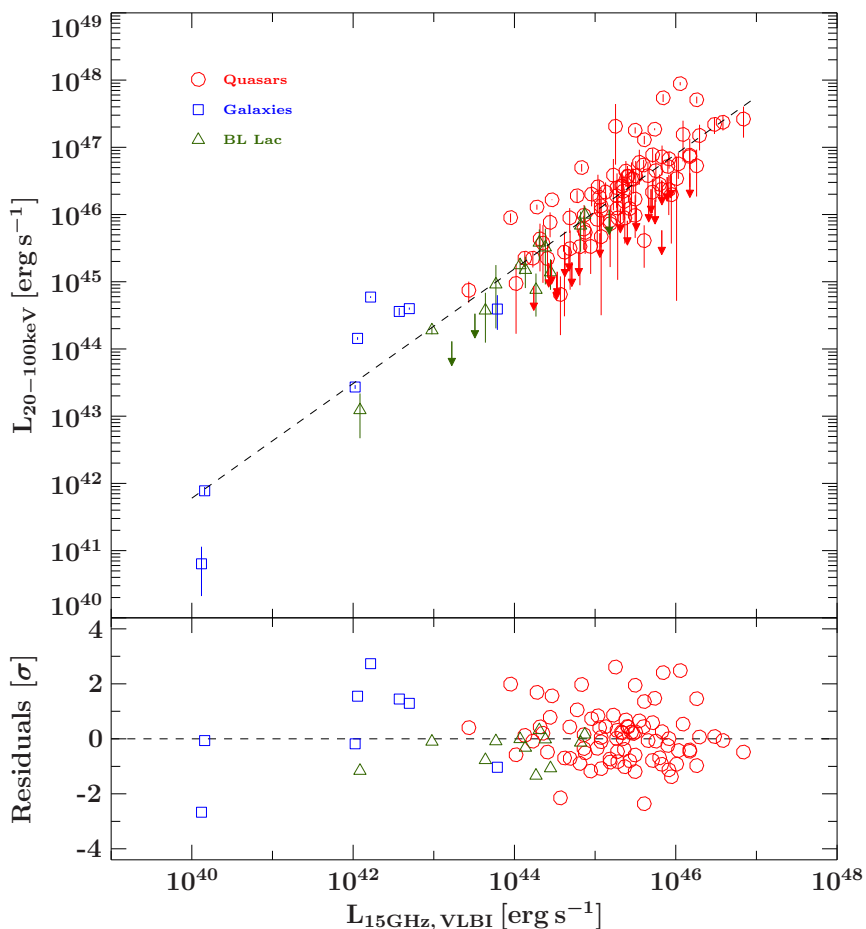


Figure 5.9: The Relation of hard X-ray (20-100 keV) to VLBA radio luminosity is shown in the upper panel. The dashed line indicates a linear regression for all sources except upper limits. The lower panel shows the residuals for the sample regarding the linear regression.

Looking at the graphs and calculated correlation coefficients, one recognises a high positive correlation between the luminosities of both wavelength bands. However, this picture is misleading since the shown distribution of data points is stretched due to the fact, that both luminosities have been calculated with the same redshift (see Sect. 4.3.2). Therefore, the values for partial Kendall's Tau have been determined which exclude the dependencies for a third parameter (the redshift z) and express the relational quality of the luminosities of the sample. The results for correlation coefficient, linear regression and partial Kendall's Tau are listed in Table 5.2. The determined parameters of the lines for the linear regression only serve as a qualitative estimation about the X-ray and radio correlation of the different sources types to each other.

In all plots the classes have distinct areas in which they are occurring. Quasars form the bright, radio galaxies the fainter end of the stretched-out distribution. BL Lacs are found in the intermediate region and intersect with the other two types. The group of upper limits lies above about $10^{43} \text{ erg s}^{-1}$ ($10^{44} \text{ erg s}^{-1}$ for the group of quasars), which is about approximately the middle of the plotted distribution in the radio band. This set of sources forms a sequence that is distributed at the lower part but also yet within the band of all other

sources. The data points of all source types, graphed against the different radio luminosities, are distributed in a very similar way with the exception of the jet measurement, which is scattered notably wider. The correlation coefficient for all object classes about 0.1 greater than in other measurement types.

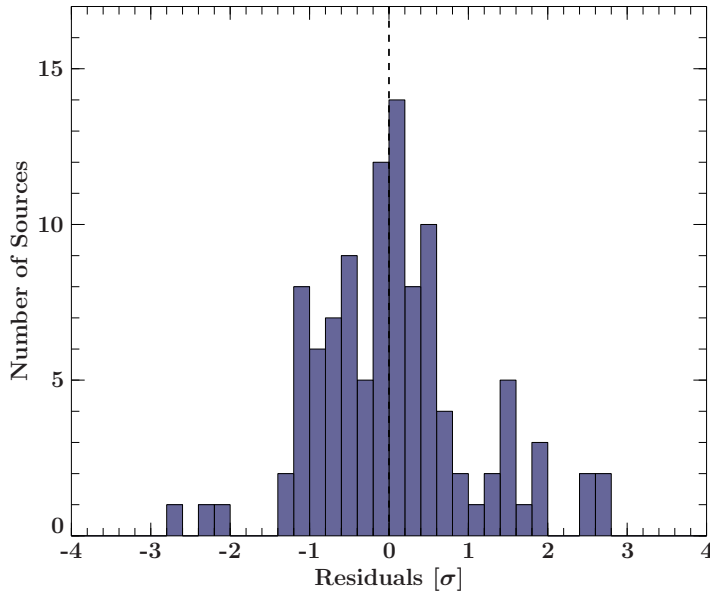


Figure 5.10: Distribution of residuals for the linear regression of Hard X-ray and radio flux (see Fig. 5.9).

The slopes of BL Lacs differ the most throughout the radio measurements with values of ≈ 0.76 – 0.96 . The most static slope is featured by the group of quasars with about 0.71 – 0.79 , when excluding the flat slope of 0.54 from the jet measurement. The steep slope of galaxies up to ≈ 1.45 is likely due to a very small sample size of four objects for one observation. For all types the value reaches from 0.78 to 0.91 , a trend that is dominated by the numerous quasars. Even though the slopes of all types mutually compatible within their uncertainties (except quasars and galaxies for the jet and galaxies for the core measurement) certain tendencies in terms of X-ray and radio correlation can be expressed. BL Lacs seem to be higher correlated than quasars. An estimation about radio galaxies remains difficult because of the small sample size.

Much more significant for the comparison and validity of correlation between X-ray and radio luminosity, the partial Kendall’s Tau is addressed. While taking into account all upper limits, a significant partial correlation appears for the entire MOJAVE-1 sample (123–126 sources) and the quasar subsample (103 sources) for all radio measurements at a uncertainty level of 0.05 (Table 5.2). Total and core measurement exhibit the strongest correlations, values for the jet observation are lowest. Values for τ/σ change considerably for galaxies and BL Lacs. Furthermore, the results of the test are less erratic when using a less conservative definition of upper limits, i.e. a lower number of upper limits. The correlation after partial Kendall’s Tau of luminosities is strongest for the complete sample. The distributions of galaxies and BL Lacs have little influence on the correlation of the sample compared to the quasars that outline the majority of AGN types.

For the core and jet component the algorithm did not provide a valid result for galaxies

as in the determination of τ division by zero occurs. This is a not avoidable side effect that may happen for very small samples. For BL Lacs no recognizable correlations were found ($\tau/\sigma \leq 0.61$).

	Number of Sources ^a	Corr. Coefficient	a (y-intercept)	b (slope)	τ^b	τ/σ^c	Corr. ^d
Total							
All Sources	102 / 126	0.88	5.27 ± 3.98	0.91 ± 0.04	0.25	4.85	Y
Quasars	82 / 103	0.80	10.47 ± 7.73	0.79 ± 0.07	0.23	4.21	Y
Galaxies	8 / 8	0.95	1.06 ± 12.88	1.00 ± 0.26	0.71	1.70	N
BL Lacs	12 / 15	0.86	2.77 ± 16.91	0.96 ± 0.09	0.02	0.12	N
VLBA							
all sources	102 / 126	0.89	7.66 ± 3.72	0.85 ± 0.03	0.24	4.62	Y
Quasars	82 / 103	0.80	10.44 ± 7.72	0.79 ± 0.07	0.22	4.10	Y
Galaxies	8 / 8	0.83	-1.18 ± 12.67	1.07 ± 0.21	0.28	0.87	N
BL Lacs	12 / 15	0.86	2.92 ± 16.79	0.96 ± 0.08	0.02	0.12	N
Unresolved							
all sources	102 / 126	0.87	10.25 ± 3.52	0.80 ± 0.04	0.21	4.40	Y
Quasars	82 / 103	0.79	10.85 ± 7.95	0.79 ± 0.07	0.20	3.91	Y
Galaxies	8 / 8	0.67	3.02 ± 11.60	0.98 ± 0.20	-0.14	-1.61	N
BL Lacs	12 / 15	0.85	5.51 ± 15.95	0.90 ± 0.09	0.00	0.00	N
Core							
all sources	99 / 123	0.87	8.90 ± 4.05	0.83 ± 0.04	0.23	4.96	Y
Quasars	82 / 103	0.80	14.10 ± 7.26	0.71 ± 0.07	0.22	4.53	Y
Galaxies	5 / 5	0.90	-17.01 ± 19.39	1.45 ± 0.14			N*
BL Lacs	12 / 15	0.86	6.12 ± 15.75	0.89 ± 0.09	0.09	0.61	N
Jet							
all sources	99 / 123	0.80	11.44 ± 4.06	0.78 ± 0.05	0.23	3.92	Y
Quasars	82 / 103	0.70	22.20 ± 5.88	0.54 ± 0.06	0.21	3.26	Y
Galaxies	4 / 4	0.30	-16.46 ± 20.84	1.44 ± 0.24			N*
BL Lacs	12 / 15	0.75	10.99 ± 16.43	0.79 ± 0.19	0.06	0.51	N

Table 5.2: Spearman correlation coefficient and parameters for linear regression of X-ray and radio luminosity in logarithmic scaling after $\log(L_X) = a + b \cdot \log(L_R)$ (without upper limits) and results of partial correlation analysis (upper limits included). ^a number without / with upper limits. ^b Partial Kendall's Tau after Akritas & Siebert (1996), ^c Tau divided by Variance, ^d Correlation present after partial correlation analysis at level 0.05. The asterisk indicates no valid result for the Tau algorithm (but highly probable zero correlation)

5.3.3 Jet Velocity and Luminosity

The AGN sample of the 2cm survey used in Cohen et al. (2007) with 119 radio-selected sources greatly intersects with the MOJAVE-1 sample. The distribution of apparent jet velocities vs. apparent radio luminosity in Fig. 2.5 was also found for the radio measurements of the MOJAVE-1 sample after Kovalev et al. (2005). As shown in Fig. 5.11 (left panel) and Fig. A.3 tendencies of the distribution of the various source classes are shown in all radio measurements likewise. Quasars outline the brightest objects and the jets with the highest velocities, while radio galaxies feature opposite properties. BL Lacs are distributed between the other two classes and in addition possess higher jet speeds for objects with higher luminosity. The right panel of Fig. 5.11 shows jet velocity against the hard X-ray luminosity including upper limits. The positional tendency of the object classes as mentioned can also be recognized in this plot. Upper limit sources, i.e. objects with intrinsically very faint hard X-ray emission are distributed up to jet velocities of about 25 c , with the vast majority of all sources below this limit.

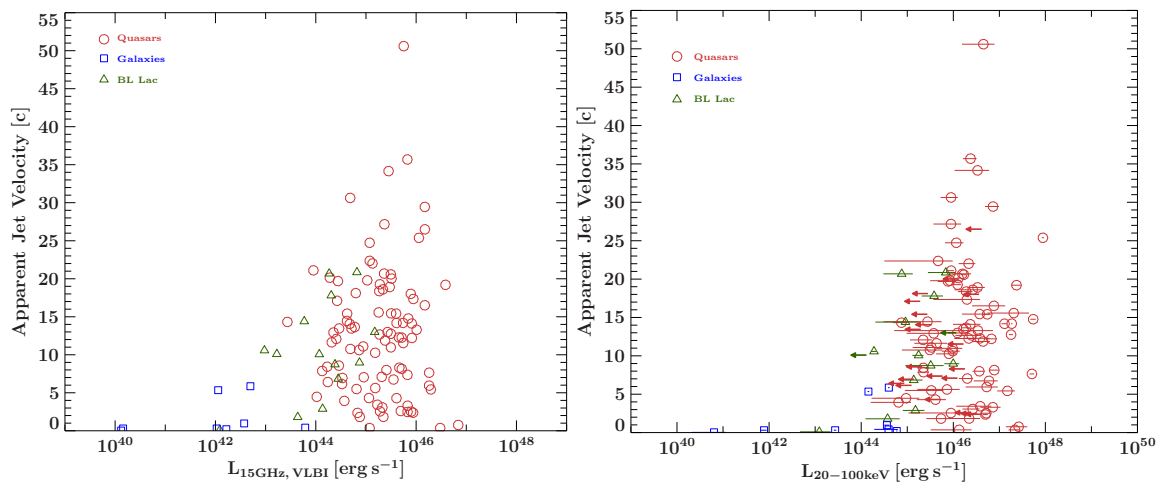


Figure 5.11: Apparent jet velocity in units of c against VLBA radio luminosity (left panel) and hard X-ray luminosity (right panel).

6 Discussion

BASED on the results of spectral fitting and the subsequent statistics and relations, this chapter focusses on the discussion of further implications regarding the X-ray properties of the MOJAVE-1 sample itself, as well as the relation of the spectral shape and luminosity of blazars. Section 6.1 addresses the cases of X-ray bright sources that feature atypical photon indices, that are the results of spectral fitting with a simple power-law. The distribution of X-ray flux and luminosity and the implications for source count statistics as well as selection biases for the sample are discussed in Sect. 6.2 and 6.3, respectively. The application of spectral slopes for *Swift*/BAT and *Fermi*/LAT measurements regarding the blazar sequence is approached in Sect. 6.4.

6.1 Spectral Shape and Photon Index

The distribution of photon indices of all sources in the MOJAVE-1 sample that are bright enough for spectral fitting shows an approximately bell-shaped form around typical values for AGN. Due to the compromise of a limiting SNR value above which fitting is still considered reasonable, a small number of weak, but still as bright classified, sources show relatively large uncertainties in their photon indices. This limit, which was half empirically and arbitrarily set to 3.0σ , leads to the noticeable high indices above $\Gamma \gtrsim 2.8$ for two sources, and could as well be raised to a value that would prevent too large fluctuations of the overall photon index because of poor quality spectra, on the cost of a less representative averaged index. However, the averaged values Γ_{av} can be recognized as typical AGN photon indices. Compared to the *Swift*/BAT X-ray survey by Ajello et al. (2008), they match within their uncertainties with the group of radio-loud AGN and Seyfert galaxies: $\Gamma = 1.66$ and $\Gamma = 2.00$, respectively (six of all eight radio galaxies in the MOJAVE-1 sample can be classified as Seyfert galaxies after the 58-month BAT catalogue). Another possible explanation for the atypical photon indices of sources with SNRs closely above 3 sigma may be the difficulty of assigning uncertainties to spectra with very low count rates.

A quite different example is radio galaxy 3C84 (0316+413) exhibits a very unusual photon index if $\Gamma = 3.54$, which is not the result of the fitting of weak count rates. Actually, the source is very bright at hard X-rays (BAT SNR = 50.9σ). However, another factor than the quality of the count rate spectrum has to be taken into account. This source is located in a cluster of galaxies, the Perseus cluster. Hot intergalactic gas radiates at energies in the range of keV (Fabian, 2001). This leads to a spectral energy distribution that cannot be described by a simple power-law fit used for the non-thermal emission of AGN at hard X-rays. The power-law fit statistic of $\chi_{\text{red}}^2 = 3.79$ illustrates this issue.

Another noticeable and interesting case is the BL Lac object 0716+714. Both soft and hard X-ray photon indices observed by XRT and BAT are not compatible and suggest a different spectral shape next to each other. Figure 6.1 shows the photon indices obtained by XRT in the time between January 2005 and September 2012 (Langejahn et al., 2013). The averaged index was determined to be $\langle\Gamma_{\text{XRT}}\rangle = 2.05 \pm 0.21$ with the uncertainty of one standard deviation, implying a fluctuation around a flat spectral energy distribution in the

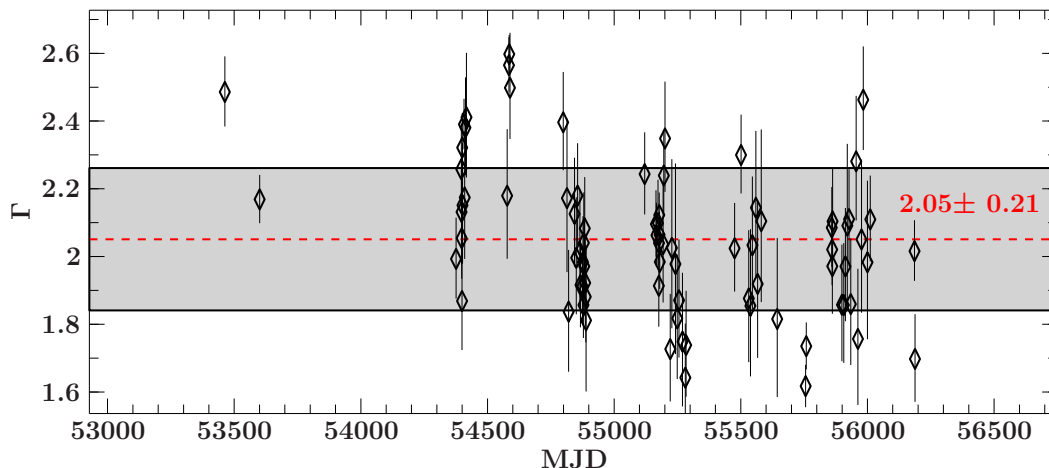


Figure 6.1: Soft X-ray photon index Γ for XRT observations of BL Lac 0716+714 between January 2005 and September 2012. The red line indicates the mean value, the gray box one standard deviation.

soft X-ray regime (2–10 keV) as opposed to the spectral behaviour observed by BAT with a photon index of $\Gamma_{\text{BAT}} = 0.83^{+0.65}_{-0.81}$. This particular object is known to be highly variable on a multitude of frequencies over short time scales (e.g. Wagner et al., 1996). The determined indices imply that BAT (20–100 keV) detected the spectral range of the left side of the rising IC emission peak, while XRT (0.2–10 keV) observed the gap between IC and synchrotron peak, explaining the vivid fluctuation around a ”flat” spectral energy distribution. Although it seems remarkable that 0716+714 is the only source in the sample that exhibits such a steep photon index for BAT, the majority of the MOJAVE-1 sample still needs to be checked for similar behaviour, which requires higher quality spectra.

Beneath the used method for determining Γ_{av} and the corresponding error for each class (Sect. 4.1.3), two other different approaches were tested. One method uses a Gaussian fit to the distribution of the photon indices of the bright sources and estimates the error of this distribution via the curve’s FWHM. However, this approach may not be an appropriate estimate due to the small sample size. The other method determines the mean value of the indices and assumes the highest and lowest values for the range of errors, which is likely too generous and often due to only one or two atypical indices far from the mean. Compared to the results of the method used in this work, all photon indices of bright and faint sources are compatible within their uncertainties.

6.2 X-ray Flux and Luminosity Distribution

Although the AGN in the sample can reasonably be characterized as hard X-ray emitters, properties in the energy band of 20–100 keV can only be estimated for a certain portion of the sources. This encompasses sources at low BAT SNR values closely to 3.0 (see previous section) and, of course, all 29 upper limits.

Especially for the upper limit sources better observational data is needed to clarify how strong the hard X-ray output of these objects really is. The nine-year Galactic survey catalogue of INTEGRAL/IBIS (Krivonos et al., 2012) for example only shares seven common

sources with the MOJAVE-1 sample, most of them bright X-ray emitters as measured by BAT. Another approach for further restrictions of the intrinsic luminosity of the X-ray upper limits in the used sample could be made on the basis of hard X-ray emission models within the jet (e.g. the SSC model). Following the methodology in Cohen et al. (2007) and under the assumption of a certain Doppler factor and luminosity a similar envelope for various inclination angles could potentially be fitted to the measured luminosities and jet speeds (see Sect. 2.3 and 5.3.3).

Calculating the X-ray fluxes and luminosities for less conservative criteria regarding upper limit definition leads to a even fainter while also smaller set of upper limits. The distance towards other sources in luminosity space possibly suggests a separate and new group of hard X-ray faint and radio-loud AGN. This assumption remains risky, because of insufficient or low quality data and needs to be confirmed or rejected with the help of further observations. Since the gathered spectra of BAT already encompasses 70 months of survey data, and signal strength only increases as a function of the square root of time, it suggested to either combine observational data with other instruments, or to use new and much more sensitive pointed observations. The former option may be applicable to a small number of weak and upper limit sources, because intersections between hard X-ray data sets are also generally small, due to different observational strategies (see SIX-survey in Sect. 3.2.1). An ideal candidate for more effective pointed observations of weaker sources is the X-ray mission *NuSTAR* (Harrison et al., 2010), launched in June 2012 by NASA. The focussing optics and detector of *NuSTAR* reach a sensitivity of about 1000 times that of BAT at 10–30 keV and takes measurements in the energy range of 6–79 keV, bridging the gap between XRT and BAT in the X-ray regime (NuSTAR Galactic Science Team).

When comparing measured fluxes of multiple objects, that are distributed over a large scale of distance, selection effects for the objects becomes an issue. Nearer sources appear brighter while faint sources may not be detected at all at higher distances. The MOJAVE-1 sample is clearly biased towards higher fluxes because of the wide distribution of redshifts up to ≈ 3.5 . This effect, influencing the distribution of luminosity in the sample, is known as the Malmquist bias (see Sect. 1.1.4). This circumstance is also be illustrated by source count graphs, which display the spatial distribution of luminosities (Sect. 6.3).

In a recent study by Maselli et al. (2010), the blazar content for the first 39 months of BAT observations in the range of 15–150 keV for different significance levels was presented. Based on one of the most complete lists of blazars, the *Roma-BZCAT* Catalogue (Massaro et al., 2009), including 2837 sources in the version of April 2009, a cross-correlation with the BAT significance map resulted in 121 blazars detected at a BAT SNR of $> 3\sigma$. This sample consists of 20% BL Lacs, 57% FSRQs, and 23% sources of uncertain classification. In comparison, the MOJAVE-1 sample is composed of 16% BL Lacs and 75% quasars. The averaged hard X-ray fluxes in the first sample are approximately equal for FSRQs and BL Lacs, with $19.6 \times 10^{-12} \text{ erg s}^{-1} \text{ cm}^{-2}$ and $19.4 \times 10^{-12} \text{ erg s}^{-1} \text{ cm}^{-2}$, respectively. In contrast for the MOJAVE-1 sample, the X-ray flux for quasars are more than double the flux for BL Lacs, with $10.5 \times 10^{-12} \text{ erg s}^{-1} \text{ cm}^{-2}$ and $4.5 \times 10^{-12} \text{ erg s}^{-1} \text{ cm}^{-2}$, respectively. The difference in both portions of AGN classes between the samples as well as the observed flux for the classes can be explained by selection effects (e.g. Padovani et al., 2012). Whilst the sample assembled by Maselli et al. (2010) can be regarded as more representative regarding hard X-ray properties of blazars, this shows again the strong radio bias of MOJAVE.

This circumstance has also been shown by the result of only small correlational behaviour

between radio and X-ray fluxes (Sect. 5.3.1), despite of significant correlations for the corresponding luminosities (Sect. 5.3.2). Furthermore, Feigelson & Berg (1983) showed that the using luminosities instead of fluxes is more effective when seeking a correlation between both energy bands.

However, the challenging part of comparing X-ray and radio fluxes as well as luminosities for correlations is, first, the appliance of a linear regression onto a set of logarithmic graphed data points that are not distributed symmetrically around the regression line, secondly, the artificially stretched distribution in luminosity space, and thirdly, subsamples of AGN classes that are too small to make profound statements about possible correlations. The first item points out that the used method of linear regression is only suitable for Gaussian-distributed data points, which is not clearly the case. While applying a power-law fit to the data in the linear space would be a more adequate approach, it remains doubtful whether the results of this method would reveal more information about a distribution where linear regression only serves as a rough and qualitative estimation of the behaviour of the sample. Looking at the residuals of both regressions for flux and luminosity (compare histograms in Fig. 5.8 and Fig. 5.10), one recognizes a more symmetric distribution for the plot of X-ray against radio luminosities. This is probably due to the fact that the linear regression line is better able to describe a distribution, that has been stretched, forming an elongated accumulation of data points. The effect of artificially skewed distributions can be eliminated by an analysis for partial correlation. This approach, along with the calculation of Partial Kendall's Tau (Sect. 5.3.2) greatly depends on the size of the used sample. Both the whole sample (102 sources) and the group of quasars (82) show significant correlation under the elimination of the influence of redshift at a level of 0.05. Although both groups of BL Lacs (15) and radio galaxies (8) do not show a significant correlation of luminosity, the noticeably variable results of τ/σ for slightly different starting parameters suggest that the test is not as expressive for small sample sizes than for larger ones. It cannot be excluded, that the intrinsic luminosity of BL Lacs and radio galaxies in the radio and hard X-ray band are also correlated like the group of quasars. A larger sample of at least about 30 to 50 objects is roughly estimated to be needed for more expressive results.

6.3 Source Count Statistics

In order to test how the X-ray and gamma-ray flux distributions of the radio-selected MOJAVE-1 sample are spatially spread and detected, source count diagrams $\text{Log}(N)\text{-Log}(S)$ are plotted. These graphs are cumulative distributions which display the amount of sources with at least one specific flux value. The variable S is synonymous with the flux F , commonly used in radio astronomy. In a similar manner, the number of sources has been graphed against the intrinsic luminosity L for different redshift intervals to make estimations about detection biases for distant objects.

6.3.1 $\text{Log}(N)\text{-Log}(S)$ Distribution

For uniformly distributed objects in space and under the assumption of a Euclidian non-evolving Universe, a distribution of a power-law $N \propto S^{-3/2}$ is expected. The $\text{Log}(N)\text{-Log}(S)$ diagrams are shown in Fig. 6.2. In each case the groups of radio galaxies and unidentified objects has been excluded, leaving 123 sources. The count distribution for the 15 GHz VLBA measurement (Kovalev et al., 2005) follows a slope of $-3/2$ very precisely even for the

radio-faintest objects. For hard X-ray fluxes (20–100 keV) from BAT a slightly diverging relation appears compared to the first one. Numbers for the sources at fluxes below $\approx 10^{-11} \text{ erg s}^{-1} \text{ cm}^{-2}$ also follow the expected slope but are falling above. The gray shaded region corresponds to BAT SNR values of $\approx 4.8\sigma$, just the threshold value for the *Swift*/BAT 58-month catalogue and the more recent 70-month catalogue. Roughly in this area the behaviour of the distribution changes. The small step at the lower end of the graph indicates the aggregation of upper limit sources at roughly the same flux value.

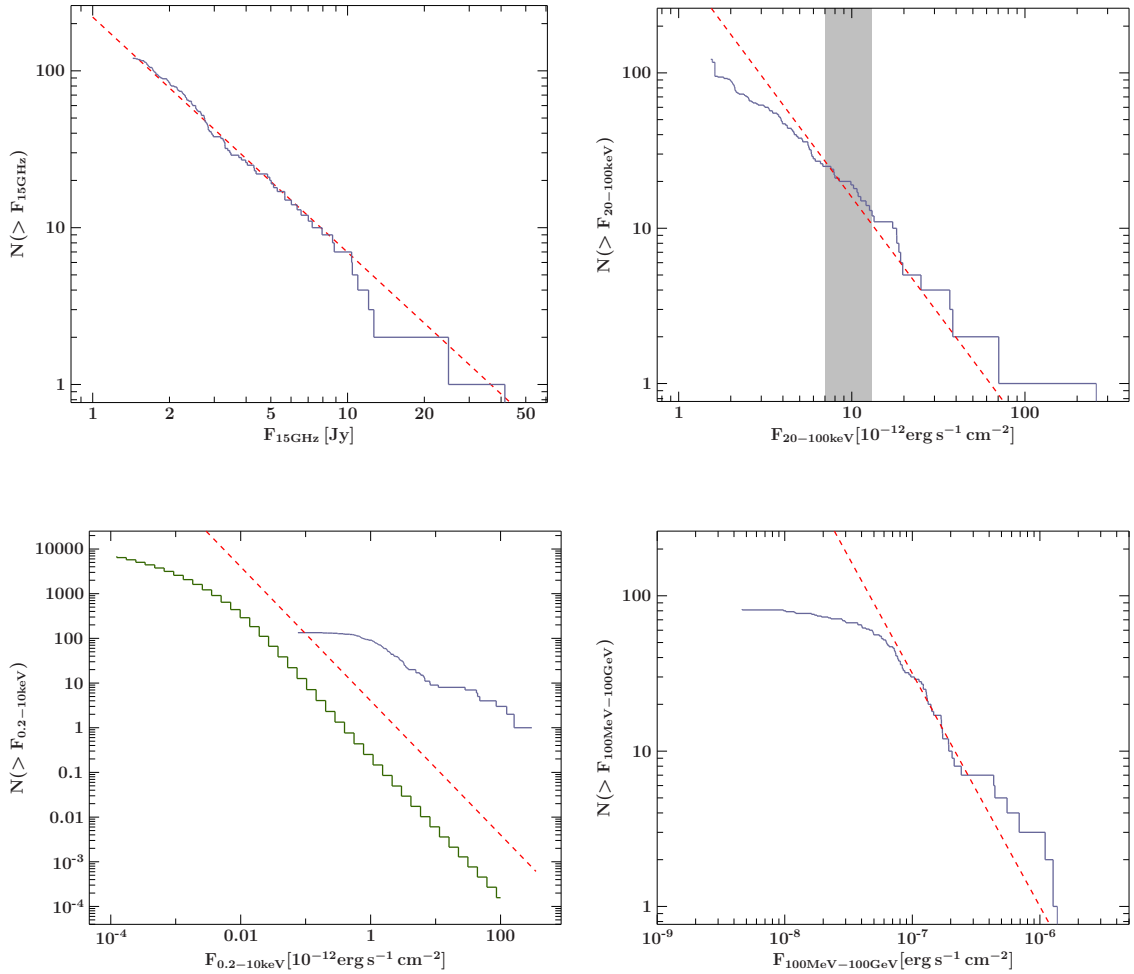


Figure 6.2: Source count distributions of the MOJAVE-1 sample. Top left: 15GHz, top right: 20–100 keV with grey shaded area for fluxes corresponding to BAT SNR $\approx 4.8\sigma$, bottom left: 2–10 keV (blue) and 2–8 keV values after Gilli et al. (2007) (total AGN count, Fig. 10) (green)⁸, bottom right: 0.1–100 GeV. Red dashed lines indicate power-laws with exponent $-3/2$. Normalizations have been chosen for the sake of comparability.

⁸Source count data from Gilli et al. (2007) is actually graphed for $N(> S)$ per square degree. For the qualitative comparison with the 2–10 keV data from *Swift*/XRT (blue line) this has been ignored.

Redshift	Number of Sources	15 GHz	20–100 keV
< 0.2	4	0.45	0.29
< 0.35	13	0.38	0.43
< 1.0	52	0.22	0.31
< 4.0	94	0.19	0.31

Table 6.1: Results of $\langle (F_{\min}/F_i)^{3/2} \rangle$ for a V/V_{\max} test performed for the MOJAVE-1 sample without radio galaxies, unid. sources and upper limits.

The lower left plot shows the distribution for the energy range of 2–10 keV. The blue line represents *Swift*/XRT measurements (Chang, 2010) while the green line is the result of observational data of AGN after Gilli et al. (2007) performed with *Chandra* and *XMM-Newton*. Although the used dataset is actually graphed for $N(> S)$ per square degree, for the sake of comparison this plot is thought to be sufficient. The XRT distribution follows the expected slope of $-3/2$ only for fluxes of about $(1 - 10) \times 10^{-12} \text{ erg s}^{-1} \text{ cm}^{-2}$. Below this region, the curve saturates for faint sources. Above, the distribution shows a significant excess for higher fluxes. The soft X-ray distribution from Gilli et al. (2007) flattens below fluxes of about $0.1 \times 10^{-12} \text{ erg s}^{-1} \text{ cm}^{-2}$ and does not show any excess towards higher fluxes. The slight excess for the XRT curve is likely due to temporarily brighter sources that appear to be extraordinary bright themselves since all XRT observations are single measurements and not averaged over greater ranges of time. A similar source count distribution regarding the pronounced profile of high excess and low saturation of the XRT curve also shows for data of *Fermi*/LAT, in the lower right panel. Because only about two-thirds of the MOJAVE-1 sources were detected in the 1FGL-catalogue, the graph only shows data for 82 AGN. Distributions at low fluxes that are flatter than the power-law with slope $-3/2$, that is in agreement with the rest of the graph, indicates fluxes that are too low for the given number of sources or more importantly fewer detected faint sources than formally expected.

A way of testing if the AGN population in question has a density that depends on distance is the V/V_{\max} test (Krolik, 1999). The quantity that is calculated for the datasets of radio and hard X-ray emission only requires in its simplest form the flux values: $\langle (F_{\min}/F_i)^{3/2} \rangle$ with the flux value for object i and the minimum flux. For an uniform distribution in a Euclidean Universe, a result of 0.5 is expected. Different values indicate a radial gradient of density. Smaller values show a decreasing density distribution with distance while larger ones indicate an increasing density. Results of the test are presented in Table 6.1 for different redshifts, i.e. distances or volumes, respectively. For radio as well as for hard X-ray fluxes the test shows a decreasing density of objects with distance. Furthermore, for sources that are more distant, the density for radio emission becomes much smaller than the expected value of 0.5 while the density for X-ray emission stays about the same, except for the calculation up to $z = 0.35$.

Compared to this sample, other hard X-ray surveys show a more representative view on the AGN and blazar population, respectively. Ajello et al. (2012) compiled a list of 720 objects for the 60-month BAT survey in the energy band of 15–55 keV, with 428 sources classified as AGN. The flux characteristics of this sample are in good agreement with Euclidean geometry. Another sample, including 217 X-ray detected AGN was the *INTEGRAL*/IBIS

7-year All-Sky Hard X-ray Survey by Krivonos et al. (2010) (17–60 keV), also showing an uniform distribution. However, both surveys include relatively close by objects, with a median redshift of AGN of about 0.03 for the BAT data set and a comparatively small value for *INTEGRAL*/IBIS. A sample of objects, that is much more comparable with the MOJAVE-1 sample is the data set of blazars, compiled by Maselli et al. (2010) (previously discussed in Sect. 6.2). The 121 sources are also X-ray selected but feature significantly higher average redshifts, i.e. $\langle z_{\text{BLLac}} \rangle = 0.14$ and $\langle z_{\text{FSRQ}} \rangle = 1.24$ at a detection threshold of $> 3\sigma$, which is very similar to the MOJAVE-1 sample. The corresponding flux distribution is in acceptable agreement with Euclidean geometry.

One of the most important results from comparing the source count graphs for various energy ranges is that the flux-limited MOJAVE-1 sample is complete for the frequency of 15 GHz, but not for soft and hard X-rays as well as for gamma-rays, as clearly indicated by the significant drop of source numbers towards low fluxes. This trend is strongest for the gamma-ray fluxes from LAT, which can be explained by the fact less than all 135 MOJAVE sources were detected with a slight majority of these source distributed towards higher radio fluxes. In other words, assuming an even distribution of X-ray or gamma-ray sources (AGN) in an Euclidean Universe, the MOJAVE-1 sample is not representative and highly biased towards 15 GHz fluxes.

6.3.2 Log(N)-Log(L) Distribution

The source count distribution of fluxes (Log(N)-Log(S)) reveals information about the geometrical distribution of the observed objects that can be compared to cosmological models. Graphing the number of sources against their intrinsic luminosity for various redshift intervals (Log(N)-Log(L)) gives an overview of the evolution of luminosity in AGN sources over time, since luminosity depends on flux and redshift or distance, respectively (Eq. 4.5). However, selection effects for the observed sample have to be taken into account.

Figure 6.3 shows the Log(N)-Log(L) distribution of of hard X-ray luminosities of the MOJAVE-1 sample with three different groups each in bins of redshift z . The limits for the bins in the left panel were determined so that an equal amount of sources fall in each bin. The results are three similar distributions that roughly follow a slope of $-3/2$ (red dashed line) except for lower luminosities. Curves that correspond to a higher redshift than the others have a certain offset towards higher luminosities since less low-luminosity objects are being registered if they are far away. This effect is explained by the Malmquist bias, which favours bright sources at large distances since significantly fainter sources are not even detected (see also Sect. 1.1.4).

The right panel of Fig. 6.3 shows the same plot with different sizes for the redshift bins, that have been determined to the effect that each bin represents the same volume. This is a more suitable and less skewed way of graphing the luminosity. Only sources with redshifts up to $z = 2$ were used, due to the fact that equal volumes up to the maximal redshift of ≈ 3.5 result in very few sources within the last volume interval. Using the same cosmological parameters as in Lister et al. (2009b) and assuming a flat Universe, the volumes have been computed with the help of the online software for cosmological calculations provided by Wright (2006). The resulting distribution for the lowest z bin is similar to the previous plot. The two higher bins exhibit flatter slopes than $-3/2$ except very bright sources.

The most luminous sources in each volume have a more prominent luminosity difference than the faintest objects. Although the logarithmic scaling leads to the same statement for

the first plot (left panel), the trend of the approximation of low luminosities is stronger in this case. The changing and flattening of the slope with redshift, or more distant volume intervals would indicate that less low luminosity objects farther away. The two curves for redshift larger than 1.13 end "earlier", or with less sources than the curve for $z < 1.13$. However this effect, again, is due to the selection effect that prefers sources that are above the flux detection threshold, independently from redshift (Malmquist bias).

Each source count distribution for every z or volume interval features an object with the lowest luminosity in this interval, i.e. the left "end" of the distribution. In an interval closer to the observer, a larger amount of objects is found, indicated by the steeper slope at a certain flux value in a source count plot. In this way, closer distributions of AGN appear to be more of Euclidean nature.

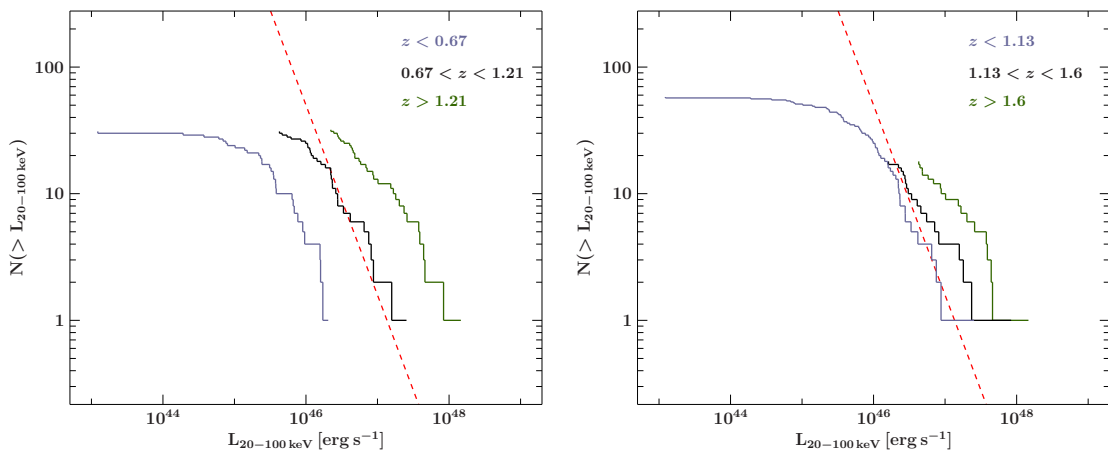


Figure 6.3: Source count distributions for hard X-ray luminosities of the MOJAVE-1 sample: Cumulative number of sources against luminosity, grouped after redshift z for equal number of sources in each bin (left panel) and equal number of sources per bin of volume (right panel).

In the end, the issue of the difference of the source distributions of the same sample for different energy bands is handled by the question of how much the evolution of density and luminosity contribute to the observed emission. For the scope of this thesis, it is thought to be sufficient to characterize the X-ray emission behaviour of the used sample without considering further cosmological influences. To shed light on the characteristics of X-ray-weak radio-loud AGN, that are not completely detected at high redshifts, it is necessary to perform additional and more sensitive measurements in this energy domain.

6.4 Luminosity Dependence of Blazar SEDs

Using spectral data from the soft X-ray (2–10 keV) and gamma-ray regime (0.1–100 GeV) together with BAT multiple broadband SEDs for the MOJAVE-1 sample were created, each for a specific BAT luminosity bin. For the soft X-ray data, spectral information from single observations from *Swift*/XRT (Chang, 2010) and for the gamma-ray data from the 1FGL survey catalogue from *Fermi*/LAT (Abdo et al., 2010b) were used. The sizes of the bins were chosen to the effect that the same amount of sources fall into each of the five bins. Only 82 sources out 135 in the MOJAVE-1 sample were listed in the 1FGL catalogue. When

defining two subsets of objects in the MOVAVE-1 sample, one detected at gamma-rays, and one not detected, the balance of an equal number of sources in every BAT luminosity bin is shifted because the different luminosity classes were detected by *Fermi* not equally well. The following results were determined while excluding upper limit sources.

The plot of hard X-ray against the soft X-ray photon indices of the sample is presented in Fig. 6.4. The upper panel shows the sources of all luminosity classes. Objects with unusual photon indices are additionally labelled. The set of sources concentrates at indices $\Gamma \lesssim 2$, whereas the vast majority is compatible with a BAT index of 2 within their uncertainties, meaning a flat spectrum. This implies that the measured X-ray spectral energy distribution for the most sources lies in the gap between both great emission peaks and at the beginning left side of the IC peak. The lower panel shows sources only from the highest luminosity bin ($L_{\text{BAT}} > 5.5 \cdot 10^{46} \text{ erg s}^{-1}$). Evidently, sources that are the brightest at hard X-rays also feature lower photon indices, i.e. a steeper energy distribution. This tendency is followed by the objects from the second-brightest luminosity bin. Detections in the 1FGL catalogue are indicated by black crosses.

Excluding upper limits and radio galaxies, the SEDs for both *Fermi*-detected (1FGL) and non-detected sources are plotted in Fig. 6.5 using the averaged photon index in each luminosity bin to indicate the spectral shape of the energy distribution. The number of all 69 1FGL-sources is distributed as (from faintest bin to brightest): 13, 11, 18, 11, 16. The 29 non-detected sources have the distribution: 7, 5, 2, 6, 9. The criterion of how many sources contribute to the average flux in a bin is admittedly rather arbitrary. Depending on the exact binning, the offsets of the different graphed slopes vary strongly. In general though, non-detected source bins seem to feature lower averaged fluxes than the corresponding detected ones. For the highest luminosity class this may be explained by the redshift distribution of this source group, which possesses on average a significantly higher redshift than the corresponding luminosity class of detected sources (see Fig. 6.6).

In both graphs in Fig. 6.5 the slopes of both X-ray regions increase with higher (brighter) BAT luminosity bin. In the first approximation no clear change of the slope with the luminosity bin can be recognized for the spectral region of LAT. To make a more founded statement of the suggested relation of spectral shape regarding hard X-ray luminosity, a partial correlation analysis has been conducted for the slopes of each source including all upper limits. The partial Kendall's Tau (see Sect. 4.3.2) has been calculated for the slopes (photon indices) of each two spectral regions with the corresponding BAT luminosity as the third parameter the slopes depend upon. A significant correlation of BAT and LAT slopes has been found with $\tau/\sigma = -2.47$, using data of 77 sources. The negative value indicates an anti-correlation, i.e. the steeper one slope is, the flatter is the other one and vice versa. Since BAT measures AGN spectra at the left side of the IC peak and Fermi/LAT on the right side, the determined (anti)correlation implies a shift of the emission peak towards lower frequencies for higher luminosities.

No significant correlations for the photon indices of XRT and BAT for 1FGL-detected and non-detected sources could be found with $\tau/\sigma = 0.28$ and $\tau/\sigma = 0.59$, respectively. However, this result might likely be misleading since the BAT photon indices were calculated using accumulated data over 70 months, while the values XRT are based on single measurements that can be subjected to variability. Another issue is the position of the soft X-ray domain for this sample itself, which is located at even lower energies than the BAT region. This means that XRT might measure contributions of the synchrotron and IC peak depending

on the specific object and variability state. At this point a correlation between both X-ray domains is difficult to estimate and cannot be ruled out completely.

Figure 6.6 shows the redshift distribution for the MOJAVE-1 sample with 1FGL-detected (upper panel) and non-detected sources (lower panel). Objects with X-ray luminosities in the highest BAT bin are marked additionally. The detected sources form a wide peaked distribution around $z \approx 1$, while non-detections have an overall flatter and less pronounced distribution. The relative amount of brightest BAT sources is approximately equal in both groups. However, the detected group does not exhibit redshifts greater than about 2.2, whereas the non-detected group features six quasars above this limit, three of them in the brightest X-ray category. Some of the sources in this luminosity group have not been detected in the 1FGL catalogue. These objects all are distant sources ($z \gtrsim 1.6$) and have on average a significantly higher redshift than the X-ray-brightest sources that have been detected by *Fermi*. This result suggests a relation between the ability to detect a source in the gamma-ray regime by *Fermi* (at least up to a certain significance) and the distance (redshift) while hard X-ray emission peaks in these cases.

This luminosity dependence of spectral slopes for a sample of blazars is known to be described by the so-called blazar sequence (see also Sect. 2.2), first characterized by Fossati et al. (1998). A recent study, using observations with *Fermi*/LAT and *Swift*/BAT was presented by Sambruna et al. (2010), who worked with a gamma-ray and hard X-ray selected sample of blazars. The corresponding luminosity classes were binned regarding hard X-ray emission. They found a luminosity dependence of the spectral slopes at both energies, supporting the blazar sequence, which was originally based upon radio samples and radio luminosities. The used blazar sample was composed of 12 FSRQs and 10 BL Lacs, all detected over a threshold of 3σ . FSRQs, which are generally more luminous than BL Lacs were found to have hard continua at X-rays as well as soft continua at gamma-rays (photon indices $\Gamma_X \lesssim 2$ and $\Gamma_\gamma \gtrsim 2.4$). BL Lacs follow this trend, but with less softer gamma continua ($\Gamma_\gamma \gtrsim 2$). A third group is characterized by the opposite behaviour regarding photon indices, called high-energy-peaked BL Lacs (HBLs). The X-ray and gamma-ray characteristics of the MOJAVE-1 blazars are far less pronounced compared to the data set from Sambruna et al. (2010). Here, the average slopes of BL Lacs at gamma-rays are only slightly harder than the group of quasars ($\Gamma_{\gamma, \text{BLLac}} \approx 2.3$ and $\Gamma_{\gamma, \text{quasar}} \approx 2.5$). Furthermore, no sources with the distinct properties of HBLs are found. Despite of the less distinct population in terms of spectral shape, the overall behaviour, described by the blazar sequence can be confirmed for this set of radio-selected blazars.

As mentioned before, because of merely single XRT measurements of the MOJAVE-1 sample, possible correlations of photon indices to BAT or LAT cannot clearly be derived. With the help of averaged slopes for XRT observations it could be determined, if the soft and hard X-ray photon indices of all non-*Fermi* sources also indicate a behaviour described by the blazar sequence. If this would be the case, one would expect that the IC emission peaks are shifted to relatively low energies, since they are apparently not visible by *Fermi* in the corresponding gamma-ray band. Following the predictions of the blazar sequence, the corresponding luminosity of these sources should be larger than for the *Fermi*-detected group. This constitutes an approach for the estimation if the blazar sequence in its simplest form can explain the missing *Fermi* detections of about a third of the sources in the MOJAVE sample.

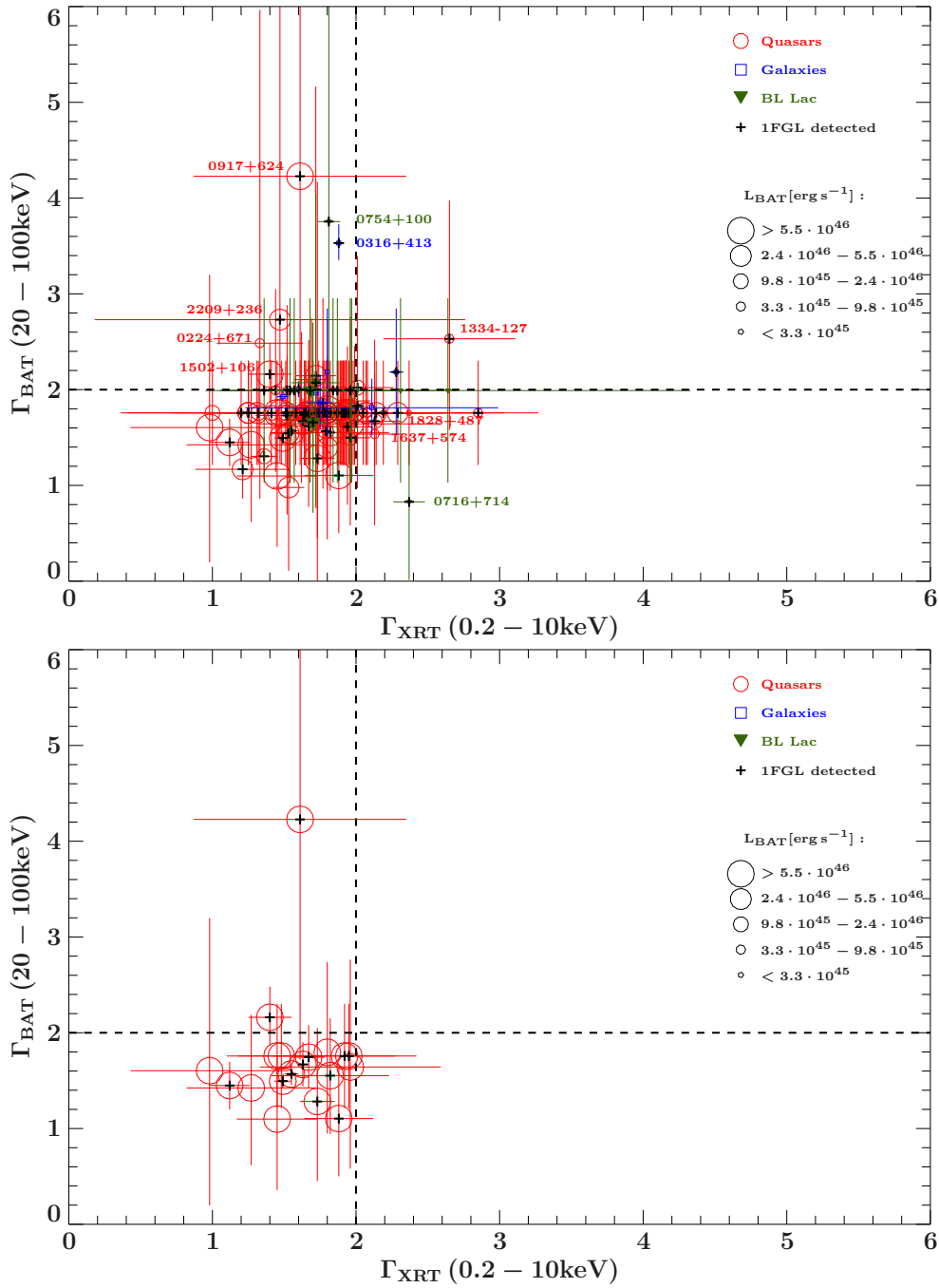


Figure 6.4: Relation of photon indices of BAT (20–100 keV) and XRT (2–10 keV) for the entire MOJAVE-1 sample (upper panel) and only the highest BAT luminosity bin (lower panel). Dashed lines indicate $\Gamma = 2$.

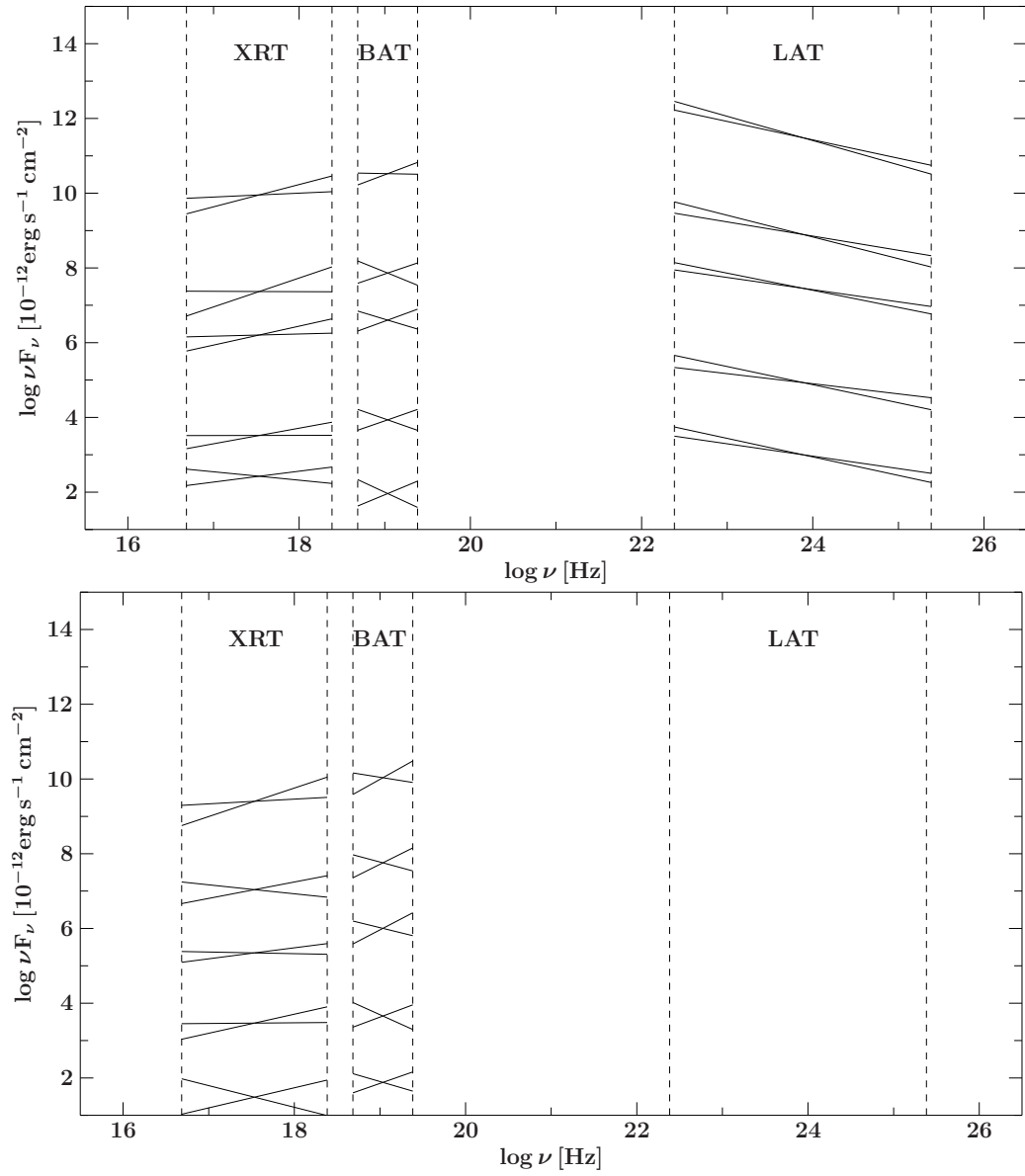


Figure 6.5: Spectral energy distribution of the MOJAVE-1 sample excluding upper limit sources and radio galaxies. To distinguish each of five distributions (BAT luminosity bins), an artificial offset has been added respectively. The upper panel shows all 69 1FGL detected sources, while the lower panel displays all 29 non-detected ones. Spectral slopes are averaged values.

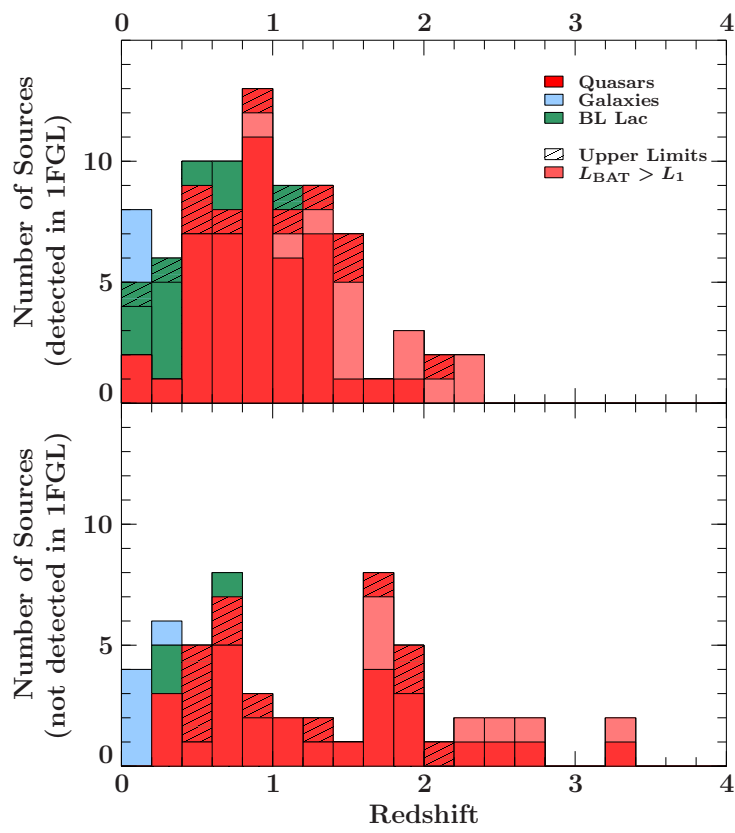


Figure 6.6: Distribution of MOJAVE-1 redshift values for 1FGL detected (upper panel) and non-detected sources (lower panel). The lower limit for the highest BAT luminosity bin is $L_1 = 5.5 \cdot 10^{46} \text{ erg s}^{-1}$. Objects above L_1 are exclusively quasars.

7 Conclusion and Outlook

THE working basis in this thesis is a complete sample of 135 radio-selected AGN, that is composed mostly out of blazars and regularly monitored by the MOJAVE program using VLBI techniques. With the analysis of X-ray spectra gathered by *Swift*/BAT, hard X-ray characteristics are available for the first time for such a large and well defined blazar sample. In addition to the finding, that the majority of the AGN sample can be classified as hard X-ray emitters, the properties of flux and luminosity have been addressed. The following points represent the main aspects of further studies in this work regarding correlation studies to other energy bands, basic statistical issues of the collected X-ray data set, as well as the relevance for current research concerning blazar luminosities:

- A significant part of the sample, 29 out of 135 sources, is characterized as upper limits in flux and luminosity space. However, this number is a rather conservative estimation. Depending on the exact criteria for the definition of upper limit sources, different values for the fluxes of upper limits emerge, which can be significantly lower than sources of similar radio flux, forming a possibly separate group of hard X-ray weak blazars. This case has to be studied further under involvement of more sensitive data or by theoretical hard X-ray emission models for jets.
- The fluxes in the hard X-ray regime are only mildly correlated to VLBI radio fluxes, whereas significant correlations of the luminosities have been determined for the entire sample, as well for the subsample of quasars. It cannot be excluded that the groups of radio galaxies and BL Lacs also show X-ray-radio correlation. For this to prove, larger samples of the corresponding AGN types are required. A consequential approach for example would be the extension of the number of objects by involving the source catalogue of TANAMI (Ojha et al., 2010), an equivalent AGN monitoring program on the southern hemisphere.
- The source count distributions at different wavelengths of the MOJAVE-1 sample suggest considerable selection effects regarding the radio measurements. To what extent the evolution of density and luminosity in the energy ranges of X-rays and gamma-rays influences the observed distributions is still open to debate. To address the issue of the actual density distribution at hard X-rays it is necessary to perform further and more sensitive observations of blazars spread over large scales of distance.
- By assembling broadband SEDs with observational data from *Swift*/XRT, BAT and *Fermi*/LAT, the spectral behaviour described by the blazar sequence could be verified on a large sample of radio-selected blazars. However, it is still to be discussed if the non-detection of MOJAVE sources by *Fermi* can also be explained by a shift of the IC emission peak as the model of the blazar sequence in its simplest form would suggest. Taking into account long-term surveys at different wavelengths, such as soft X-rays (XRT), of the very same subsample could help to clarify this assumption.

Many of the raised issues from the results of this work establish starting points for future research in the fields of multi-wavelength astronomy and especially the source class of blazars. With the help of high-quality X-ray measurements, further interesting and important results for understanding emission processes in AGN and the unification of AGN classes can be expected. The recently launched mission *NuSTAR* (Harrison et al., 2010) would prove very effective for these purposes, because of its vastly improved sensitivity at hard X-rays compared to previous and other concurrent missions. At this point, it is highly suggested to use this new instrument for the multi-wavelength research issues that lie within the list of the MOJAVE-1 sources, especially with the more peculiar ones like the highly variable BL Lac object 0716+714, or the group of very X-ray faint AGN.

A Graphs: Radio and Hard X-ray Relations

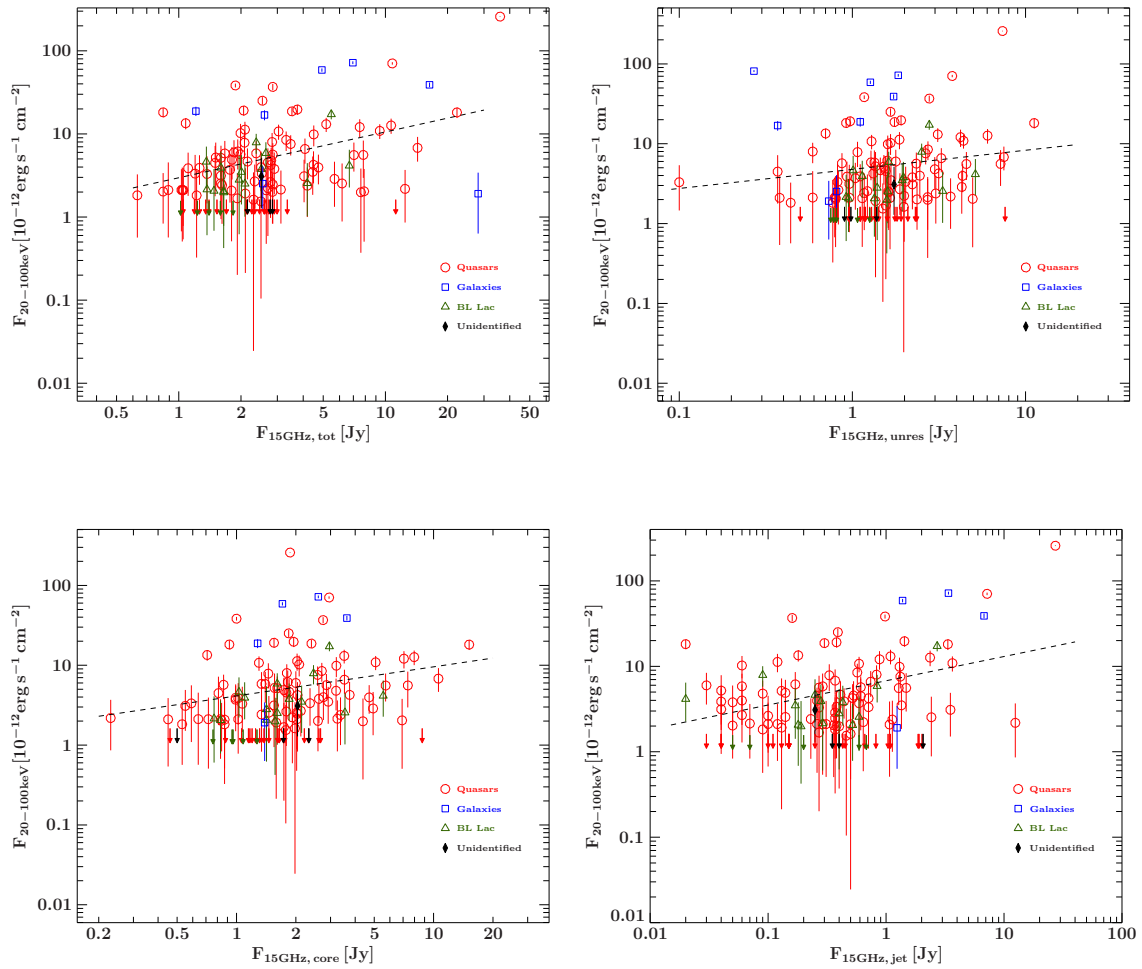


Figure A.1: Relation of hard X-ray fluxes to the following radio measurements of the MOJAVE-1 sample: total (top left), unresolved (top right), core (bottom left), and jet (bottom right).

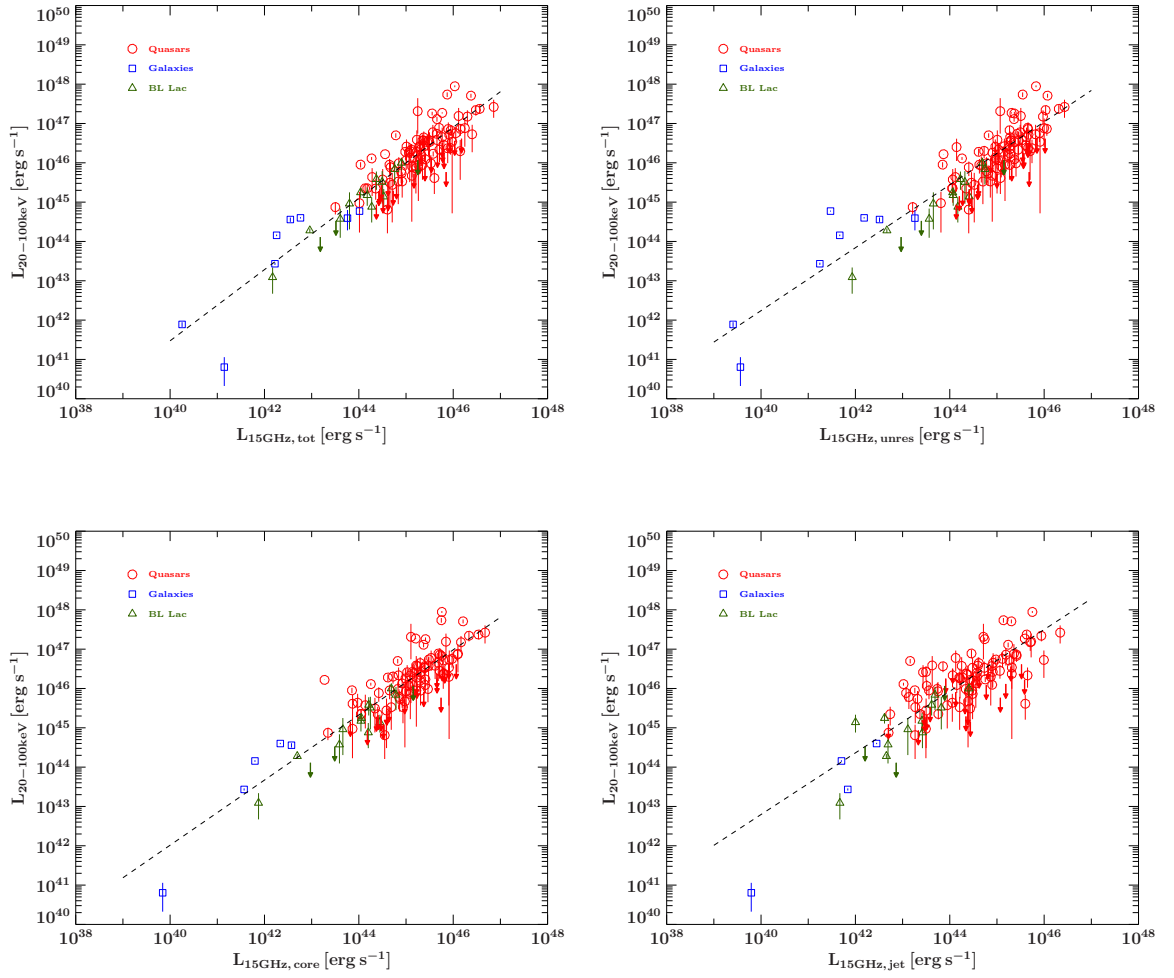


Figure A.2: Relation of hard X-ray luminosities to the following radio measurements of the MOJAVE-1 sample: total (top left), unresolved (top right), core (bottom left), and jet (bottom right).

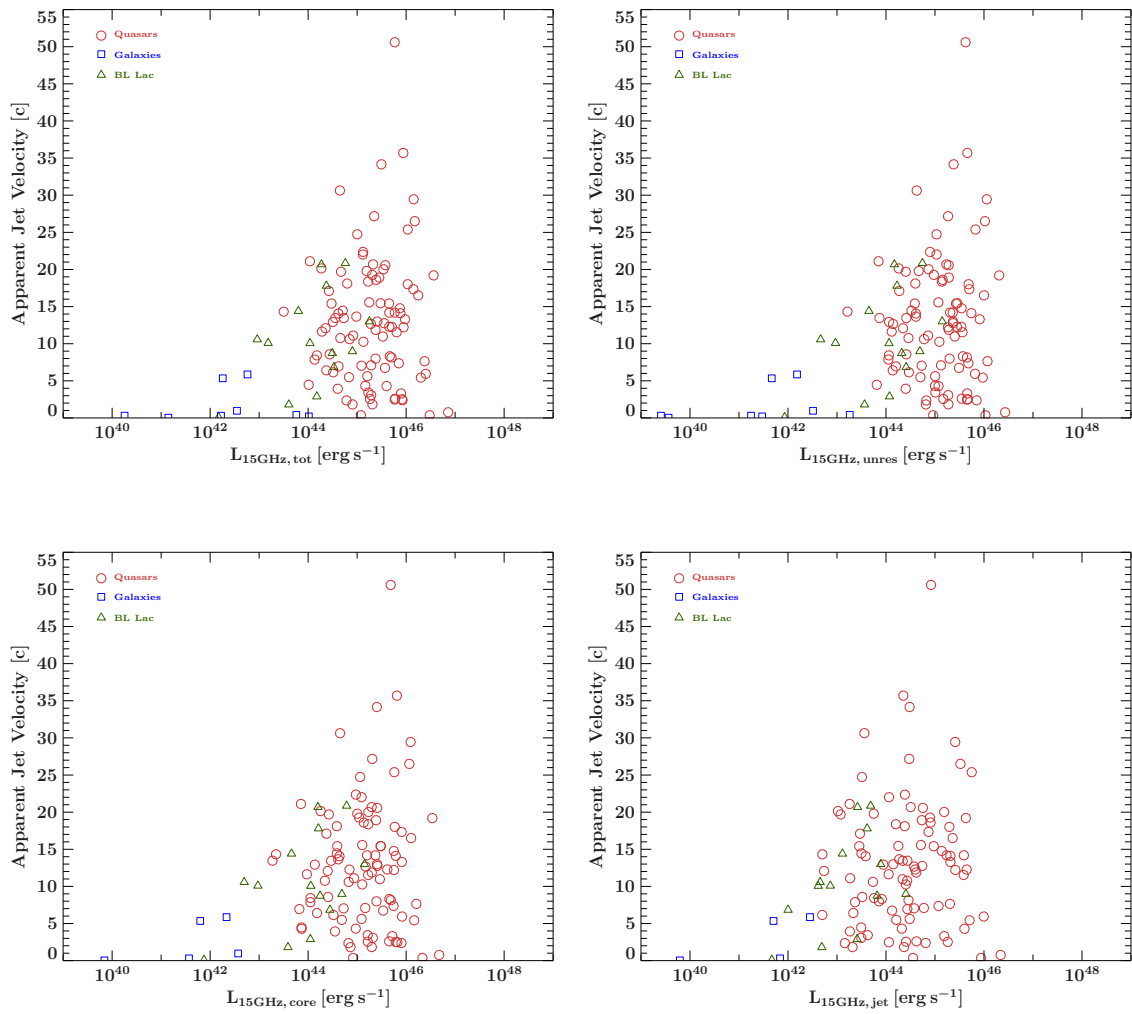


Figure A.3: Apparent jet velocity in units of c against radio luminosity measurements of the MOJAVE-1 sample: total (top left), unresolved (top right), core (bottom left), and jet (bottom right).

B Hard X-ray Data for the MOJAVE-1 Sample

Table B.1: MOJAVE-1 sample with calculated photon indices, fluxes and luminosities in the range of 20–100 keV.

Name ^a	Common Name	SNR ^b	Γ^c	$F_{20-100\text{keV}}^d$ [$10^{-12} \frac{\text{erg}}{\text{cm}^2}$]	$L_{20-100\text{keV}}$ [erg s^{-1}]	Type ^e	z	X-ray det. ^f	γ -ray det. ^g
0003-066	NRAO 005	2.13		$3.78_{-0.43}^{+0.54}$ *	$(1.50_{-0.19}^{+0.20}) \times 10^{45}$	B	0.3467		
0007+106	III Zw 2	13.12	$1.86_{-0.27}^{+0.29}$	$18.81_{-2.40}^{+2.40}$	$(3.61_{-0.46}^{+0.46}) \times 10^{44}$	G	0.0893	1	
0016+731		3.62	$1.64_{-1.06}^{+1.12}$	$3.87_{-2.07}^{+2.09}$	$(5.97_{-3.20}^{+3.23}) \times 10^{46}$	Q	1.781		
0048-097	PKS 0048-09	2.25		$2.52_{-0.29}^{+0.36}$ *		B			3
0059+581	TXS 0059+581	1.35		$2.14_{-0.12}^{+0.19}$ *	$(3.35_{-0.25}^{+0.24}) \times 10^{45}$	Q	0.644		3
0106+013	4C +01.02	1.64		$1.18_{-0.07}^{+0.10}$ *	$(2.99_{-0.22}^{+0.22}) \times 10^{46}$	Q	2.099		3
0109+224	S2 0109+22	0.93		$0.74_{-0.08}^{+0.10}$ *	$(1.57_{-0.20}^{+0.21}) \times 10^{44}$	B	0.265		3
0119+115	PKS 0119+11	-0.22		0.04^{\dagger} *	4.76×10^{43}	Q	0.57		
0133+476	DA 55	2.52		$3.96_{-0.23}^{+0.35}$ *	$(1.23_{-0.09}^{+0.09}) \times 10^{46}$	Q	0.859		3
0202+149	4C +15.05	0.29		$0.57_{-0.03}^{+0.05}$ *	$(3.03_{-0.22}^{+0.22}) \times 10^{44}$	Q	0.405		3
0202+319	B2 0202+31	0.50		$0.78_{-0.04}^{+0.07}$ *	$(8.63_{-0.64}^{+0.63}) \times 10^{45}$	Q	1.466		3
0212+735	S5 0212+73	13.12	$1.45_{-0.25}^{+0.25}$	$18.69_{-2.14}^{+2.14}$	$(5.10_{-0.58}^{+0.58}) \times 10^{47}$	Q	1.466	1, 2	3
0215+015	OD 026	1.54		$2.11_{-0.12}^{+0.19}$ *	$(3.36_{-0.25}^{+0.24}) \times 10^{46}$	Q	1.715		3
0224+671	4C +67.05	3.04	$2.49_{-1.62}^{+3.48}$	$3.33_{-2.24}^{+2.27}$	$(4.34_{-2.92}^{+2.96}) \times 10^{45}$	Q	0.523		
0234+285	4C +28.07	2.31		$3.10_{-0.18}^{0.27}$ *	$(2.16_{-0.16}^{+0.16}) \times 10^{46}$	Q	1.206		3
0235+164	AO 0235+164	3.05		$5.20_{-3.12}^{+2.68}$	$(2.58_{-1.55}^{+1.33}) \times 10^{46}$	Q	0.94		3
0238-084	NGC 1052	12.47	$1.81_{-0.29}^{+0.30}$	$16.90_{-2.32}^{+2.32}$	$(7.76_{-1.07}^{+1.07}) \times 10^{41}$	G	0.005037	1	
0300+470	4C +47.08	3.31	$1.80_{-1.22}^{+1.30}$	$4.63_{-2.41}^{+2.42}$		B			3
0316+413	3C 84	50.91	$3.53_{-0.18}^{+0.20}$	$38.97_{-2.48}^{+2.50}$	$(2.72_{-0.17}^{+0.17}) \times 10^{43}$	G	0.0176	1, 2*	3
0333+321	NRAO 140	13.93	$1.67_{-0.23}^{+0.23}$	$25.09_{-2.61}^{+2.61}$	$(1.79_{-0.19}^{+0.19}) \times 10^{47}$	Q	1.259	1	3
0336-019	CTA 26	1.03		$1.54_{-0.09}^{+0.14}$ *	$(4.69_{-0.35}^{+0.34}) \times 10^{45}$	Q	0.852		3
0403-132	PKS 0403-13	5.23	$1.99_{-0.85}^{+1.06}$	$5.84_{-2.35}^{+2.35}$	$(7.66_{-3.08}^{+3.09}) \times 10^{45}$	Q	0.571	1	3
0415+379	3C 111	40.74	$2.00_{-0.08}^{+0.08}$	$71.91_{-2.77}^{+2.77}$	$(3.99_{-0.15}^{+0.15}) \times 10^{44}$	G	0.0491	1, 2	3
0420-014	PKS 0420-01	1.50		$1.51_{-0.09}^{+0.13}$ *	$(5.44_{-0.40}^{+0.39}) \times 10^{45}$	Q	0.9161		3

continued.

Name ^a	Common Name	SNR ^b	Γ^c	$F_{20-100\text{ keV}}^d$ [$10^{-12} \frac{\text{erg}}{\text{cm}^2 \text{ s}}$]	$L_{20-100\text{ keV}}$ [erg s^{-1}]	Type ^e	z	X-ray det. ^f	γ -ray det. ^g
0422+004	PKS 0422+00	-0.06		$1.98_{-0.23}^{+0.28*}$		B			3
0430+052	3C 120	36.09	$1.97_{-0.10}^{+0.10}$	$58.79_{-2.72}^{+2.72}$	$(1.43_{-0.07}^{+0.07}) \times 10^{44}$	G	0.033	1	
0446+112	PKS 0446+11	1.41		$3.09_{-0.18}^{+0.27*}$		U			3
0458-020	S3 0458-02	1.60		$2.47_{-0.14}^{+0.22*}$	$(7.62_{-0.56}^{+0.55}) \times 10^{46}$	Q	2.286		3
0528+134	PKS 0528+134	4.93	$1.55_{-0.61}^{+0.60}$	$12.08_{-2.96}^{+2.95}$	$(2.36_{-0.58}^{+0.58}) \times 10^{47}$	Q	2.07	1, 2	3
0529+075	OG 050	1.29		$3.29_{-0.19}^{+0.29*}$	$(2.51_{-0.19}^{+0.18}) \times 10^{46}$	Q	1.254		3
0529+483	TXS 0529+483	0.95		$2.11_{-0.12}^{+0.19*}$	$(1.34_{-0.10}^{+0.10}) \times 10^{46}$	Q	1.162		3
0552+398	DA 193	4.87	$1.42_{-0.81}^{+0.76}$	$9.87_{-2.78}^{+2.77}$	$(2.19_{-0.62}^{+0.61}) \times 10^{47}$	Q	2.363		
0605-085	OC -010	1.31		$2.64_{-0.15}^{+0.23*}$	$(8.47_{-0.63}^{+0.61}) \times 10^{45}$	Q	0.872		3
0607-157	PKS 0607-15	0.52		$2.04_{-0.12}^{+0.18*}$	$(6.48_{-0.48}^{+0.47}) \times 10^{44}$	Q	0.3226		
0642+449	OH 471	2.75		$3.49_{-0.20}^{+0.31*}$	$(2.63_{-0.19}^{+0.19}) \times 10^{47}$	Q	3.396		
0648-165	PKS 0648-16	0.30		0.04†*		U		1	3
0716+714	S5 0716+71	4.68	$0.83_{-0.81}^{+0.65}$	$7.90_{-2.13}^{+2.13}$	$(1.76_{-0.48}^{+0.47}) \times 10^{45}$	B	0.31		3
0727-115	PKS 0727-11	2.97		$4.25_{-0.24}^{+0.37*}$	$(5.67_{-0.42}^{+0.41}) \times 10^{46}$	Q	1.591		3
0730+504	TXS 0730+504	-0.14		$1.17_{-0.07}^{+0.10†*}$	$(2.39_{-0.18}^{+0.17}) \times 10^{45}$	Q	0.72		
0735+178	OI 158	-0.75		0.04†*		B			3
0736+017	OI 061	4.13	$1.61_{-0.81}^{+0.84}$	$7.85_{-2.73}^{+2.72}$	$(7.46_{-2.59}^{+2.59}) \times 10^{44}$	Q	0.1894		3
0738+313	OI 363	1.20		$2.08_{-0.12}^{+0.18*}$	$(3.11_{-0.23}^{+0.23}) \times 10^{45}$	Q	0.631		
0742+103		3.00	$1.60_{-1.41}^{+1.59}$	$4.48_{-2.70}^{+2.71}$	$(1.55_{-0.93}^{+0.94}) \times 10^{47}$	Q	2.624		
0748+126	OI 280	2.93		$5.63_{-0.32}^{+0.50*}$	$(1.90_{-0.14}^{+0.14}) \times 10^{46}$	Q	0.889		3
0754+100	PKS 0754+100	3.41	$3.75_{-1.89}^{+5.25}$	$2.81_{-2.19}^{+2.64}$	$(9.14_{-7.12}^{+8.59}) \times 10^{44}$	B	0.266		3
0804+499		1.38		$2.11_{-0.12}^{+0.19*}$	$(2.21_{-0.16}^{+0.16}) \times 10^{46}$	Q	1.436		
0805-077	PKS 0805-07	1.82		$2.41_{-0.14}^{+0.21*}$	$(4.50_{-0.33}^{+0.33}) \times 10^{46}$	Q	1.837		3
0808+019	OJ 014	-0.17		0.04†*	2.99×10^{44}	B	1.148		3
0814+425	OJ 425	-0.38		0.04†*		B			3

continued.

Name ^a	Common Name	SNR ^b	Γ^c	$F_{20-100\text{keV}}^d$ [$10^{-12} \frac{\text{erg}}{\text{cm}^2}$]	$L_{20-100\text{keV}}$ [erg s^{-1}]	Type ^e	z	X-ray det. ^f	γ -ray det. ^g
0823+033	PKS 0823+033	2.40		$3.91^{+0.55*}_{-0.45}$	$(3.82^{+0.50}_{-0.48}) \times 10^{45}$	B	0.506		3
0827+243	OJ 248	3.45	$1.62^{+0.90}_{-0.84}$	$6.15^{+2.42}_{-2.42}$	$(2.16^{+0.85}_{-0.85}) \times 10^{46}$	Q	0.942		3
0829+046	OJ 049	0.79		$0.64^{+0.091*}_{-0.07}$	$(5.27^{+0.69}_{-0.66}) \times 10^{43}$	B	0.174		3
0836+710	4C +71.07	30.06	$1.57^{+0.12}_{-0.12}$	$38.28^{+2.04}_{-2.04}$	$(8.84^{+0.47}_{-0.47}) \times 10^{47}$	Q	2.218	1	3
0838+133	3C 207	0.86		$2.10^{+0.18*}_{-0.12}$	$(3.75^{+0.27}_{-0.28}) \times 10^{45}$	Q	0.681		3
0851+202	OJ 287	1.89		$2.55^{+0.36*}_{-0.29}$	$(7.58^{+0.99}_{-0.95}) \times 10^{44}$	B	0.306		3
0906+015	4C +01.24	2.93		$3.35^{+0.29*}_{-0.19}$	$(1.58^{+0.11}_{-0.12}) \times 10^{46}$	Q	1.0256		3
0917+624	OK 630	3.11	$4.23^{+4.77}_{-2.51}$	$2.12^{+2.42}_{-1.55}$	$(2.06^{+2.35}_{-1.50}) \times 10^{47}$	Q	1.446		3
0923+392	4C +39.25	2.08		$2.18^{+0.19*}_{-0.12}$	$(4.09^{+0.30}_{-0.30}) \times 10^{45}$	Q	0.695		
0945+408	4C +40.24	3.24	$1.69^{+2.48}_{-1.85}$	$3.70^{+2.07}_{-2.21}$	$(2.64^{+1.48}_{-1.58}) \times 10^{46}$	Q	1.249		
0955+476	OK 492	0.97		$1.01^{+0.091*}_{-0.06}$	$(2.00^{+0.14}_{-0.15}) \times 10^{46}$	Q	1.882		
1036+054	PKS 1036+054	-0.32		$0.04^{\dagger*}$	3.08×10^{43}	Q	0.473		
1038+064	4C +06.41	3.49	$1.73^{+1.15}_{-1.03}$	$5.82^{+2.41}_{-2.44}$	$(4.42^{+1.83}_{-1.85}) \times 10^{46}$	Q	1.265		3
1045-188		1.15		$0.38^{+0.031*}_{-0.02}$	$(4.96^{+0.36}_{-0.37}) \times 10^{44}$	Q	0.595		
1055+018	4C +01.28	2.46		$2.87^{+0.25*}_{-0.16}$	$(9.71^{+0.70}_{-0.72}) \times 10^{45}$	Q	0.888		3
1124-186	PKS 1124-186	-0.13		$0.37^{+0.031*}_{-0.02}$	$(1.86^{+0.14}_{-0.14}) \times 10^{45}$	Q	1.048		3
1127-145	PKS 1127-14	12.13	$1.75^{+0.34}_{-0.32}$	$19.68^{+2.75}_{-2.76}$	$(1.30^{+0.18}_{-0.18}) \times 10^{47}$	Q	1.184	1	3
1150+812		0.13		$0.25^{+0.021*}_{-0.01}$	$(1.87^{+0.14}_{-0.14}) \times 10^{45}$	Q	1.25		
1156+295	4C +29.45	4.43	$2.02^{+1.37}_{-1.05}$	$4.79^{+2.02}_{-2.07}$	$(1.16^{+0.49}_{-0.50}) \times 10^{46}$	Q	0.7246		3
1213-172	PKS 1213-17	0.30		$0.33^{+0.031*}_{-0.02}$		U			
1219+044	4C +04.42	11.13	$1.17^{+0.29}_{-0.30}$	$18.19^{+2.34}_{-2.35}$	$(4.99^{+0.64}_{-0.64}) \times 10^{46}$	Q	0.965	1	3
1222+216	4C +21.35	10.65	$1.99^{+0.36}_{-0.33}$	$13.44^{+2.07}_{-2.07}$	$(8.99^{+1.38}_{-1.38}) \times 10^{45}$	Q	0.434	1	3
1226+023	3C 273	177.06	$1.74^{+0.02}_{-0.02}$	$257.94^{+2.43}_{-2.38}$	$(1.66^{+0.02}_{-0.02}) \times 10^{46}$	Q	0.1583	1	3
1228+126	M87	2.82		$1.91^{+0.25*}_{-0.11}$	$(6.38^{+0.61}_{-0.56}) \times 10^{40}$	G	0.00436		3
1253-055	3C 279	10.93	$1.56^{+0.33}_{-0.33}$	$18.14^{+2.61}_{-2.61}$	$(1.70^{+0.24}_{-0.24}) \times 10^{46}$	Q	0.536	1	3

continued.

Name ^a	Common Name	SNR ^b	Γ^c	$F_{20-100\text{keV}}^d$ [$10^{-12} \frac{\text{erg}}{\text{cm}^2 \text{s}}$]	$L_{20-100\text{keV}}$ [erg s^{-1}]	Type ^e	z	X-ray det. ^f	γ -ray det. ^g
1308+326	OP 313	2.19		$2.01^{+0.18*}_{-0.11}$	$(8.88^{+0.64}_{-0.66}) \times 10^{45}$	Q	0.9973		3
1324+224	B2 1324+22	0.99		$1.83^{+0.16*}_{-0.10}$	$(1.80^{+0.13}_{-0.13}) \times 10^{46}$	Q	1.4		3
1334-127	PKS 1335-127	4.41	$2.53^{+1.44}_{-0.95}$	$5.59^{+2.73}_{-2.63}$	$(8.03^{+3.92}_{-3.78}) \times 10^{45}$	Q	0.539	1	3
1413+135	PKS B1413+135	1.50		$2.06^{+0.29*}_{-0.24}$	$(3.74^{+0.49}_{-0.47}) \times 10^{44}$	B	0.247		
1417+385	B3 1417+385	0.77		$2.03^{+0.18*}_{-0.12}$	$(3.75^{+0.27}_{-0.28}) \times 10^{46}$	Q	1.831		
1458+718	3C 309.1	4.53	$1.77^{+0.83}_{-0.74}$	$5.69^{+1.93}_{-1.93}$	$(2.01^{+0.68}_{-0.68}) \times 10^{46}$	Q	0.904	1	
1502+106	OR 103	13.75	$2.16^{+0.32}_{-0.29}$	$19.13^{+2.55}_{-2.55}$	$(5.44^{+0.73}_{-0.73}) \times 10^{47}$	Q	1.8385		3
1504-166		-0.47		$0.80^{+0.07\dagger*}_{-0.05}$	$(2.59^{+0.19}_{-0.19}) \times 10^{45}$	Q	0.876		
1510-089	PKS 1510-08	14.93	$1.30^{+0.20}_{-0.21}$	$36.80^{+3.18}_{-3.18}$	$(1.29^{+0.11}_{-0.11}) \times 10^{46}$	Q	0.36	1	3
1538+149	4C +14.60	1.40		$2.15^{+0.30*}_{-0.25}$	$(3.24^{+0.43}_{-0.41}) \times 10^{45}$	B	0.605		
1546+027	PKS 1546+027	1.43		$3.98^{+0.35*}_{-0.23}$	$(2.22^{+0.16}_{-0.16}) \times 10^{45}$	Q	0.414		3
1548+056	4C +05.64	1.58		$1.35^{+0.12\dagger*}_{-0.08}$	$(1.39^{+0.10}_{-0.10}) \times 10^{46}$	Q	1.417		3
1606+106	4C +10.45	2.27		$4.65^{+0.41*}_{-0.27}$	$(3.36^{+0.24}_{-0.25}) \times 10^{46}$	Q	1.226		3
1611+343	DA 406	2.22		$2.38^{+0.21*}_{-0.14}$	$(2.34^{+0.17}_{-0.17}) \times 10^{46}$	Q	1.4		3
1633+382	4C +38.41	3.10	$1.28^{+0.77}_{-0.83}$	$6.59^{+2.20}_{-2.20}$	$(7.30^{+2.44}_{-2.44}) \times 10^{46}$	Q	1.813		3
1637+574	OS 562	3.81	$1.54^{+0.99}_{-0.95}$	$4.89^{+2.06}_{-2.06}$	$(9.75^{+4.11}_{-4.11}) \times 10^{45}$	Q	0.751		
1638+398	NRAO 512	1.96		$2.55^{+0.22*}_{-0.15}$	$(3.79^{+0.27}_{-0.28}) \times 10^{46}$	Q	1.666		
1641+399	3C 345	7.06	$1.50^{+0.47}_{-0.47}$	$10.88^{+2.19}_{-2.19}$	$(1.24^{+0.25}_{-0.25}) \times 10^{46}$	Q	0.593	1	3
1655+077	PKS 1655+077	0.74		$1.92^{+0.17*}_{-0.11}$	$(2.76^{+0.20}_{-0.20}) \times 10^{45}$	Q	0.621		
1726+455	S4 1726+45	1.40		$2.69^{+0.24*}_{-0.15}$	$(5.43^{+0.39}_{-0.40}) \times 10^{45}$	Q	0.717		3
1730-130	NRAO 530	2.46		$6.80^{+0.60*}_{-0.39}$	$(2.37^{+0.17}_{-0.18}) \times 10^{46}$	Q	0.902		3
1739+522	4C +51.37	2.85		$3.90^{+0.34*}_{-0.22}$	$(3.72^{+0.27}_{-0.28}) \times 10^{46}$	Q	1.379		3
1741-038	PKS 1741-03	1.46		$5.57^{+0.49*}_{-0.32}$	$(2.81^{+0.20}_{-0.21}) \times 10^{46}$	Q	1.054	2	3
1749+096	4C +09.57	2.50		$4.14^{+0.59*}_{-0.48}$	$(1.38^{+0.18}_{-0.17}) \times 10^{45}$	B	0.322		3
1751+288	B2 1751+28	3.84	$1.39^{+0.94}_{-0.96}$	$5.99^{+2.41}_{-2.41}$	$(2.64^{+1.07}_{-1.07}) \times 10^{46}$	Q	1.118		

continued.

Name ^a	Common Name	SNR ^b	Γ^c	$F_{20-100\text{keV}}^d$ [$10^{-12} \frac{\text{erg}}{\text{cm}^2 \text{s}}$]	$L_{20-100\text{keV}}$ [erg s^{-1}]	Type ^e	z	X-ray det. ^f	γ -ray det. ^g
1758+388		-0.23		$0.05_{-0.00}^{+0.001*}$	$(1.21_{-0.09}^{+0.09}) \times 10^{45}$	Q	2.092		
1800+440	S4 1800+44	1.64		$0.83_{-0.05}^{+0.07\dagger*}$	$(1.40_{-0.10}^{+0.10}) \times 10^{45}$	Q	0.663		
1803+784	S5 1803+784	4.19	$1.66_{-0.94}^{+1.04}$	$5.88_{-2.10}^{+2.07}$	$(9.95_{-3.55}^{+3.50}) \times 10^{45}$	B	0.6797		3
1807+698	3C 371	1.72		$2.05_{-0.24}^{+0.29*}$	$(1.23_{-0.15}^{+0.15}) \times 10^{43}$	B	0.051		3
1823+568	4C +56.27	3.18	$2.07_{-1.27}^{+1.98}$	$3.48_{-2.06}^{+2.08}$	$(6.88_{-4.07}^{+4.11}) \times 10^{45}$	B	0.664		3
1828+487	3C 380	6.82	$1.67_{-0.47}^{+0.49}$	$10.72_{-2.21}^{+2.20}$	$(1.90_{-0.39}^{+0.39}) \times 10^{46}$	Q	0.692	1	3
1849+670	S4 1849+67	4.36	$1.86_{-0.90}^{+1.09}$	$5.16_{-2.08}^{+2.06}$	$(8.92_{-3.60}^{+3.57}) \times 10^{45}$	Q	0.657	1	3
1928+738	4C +73.18	5.95	$2.10_{-0.55}^{+0.64}$	$7.57_{-2.07}^{+2.08}$	$(2.25_{-0.61}^{+0.62}) \times 10^{45}$	Q	0.302	1	
1936-155		-2.02		$0.04^{\dagger*}$	5.94×10^{44}	Q	1.657		
1957+405	Cygnus A	57.86	$1.93_{-0.06}^{+0.06}$	$81.28_{-2.30}^{+2.30}$	$(5.92_{-0.17}^{+0.17}) \times 10^{44}$	G	0.0561	1, 2	
1958-179	PKS 1958-179	2.70		$3.79_{-0.22}^{+0.33*}$	$(6.07_{-0.45}^{+0.44}) \times 10^{45}$	Q	0.652	2	3
2005+403		3.79	$1.10_{-0.74}^{+0.65}$	$7.99_{-2.29}^{+2.28}$	$(6.73_{-1.92}^{+1.92}) \times 10^{46}$	Q	1.736		
2008-159	PKS 2008-159	5.12	$0.98_{-0.87}^{+0.74}$	$10.23_{-2.99}^{+2.99}$	$(3.67_{-1.07}^{+1.07}) \times 10^{46}$	Q	1.18	1	
2021+317	4C +31.56	-0.60		$0.04^{\dagger*}$		U			
2021+614	OW 637	1.98		$2.52_{-0.14}^{+0.33*}$	$(3.93_{-0.35}^{+0.38}) \times 10^{44}$	G	0.227		
2037+511	3C 418	3.24	$1.80_{-0.85}^{+0.94}$	$4.55_{-2.13}^{+2.15}$	$(7.22_{-3.37}^{+3.41}) \times 10^{46}$	Q	1.686		
2121+053	PKS 2121+053	1.26		$1.62_{-0.09}^{+0.14*}$	$(3.43_{-0.25}^{+0.25}) \times 10^{46}$	Q	1.941		
2128-123	PKS 2128-12	-1.52		$0.04^{\dagger*}$	3.52×10^{43}	Q	0.501		
2131-021	4C -02.81	0.30		$0.04^{\dagger*}$	3.27×10^{44}	Q	1.284		3
2134+004	PKS 2134+004	1.33		$2.53_{-0.14}^{+0.22*}$	$(5.31_{-0.39}^{+0.39}) \times 10^{46}$	Q	1.932		
2136+141	OX 161	2.76		$4.23_{-0.24}^{+0.37*}$	$(1.50_{-0.11}^{+0.11}) \times 10^{47}$	Q	2.427		
2145+067	4C +06.69	8.16	$1.68_{-0.45}^{+0.48}$	$12.65_{-2.62}^{+2.62}$	$(5.20_{-1.08}^{+1.08}) \times 10^{46}$	Q	0.999		3
2155-152	PKS 2155-152	-0.64		$0.04^{\dagger*}$	7.02×10^{43}	Q	0.672		3
2200+420	BL Lac	12.13	$1.83_{-0.28}^{+0.29}$	$17.22_{-2.25}^{+2.24}$	$(1.90_{-0.25}^{+0.25}) \times 10^{44}$	B	0.0686	1, 2	3
2201+171	PKS 2201+171	0.68		$1.68_{-0.10}^{+0.15*}$	$(8.90_{-0.66}^{+0.65}) \times 10^{45}$	Q	1.076		3

continued.

Name ^a	Common Name	SNR ^b	Γ^c	$F_{20-100\text{ keV}}^d$ [$10^{-12} \frac{\text{erg}}{\text{s cm}^2}$]	$L_{20-100\text{ keV}}$ [erg s^{-1}]	Type ^e	z	X-ray det. ^f	γ -ray det. ^g
2201+315	4C +31.63	6.12	$1.88^{+0.57}_{-0.54}$	$8.47^{+2.25}_{-2.24}$	$(2.25^{+0.60}_{-0.56}) \times 10^{45}$	Q	0.2947	1	
2209+236	PKS 2209+236	3.20	$2.73^{+4.40}_{-1.49}$	$3.14^{+2.31}_{-2.20}$	$(3.85^{+2.83}_{-2.70}) \times 10^{46}$	Q	1.125		3
2216-038	PKS 2216-03	1.54		$2.10^{+0.18*}_{-0.12}$	$(7.29^{+0.53}_{-0.54}) \times 10^{45}$	Q	0.901		
2223-052	3C 446	1.54		$1.99^{+0.17*}_{-0.11}$	$(1.98^{+0.14}_{-0.15}) \times 10^{46}$	Q	1.404		3
2227-088	PHL 5225	5.99	$1.10^{+0.54}_{-0.60}$	$11.26^{+2.73}_{-2.73}$	$(7.75^{+1.88}_{-1.88}) \times 10^{46}$	Q	1.5595	1	3
2230+114	CTA 102	7.93	$1.54^{+0.46}_{-0.46}$	$13.08^{+2.54}_{-2.55}$	$(5.45^{+1.06}_{-1.06}) \times 10^{46}$	Q	1.037	1	3
2243-123	PKS 2243-123	1.12		$2.23^{+0.20*}_{-0.13}$	$(3.34^{+0.24}_{-0.25}) \times 10^{45}$	Q	0.632		
2251+158	3C 454.3	44.20	$1.49^{+0.08}_{-0.08}$	$70.54^{+2.41}_{-2.41}$	$(1.86^{+0.06}_{-0.06}) \times 10^{47}$	Q	0.859	1	3
2331+073	TXS 2331+073	1.76		$1.82^{+0.16*}_{-0.10}$	$(9.42^{+0.68}_{-0.70}) \times 10^{44}$	Q	0.401		3
2345-167	PKS 2345-16	0.45		$0.04^{+0.00\dagger*}_{-0.00}$	$(4.88^{+0.35}_{-0.36}) \times 10^{43}$	Q	0.576		3
2351+456	4C +45.51	0.36		$0.52^{+0.05\dagger*}_{-0.03}$	$(1.16^{+0.08}_{-0.09}) \times 10^{46}$	Q	1.986		

Notes. a) Name in IAU B1950 format, b) *Swift*/BAT SNR (70 month survey data), c) Photon Index for 20–100 keV, d) X-ray flux (* indicates fluxes calculated by assuming a photon index based on the sources with SNR > 3.0; † for upper limits), e) optical classification (Véron-Cetty & Véron, 2003), f) published hard X-ray detection in: 1) *Swift*/BAT survey catalogue for 58 months (Baumgartner et al., 2010) 2) INTEGRAL nine-year Galactic Hard X-ray Survey (Krivonos et al., 2012), * detected object: Perseus Cluster, g) 3) published Gamma-ray detection from the Fermi IFGL catalogue (Abdo et al., 2010b)

C Partial Kendall's Tau - SLANG Program

```
% -----  
% COMPUTE PARTIAL CORRELATION COEFFICIENT AND  
% SIGNIFICANCE FOR CENSORED DATA  
%  
% THE CODE IS BASED ON THE METHODOLOGY PRESENTED IN  
% 'A test for partial correlation with censored  
% astronomical data'  
% BY  
% M.G.Akritis and J.Siebert  
% Monthly Notices of the Royal Astronomical Society  
% 278, 919-924, 1996  
%  
% ISIS program (conversion from FORTRAN) by Langejahn, M.  
% -----  
  
require("isisscripts");  
require("stats");  
Minimum_Stat_Err = 1e-30;  
  
%%%%%%%%% DATASET %%%%%%%%%%  
%% dataset in text file has to be formatted as follows:  
% -both datasets that are to be checked for partial correlation  
% -are designated as x and y with the third dependent parameter z  
% -columns that indicate upper limits are designated as x_UL, y_UL, and z_UL  
% (1 = detection, 0 = upper limit)  
variable data = ascii_read_table ("file.txt",{"%F","x"},{"%F","x_UL"},{"%F","y"},{"%F","y_UL"},{"%F","z"},  
{"%F","z_UL"});  
variable ntot = length(data.x);  
variable dat = Double.Type[ntot,3];  
variable idat = Double.Type[ntot,3];  
variable p;  
for(p=0; p<=ntot-1; p++){  
  dat[p,0]=-data.x[p]; % chance - to + for right censoring  
  dat[p,1]=-data.y[p]; % chance - to + for right censoring  
  dat[p,2]=-data.z[p]; % chance - to + for right censoring  
  idat[p,0]=data.x_UL[p];  
  idat[p,1]=data.y_UL[p];  
  idat[p,2]=data.z_UL[p];  
}  
%% columns of dat:  
variable k1 = 0;%dat.rlum;  
variable k2 = 1;%dat.xlum;  
variable k3 = 2;%dat.z;  
  
%%%%%%%%% FUNCTIONS %%%%%%%%%%  
%% FUNCTION: value of h (see formula) %%%%%%%%%%  
define h(k,l,i,j)  
{  
  variable cj1=-idat[j,k];  
  if(dat[i,k] < dat[j,k]) cj1=idat[i,k];  
  variable cj2=-idat[j,l];  
  if(dat[i,l] < dat[j,l]) cj2=idat[i,l];  
  variable h=cj1*cj2;  
  return h;  
}  
  
%% FUNCTION: kendalls tau %%%%%%%%%%  
define tau(k,l)
```

```

{
variable ac = 2.0/(1.0*ntot*(1.0*ntot-1));
variable sum = 0.0;
variable i,j;
for (j=0; j<=ntot-1; j++){
for (i=0; i<=ntot-1; i++){
if(i >= j) break;
sum = sum + h(k,l,i,j);
}
}
variable tau = sum*ac;
return tau;
}

%%%%%%%% FUNCTION: partial kendalls tau %%%%%%%%%
define tau123()
{
variable res = (tau(k1,k2)-tau(k1,k3)*tau(k2,k3)) / sqrt((1.0-tau(k1,k3)2)*(1.0-tau(k2,k3)2));
return res;
}

%%%%%%%% FUNCTION: computes A_N (see formula) %%%%%%%%%
define an()
{
variable c1 = 16.0 / (1.0*ntot-1.0);
variable c2 = 6.0 / ((1.0*ntot-1.0)*(1.0*ntot-2.0)*(1.0*ntot-3.0));
variable asum = 0.0;
variable ave = 0.0;
variable aasum = Double.Type[ntot];
variable i1, i2, j1, j2, i;
for(i1=0; i1<=ntot-1; i1++){ %%% outer summation (i1)
print(i1);
for(j1=0; j1<=ntot-3; j1++){ %%% inner summation with j1<i2<j2 and all != i1
if(j1 == i1) continue;
for(j2=j1+2; j2<=ntot-1; j2++){
if(j2 == i1) continue;
for(i2=j1+1; i2<=j2-1; i2++){
if(i2 == i1) continue;
variable cj1, cj2, cj3, cj4, cj5, cj6, cj7;
variable gtsum = 0.0;
cj1= idat[j1,k1];
if(dat[i1,k1]<dat[j1,k1]) cj1=idat[i1,k1];
cj2= idat[j1,k2];
if(dat[i1,k2]<dat[j1,k2]) cj2=idat[i1,k2];
cj3= idat[j1,k3];
if(dat[i1,k3]<dat[j1,k3]) cj3=idat[i1,k3];
cj4= idat[j2,k2];
if(dat[i2,k2]<dat[j2,k2]) cj4=idat[i2,k2];
cj5= idat[j2,k3];
if(dat[i2,k3]<dat[j2,k3]) cj5=idat[i2,k3];
cj6= idat[i2,k2];
if(dat[j2,k2]<dat[i2,k2]) cj6=idat[j2,k2];
cj7= idat[i2,k3];
if(dat[j2,k3]<dat[i2,k3]) cj7=idat[j2,k3];
gtsum=cj1*(2.0*cj2 - cj3*(cj4*cj5+cj6*cj7) );
cj1= idat[j2,k1];
if(dat[i1,k1]<dat[j2,k1]) cj1=idat[i1,k1];
cj2= idat[j2,k2];
if(dat[i1,k2]<dat[j2,k2]) cj2=idat[i1,k2];
cj3= idat[j2,k3];
if(dat[i1,k3]<dat[j2,k3]) cj3=idat[i1,k3];
cj4= idat[j1,k2];
if(dat[i2,k2]<dat[j1,k2]) cj4=idat[i2,k2];
cj5= idat[j1,k3];
if(dat[i2,k3]<dat[j1,k3]) cj5=idat[i2,k3];
cj6= idat[i2,k2];

```

```

if(dat[j1,k2]<dat[i2,k2]) cj6=idat[j1,k2];
cj7=- idat[i2,k3];
if(dat[j1,k3]<dat[i2,k3]) cj7=idat[j1,k3];
gtsum=gtsum+cj1*(2.0*cj2 - cj3*(cj4*cj5+cj6*cj7) );
cj1=- idat[i2,k1];
if(dat[i1,k1]<dat[i2,k1]) cj1=idat[i1,k1];
cj2=- idat[i2,k2];
if(dat[i1,k2]<dat[i2,k2]) cj2=idat[i1,k2];
cj3=- idat[i2,k3];
if(dat[i1,k3]<dat[i2,k3]) cj3=idat[i1,k3];
cj4=- idat[j1,k2];
if(dat[j2,k2]<dat[j1,k2]) cj4=idat[j2,k2];
cj5=- idat[j1,k3];
if(dat[j2,k3]<dat[j1,k3]) cj5=idat[j2,k3];
cj6=- idat[j2,k2];
if(dat[j1,k2]<dat[j2,k2]) cj6=idat[j1,k2];
cj7=- idat[j2,k3];
if(dat[j1,k3]<dat[j2,k3]) cj7=idat[j1,k3];
gtsum=gtsum+cj1*(2.0*cj2 - cj3*(cj4*cj5+cj6*cj7) );
cj1=- idat[i1,k1];
if(dat[j1,k1]<dat[i1,k1]) cj1=idat[j1,k1];
cj2=- idat[i1,k2];
if(dat[j1,k2]<dat[i1,k2]) cj2=idat[j1,k2];
cj3=- idat[i1,k3];
if(dat[j1,k3]<dat[i1,k3]) cj3=idat[j1,k3];
cj4=- idat[j2,k2];
if(dat[i2,k2]<dat[j2,k2]) cj4=idat[i2,k2];
cj5=- idat[j2,k3];
if(dat[i2,k3]<dat[j2,k3]) cj5=idat[i2,k3];
cj6=- idat[i2,k2];
if(dat[j2,k2]<dat[i2,k2]) cj6=idat[j2,k2];
cj7=- idat[i2,k3];
if(dat[j2,k3]<dat[i2,k3]) cj7=idat[j2,k3];
gtsum=gtsum+cj1*(2.0*cj2 - cj3*(cj4*cj5+cj6*cj7) );
cj1=- idat[i2,k1];
if(dat[j1,k1]<dat[i2,k1]) cj1=idat[j1,k1];
cj2=- idat[i2,k2];
if(dat[j1,k2]<dat[i2,k2]) cj2=idat[j1,k2];
cj3=- idat[i2,k3];
if(dat[j1,k3]<dat[i2,k3]) cj3=idat[j1,k3];
cj4=- idat[j2,k2];
if(dat[i1,k2]<dat[j2,k2]) cj4=idat[i1,k2];
cj5=- idat[j2,k3];
if(dat[i1,k3]<dat[j2,k3]) cj5=idat[i1,k3];
cj6=- idat[i1,k2];
if(dat[j2,k2]<dat[i1,k2]) cj6=idat[j2,k2];
cj7=- idat[i1,k3];
if(dat[j2,k3]<dat[i1,k3]) cj7=idat[j2,k3];
gtsum=gtsum+cj1*(2.0*cj2 - cj3*(cj4*cj5+cj6*cj7) );
cj1=- idat[j2,k1];
if(dat[j1,k1]<dat[j2,k1]) cj1=idat[j1,k1];
cj2=- idat[j2,k2];
if(dat[j1,k2]<dat[j2,k2]) cj2=idat[j1,k2];
cj3=- idat[j2,k3];
if(dat[j1,k3]<dat[j2,k3]) cj3=idat[j1,k3];
cj4=- idat[i2,k2];
if(dat[i1,k2]<dat[i2,k2]) cj4=idat[i1,k2];
cj5=- idat[i2,k3];
if(dat[i1,k3]<dat[i2,k3]) cj5=idat[i1,k3];
cj6=- idat[i1,k2];
if(dat[i2,k2]<dat[i1,k2]) cj6=idat[i2,k2];
cj7=- idat[i1,k3];
if(dat[i2,k3]<dat[i1,k3]) cj7=idat[i2,k3];
gtsum=gtsum+cj1*(2.0*cj2 - cj3*(cj4*cj5+cj6*cj7) );
cj1=- idat[i1,k1];
if(dat[i2,k1]<dat[i1,k1]) cj1=idat[i2,k1];

```

```

cj2= idat[i1,k2];
if(dat[i2,k2]<dat[i1,k2]) cj2=idat[i2,k2];
cj3= idat[i1,k3];
if(dat[i2,k3]<dat[i1,k3]) cj3=idat[i2,k3];
cj4= idat[j2,k2];
if(dat[j1,k2]<dat[j2,k2]) cj4=idat[j1,k2];
cj5= idat[j2,k3];
if(dat[j1,k3]<dat[j2,k3]) cj5=idat[j1,k3];
cj6= idat[j1,k2];
if(dat[j2,k2]<dat[j1,k2]) cj6=idat[j2,k2];
cj7= idat[j1,k3];
if(dat[j2,k3]<dat[j1,k3]) cj7=idat[j2,k3];
gtsum=gtsum+cj1*(2.0*cj2 - cj3*(cj4*cj5+cj6*cj7) );
cj1= idat[j1,k1];
if(dat[i2,k1]<dat[j1,k1]) cj1=idat[i2,k1];
cj2= idat[j1,k2];
if(dat[i2,k2]<dat[j1,k2]) cj2=idat[i2,k2];
cj3= idat[j1,k3];
if(dat[i2,k3]<dat[j1,k3]) cj3=idat[i2,k3];
cj4= idat[j2,k2];
if(dat[i1,k2]<dat[j2,k2]) cj4=idat[i1,k2];
cj5= idat[j2,k3];
if(dat[i1,k3]<dat[j2,k3]) cj5=idat[i1,k3];
cj6= idat[i1,k2];
if(dat[j2,k2]<dat[i1,k2]) cj6=idat[j2,k2];
cj7= idat[i1,k3];
if(dat[j2,k3]<dat[i1,k3]) cj7=idat[j2,k3];
gtsum=gtsum+cj1*(2.0*cj2 - cj3*(cj4*cj5+cj6*cj7) );
cj1= idat[j2,k1];
if(dat[i2,k1]<dat[j2,k1]) cj1=idat[i2,k1];
cj2= idat[j2,k2];
if(dat[i2,k2]<dat[j2,k2]) cj2=idat[i2,k2];
cj3= idat[j2,k3];
if(dat[i2,k3]<dat[j2,k3]) cj3=idat[i2,k3];
cj4= idat[j1,k2];
if(dat[i1,k2]<dat[j1,k2]) cj4=idat[i1,k2];
cj5= idat[j1,k3];
if(dat[i1,k3]<dat[j1,k3]) cj5=idat[i1,k3];
cj6= idat[i1,k2];
if(dat[j1,k2]<dat[i1,k2]) cj6=idat[j1,k2];
cj7= idat[i1,k3];
if(dat[j1,k3]<dat[i1,k3]) cj7=idat[j1,k3];
gtsum=gtsum+cj1*(2.0*cj2 - cj3*(cj4*cj5+cj6*cj7) );
cj1= idat[i1,k1];
if(dat[j2,k1]<dat[i1,k1]) cj1=idat[j2,k1];
cj2= idat[i1,k2];
if(dat[j2,k2]<dat[i1,k2]) cj2=idat[j2,k2];
cj3= idat[i1,k3];
if(dat[j2,k3]<dat[i1,k3]) cj3=idat[j2,k3];
cj4= idat[i2,k2];
if(dat[j1,k2]<dat[i2,k2]) cj4=idat[j1,k2];
cj5= idat[i2,k3];
if(dat[j1,k3]<dat[i2,k3]) cj5=idat[j1,k3];
cj6= idat[j1,k2];
if(dat[i2,k2]<dat[j1,k2]) cj6=idat[i2,k2];
cj7= idat[j1,k3];
if(dat[i2,k3]<dat[j1,k3]) cj7=idat[i2,k3];
gtsum=gtsum+cj1*(2.0*cj2 - cj3*(cj4*cj5+cj6*cj7) );
cj1= idat[j1,k1];
if(dat[j2,k1]<dat[j1,k1]) cj1=idat[j2,k1];
cj2= idat[j1,k2];
if(dat[j2,k2]<dat[j1,k2]) cj2=idat[j2,k2];
cj3= idat[j1,k3];
if(dat[j2,k3]<dat[j1,k3]) cj3=idat[j2,k3];
cj4= idat[i1,k2];
if(dat[i2,k2]<dat[i1,k2]) cj4=idat[i2,k2];

```

```

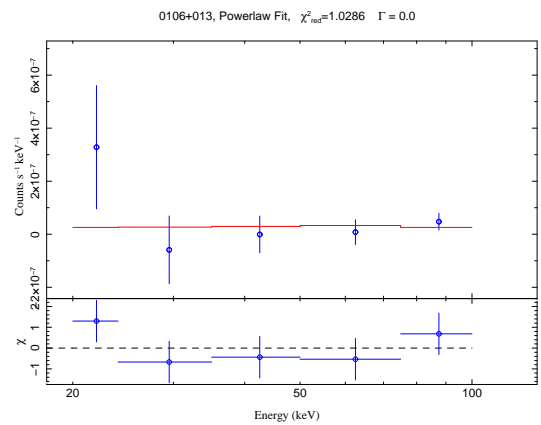
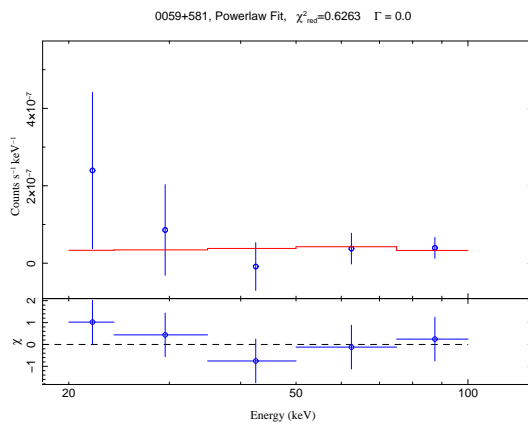
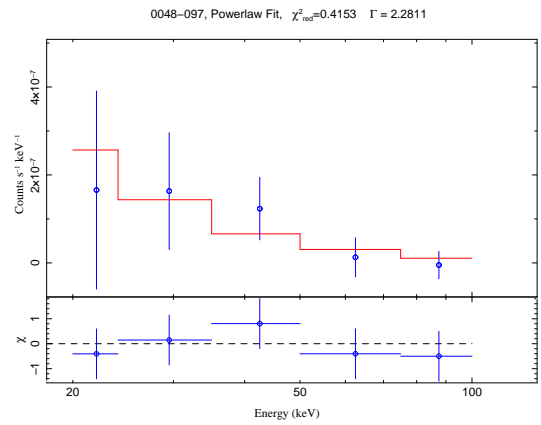
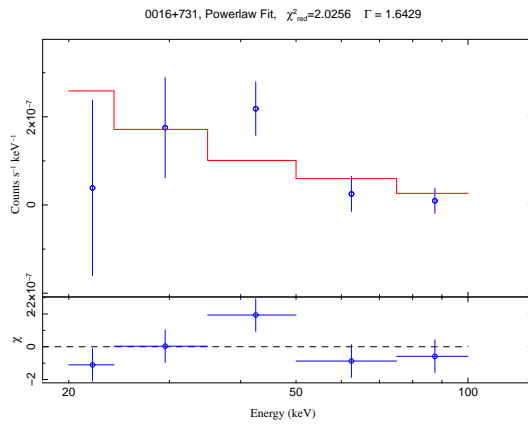
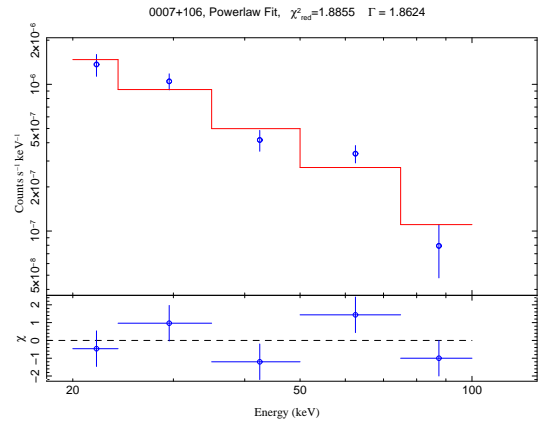
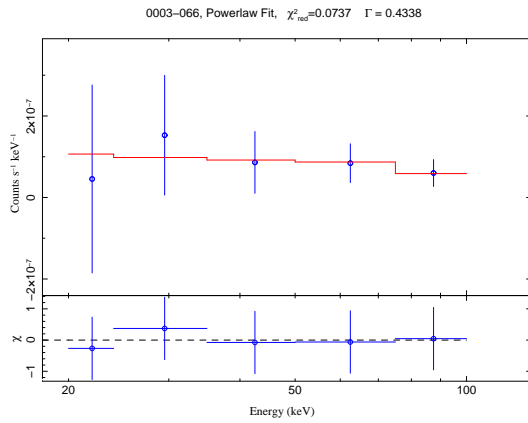
cj5= idat[i1,k3];
if(dat[i2,k3]<dat[i1,k3]) cj5=idat[i2,k3];
cj6= idat[i2,k2];
if(dat[i1,k2]<dat[i2,k2]) cj6=idat[i1,k2];
cj7= idat[i2,k3];
if(dat[i1,k3]<dat[i2,k3]) cj7=idat[i1,k3];
gtsum=gtsum+cj1*(2.0*cj2 - cj3*(cj4*cj5+cj6*cj7) );
cj1= idat[i2,k1];
if(dat[j2,k1]<dat[i2,k1]) cj1=idat[j2,k1];
cj2= idat[i2,k2];
if(dat[j2,k2]<dat[i2,k2]) cj2=idat[j2,k2];
cj3= idat[i2,k3];
if(dat[j2,k3]<dat[i2,k3]) cj3=idat[j2,k3];
cj4= idat[j1,k2];
if(dat[i1,k2]<dat[j1,k2]) cj4=idat[i1,k2];
cj5= idat[j1,k3];
if(dat[i1,k3]<dat[j1,k3]) cj5=idat[i1,k3];
cj6= idat[i1,k2];
if(dat[j1,k2]<dat[i1,k2]) cj6=idat[j1,k2];
cj7= idat[i1,k3];
if(dat[j1,k3]<dat[i1,k3]) cj7=idat[j1,k3];
gtsum=gtsum+cj1*(2.0*cj2 - cj3*(cj4*cj5+cj6*cj7) );
aasum[i1]=aasum[i1]+1.0/24.0*gtsum; %%% summation over permutations
}
}
}
ave = ave + c2*aasum[i1];
}
ave=ave/(1.0*ntot);
for(i=0; i<=ntot-1; i++){
asum=asum+(c2*aasum[i]-ave)2;
}
return asum*c1;
}

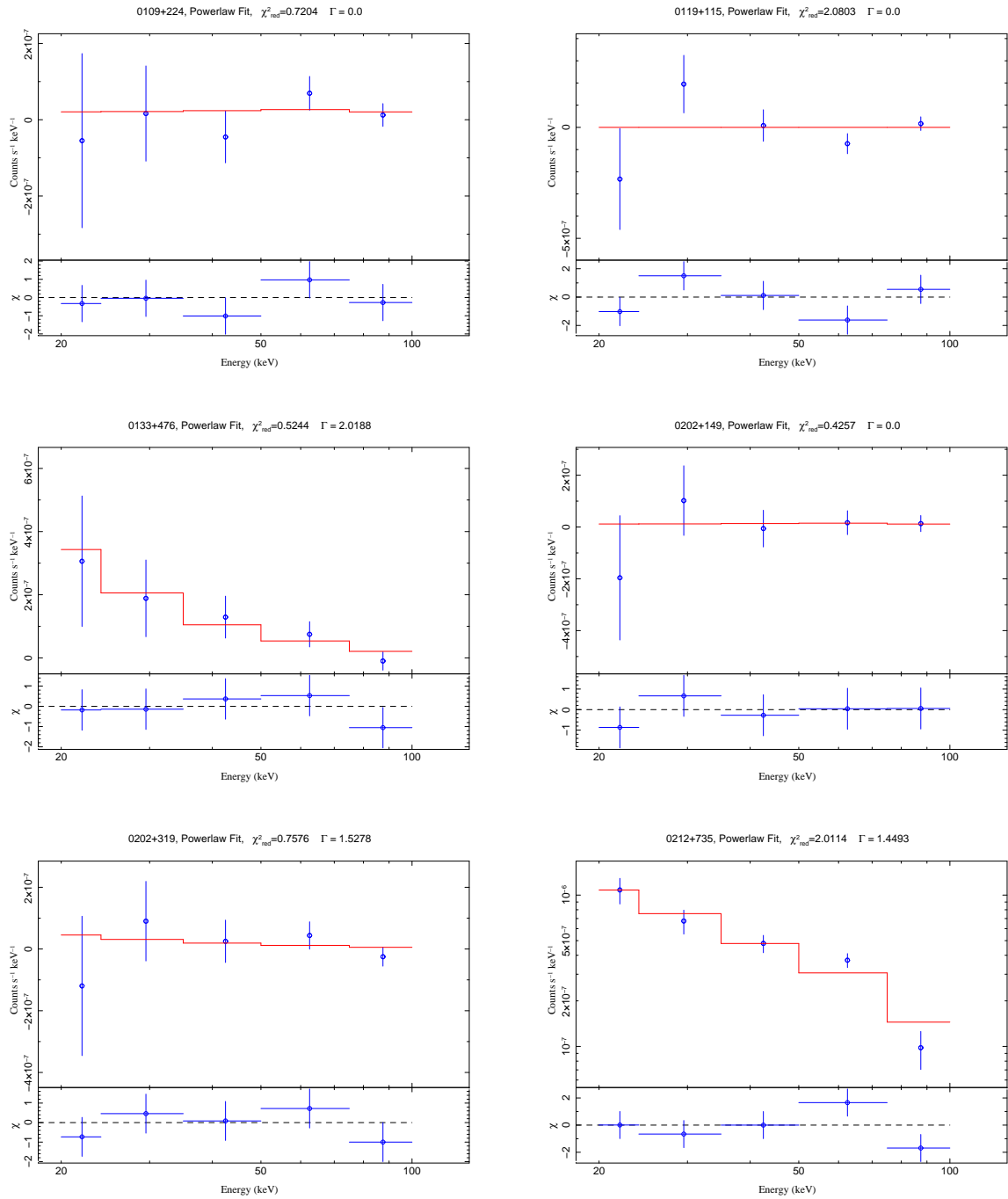
%%%%%%%%% FUNCTION: sigma, variance of statistic %%%%%%%%%%
define sigma()
{
variable sig2 = an()/(ntot*(1.0-tau(k1,k3)2)*(1.0-tau(k2,k3)2));
return sqrt(sig2);
}

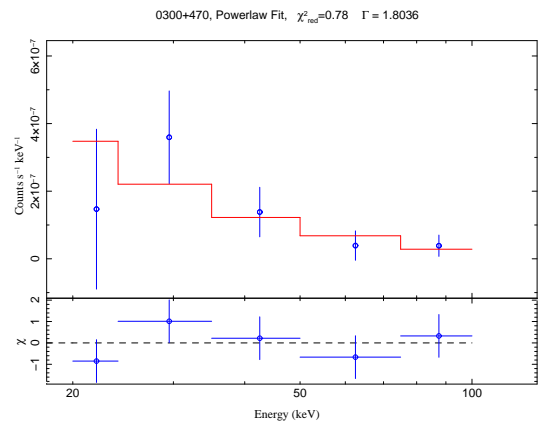
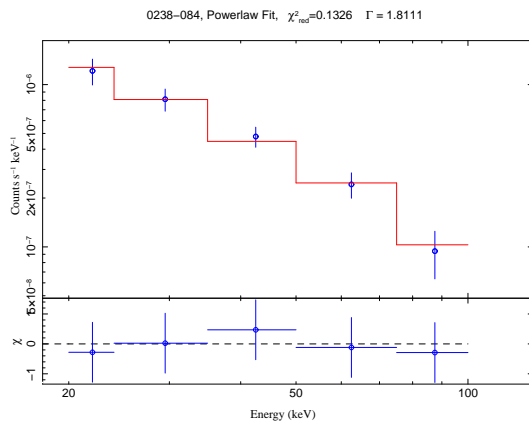
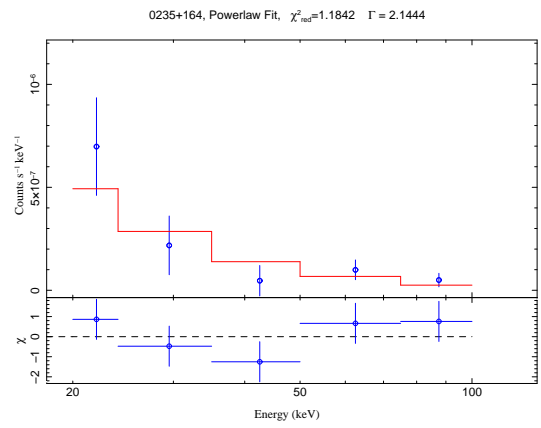
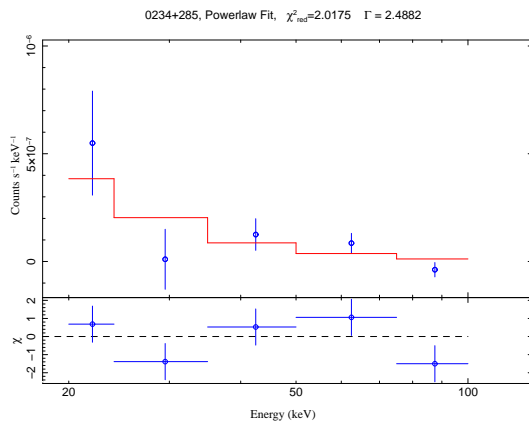
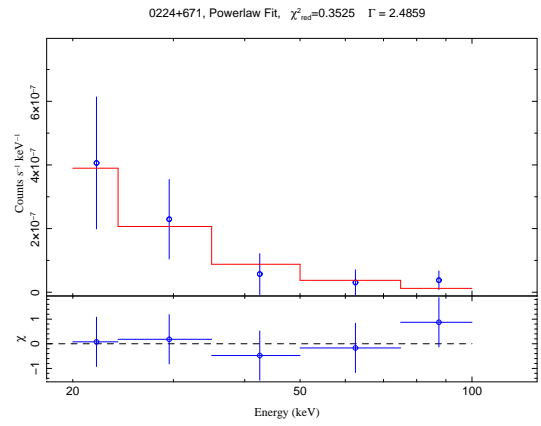
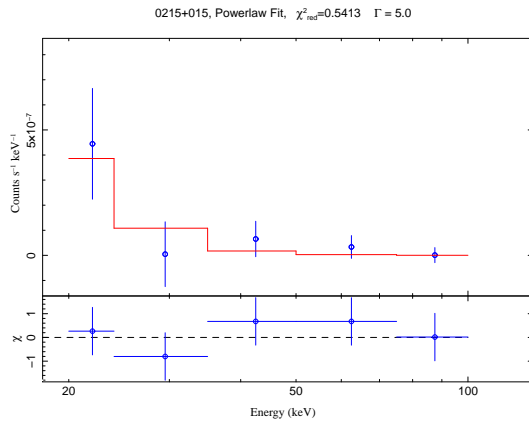
%%%%%%%%% START PROGRAM %%%%%%%%%%
print("—COMPUTE PARTIAL CORRELATION COEFFICIENT—");
print("Tau(1,2): " + sprintf("%S", tau(k1,k2)));
print("Tau(1,3): " + sprintf("%S", tau(k1,k3)));
print("Tau(2,3): " + sprintf("%S", tau(k2,k3)));
variable res = tau123();
print("-> Partial Kendalls tau: " + sprintf("%S", res));
print("Calculating variance...this takes some time...");
variable s = sigma();
print("Square root of variance (sigma): " + sprintf("%S", s));
if(abs(res/s) > 1.96) {
print("Zero partial correlation rejected at level 0.05");
}
else {
print("Null hypothesis cannot be rejected!");
print("-> No correlation present, if influence of third variable is excluded");
}
}

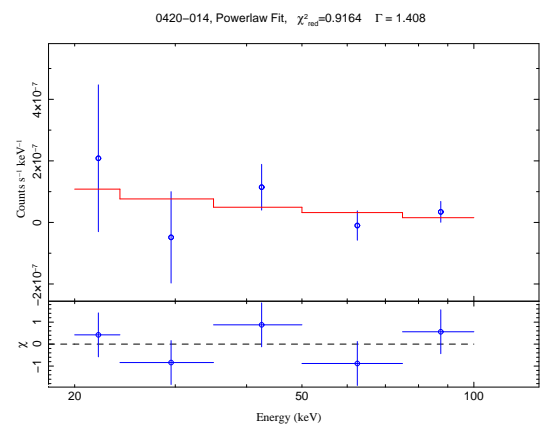
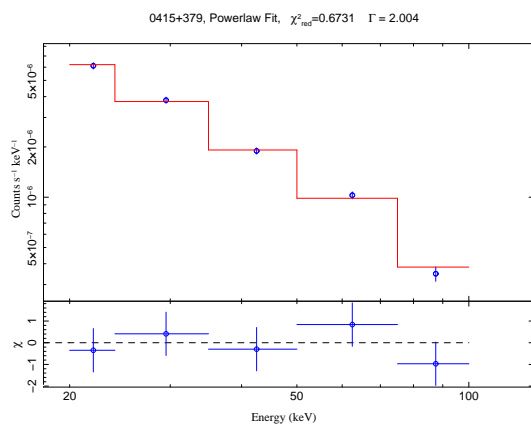
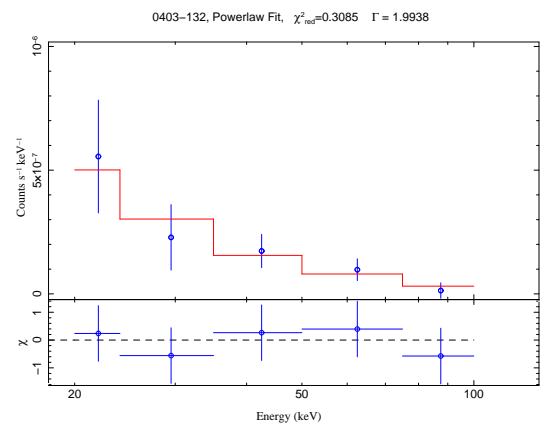
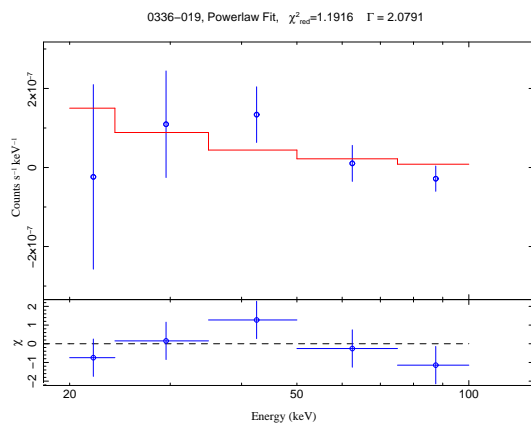
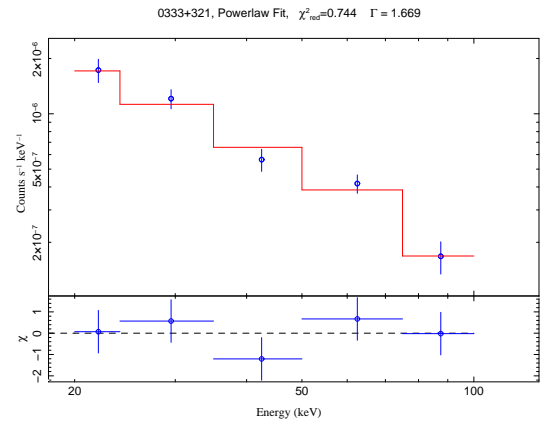
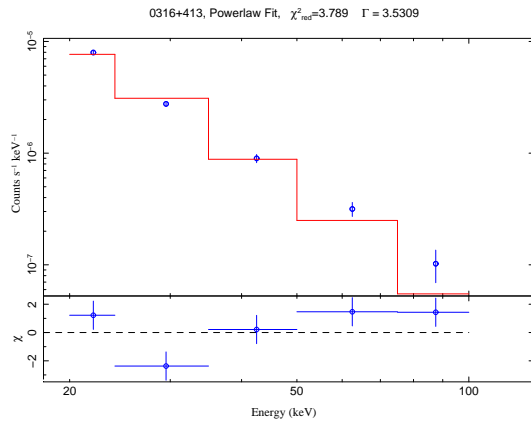
```

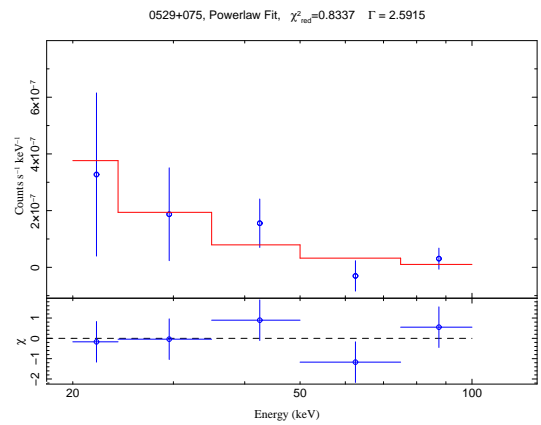
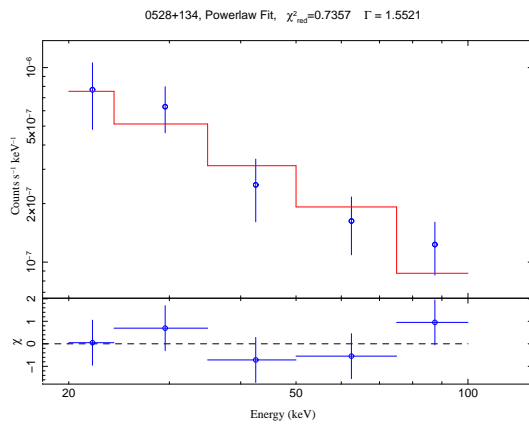
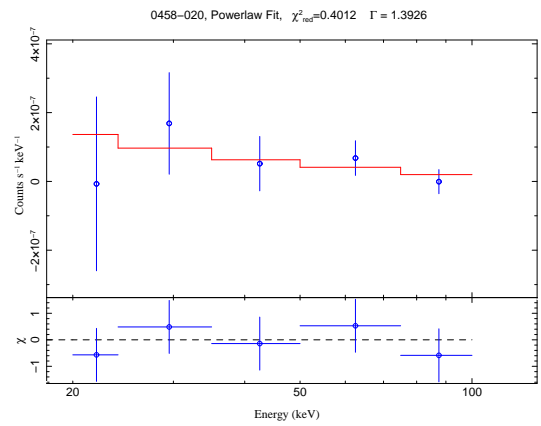
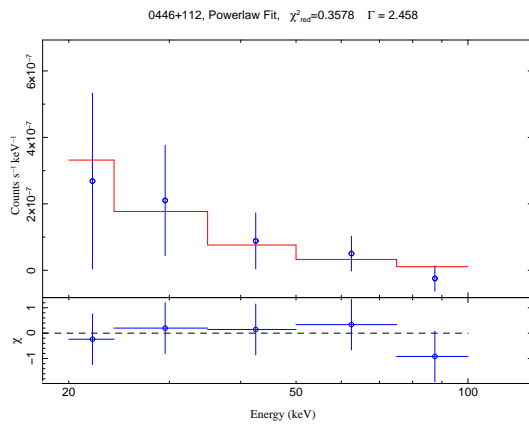
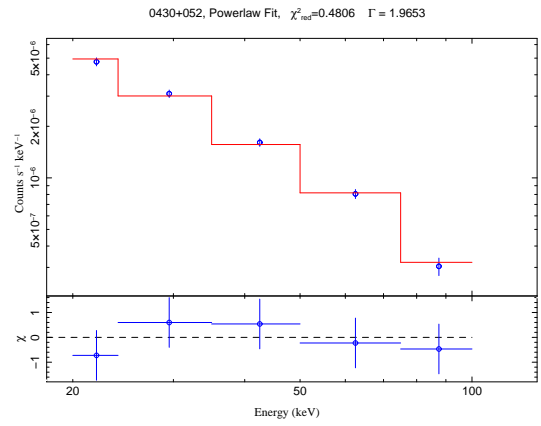
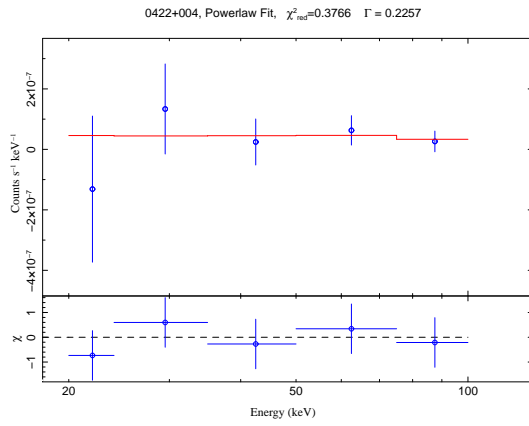

D BAT Spectra of the MOJAVE-1 Sample

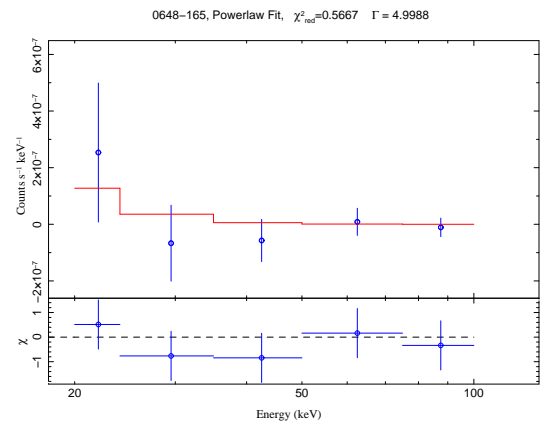
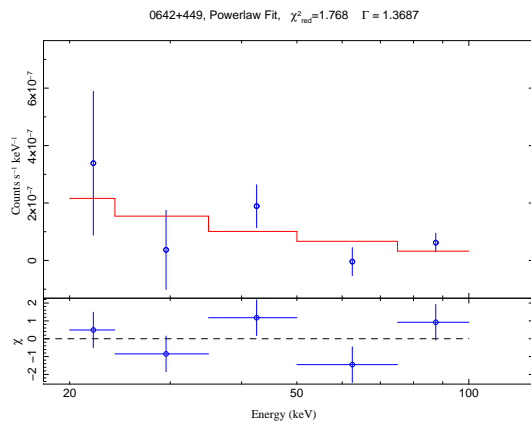
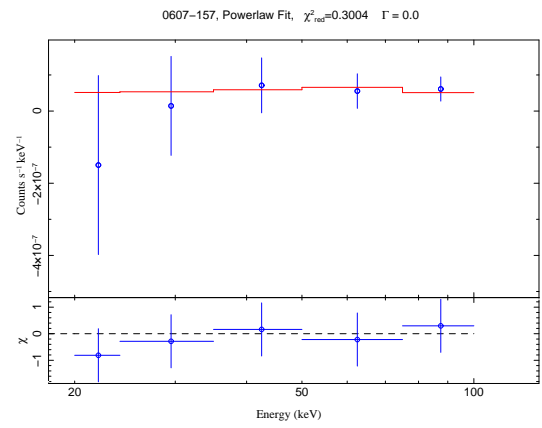
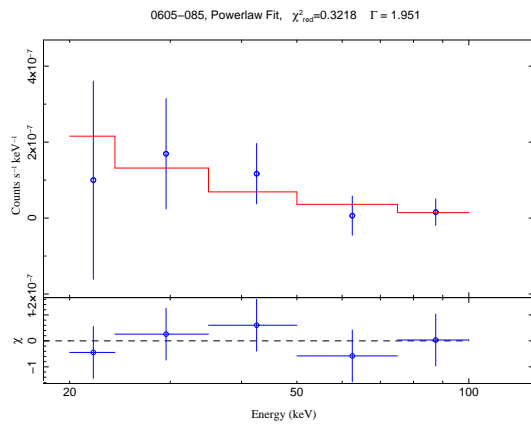
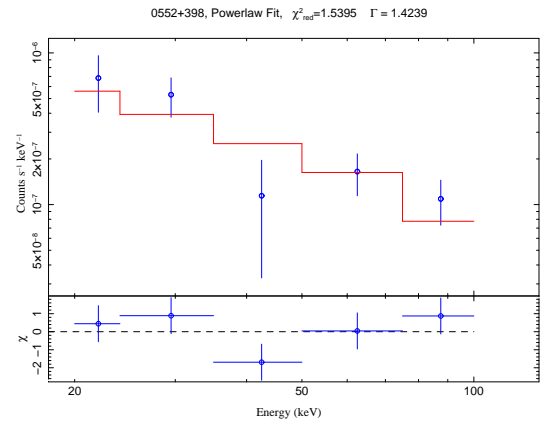
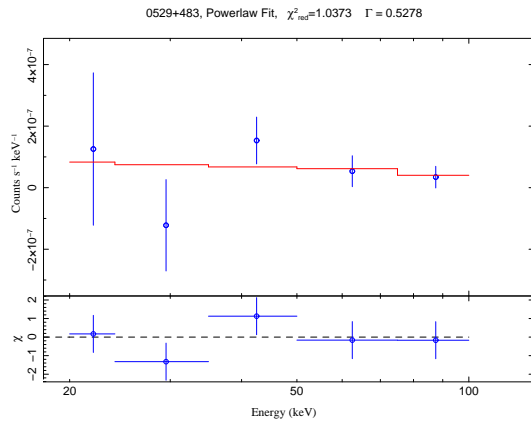


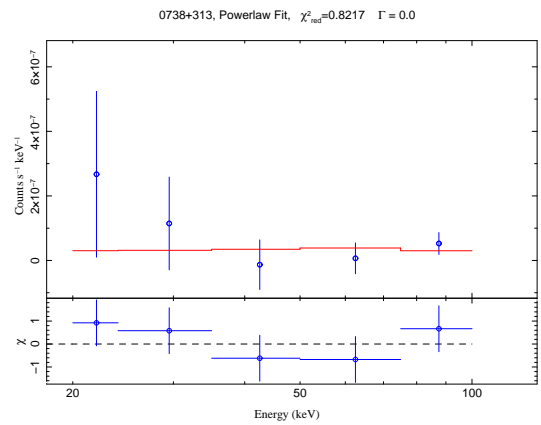
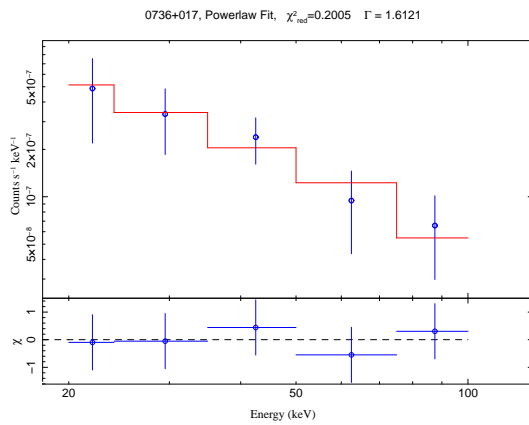
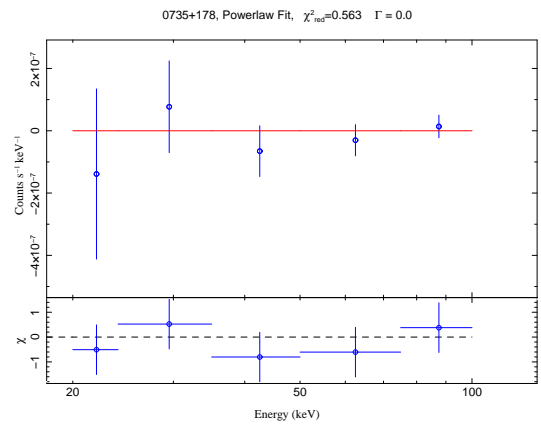
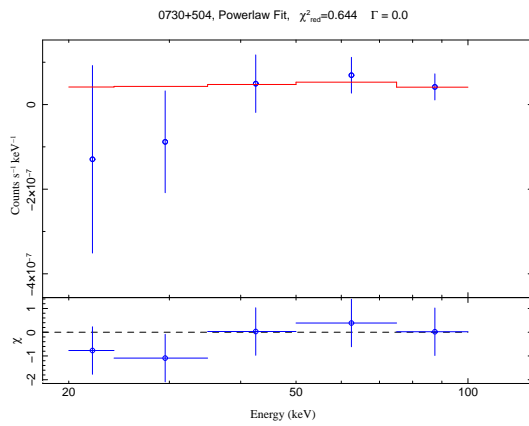
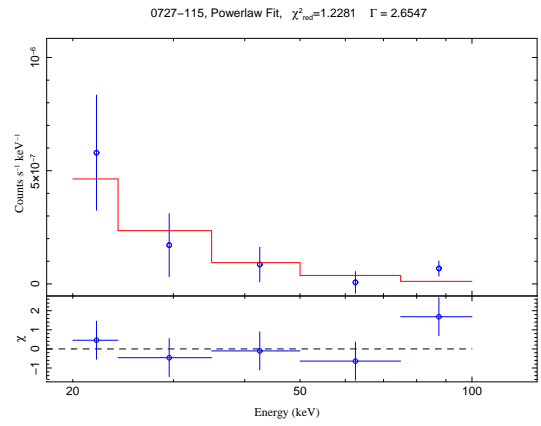
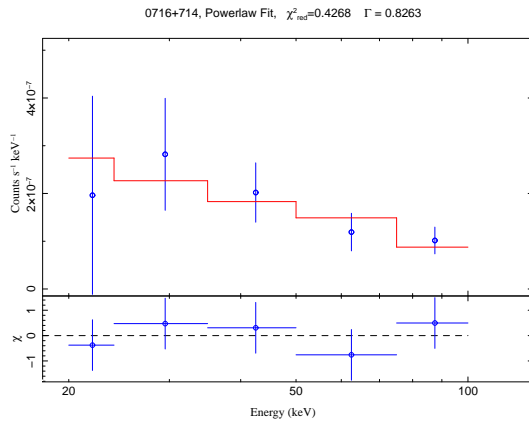


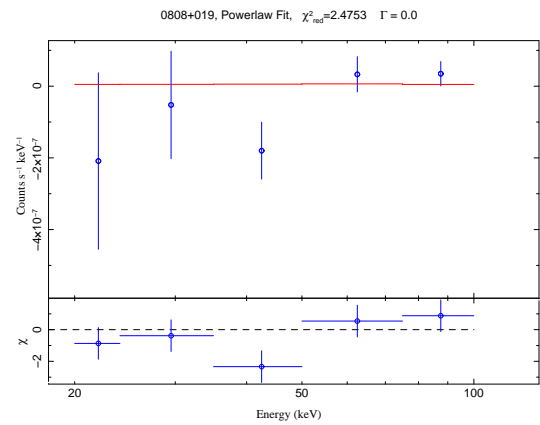
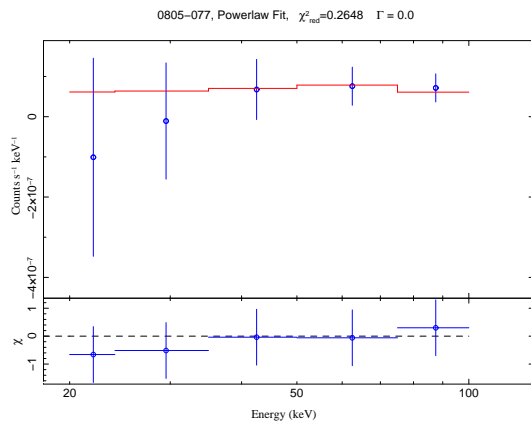
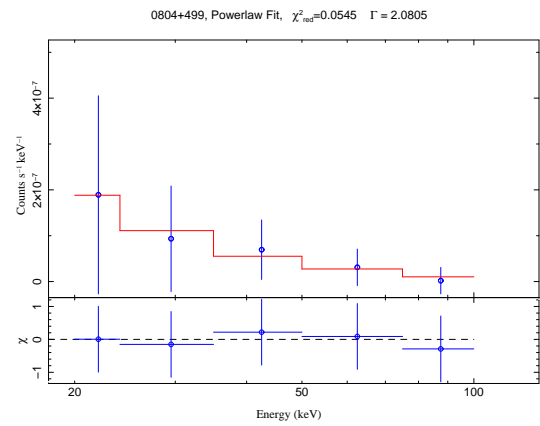
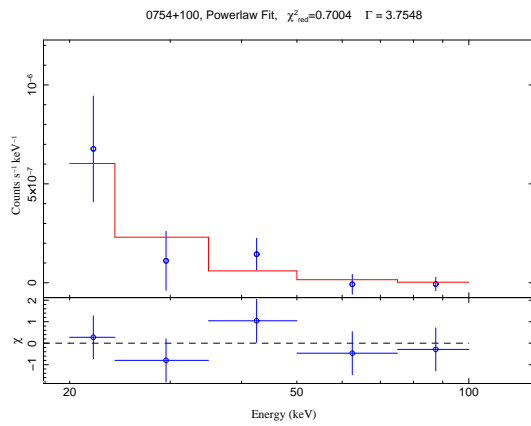
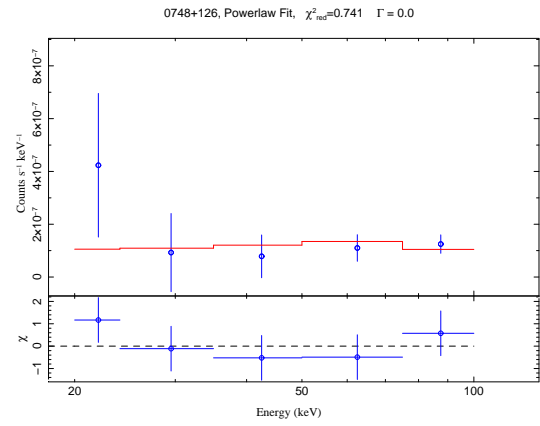
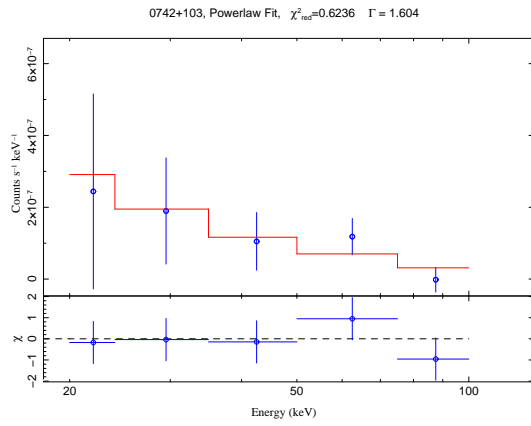


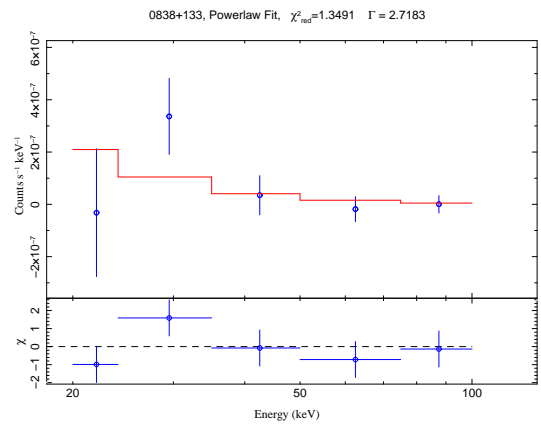
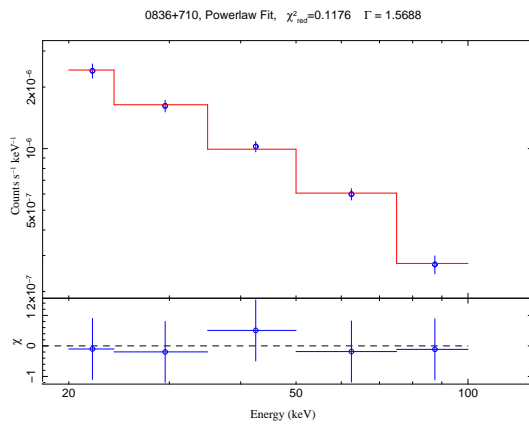
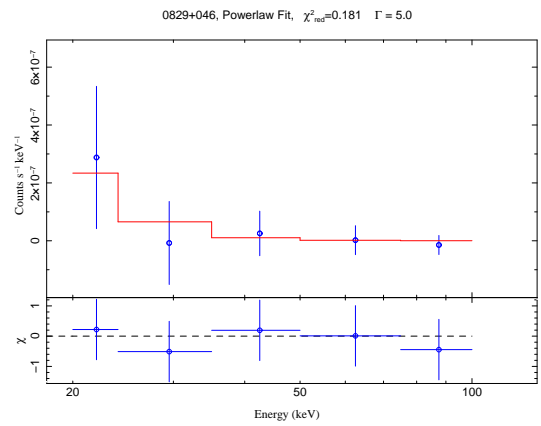
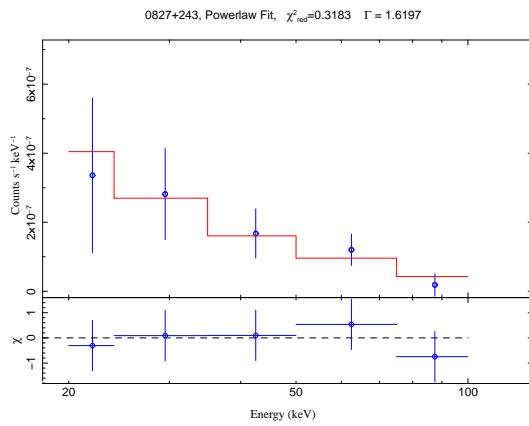
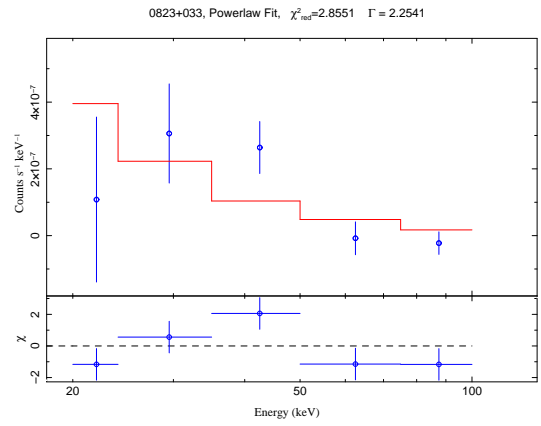
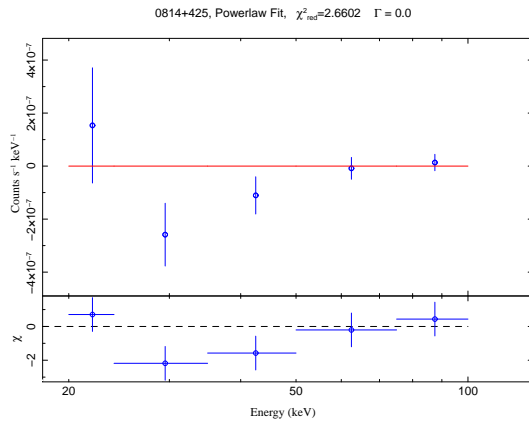


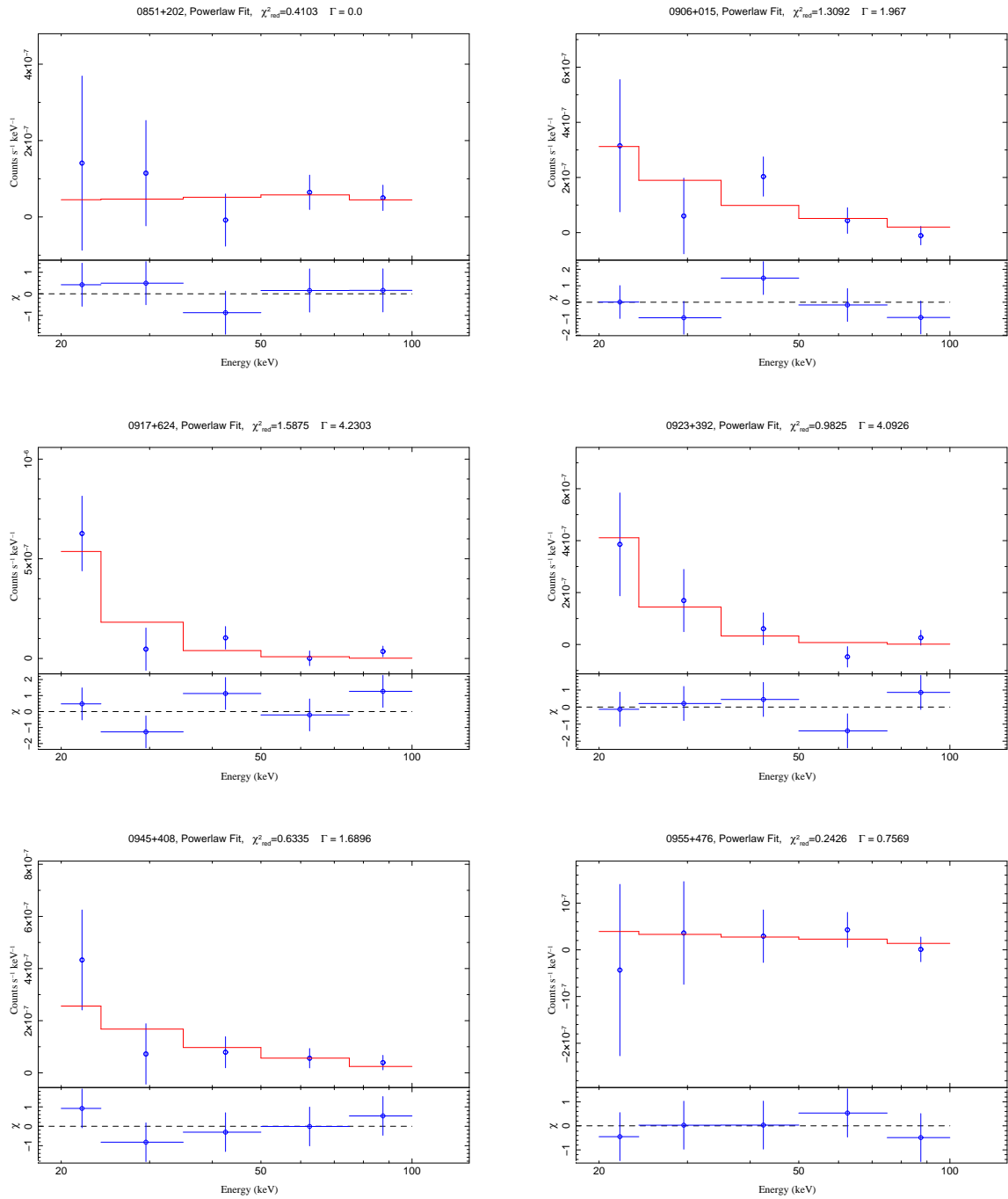


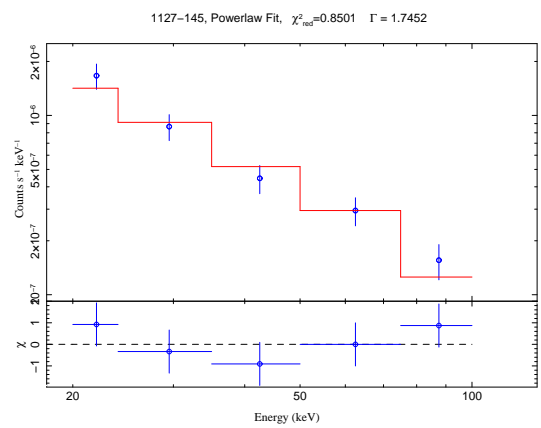
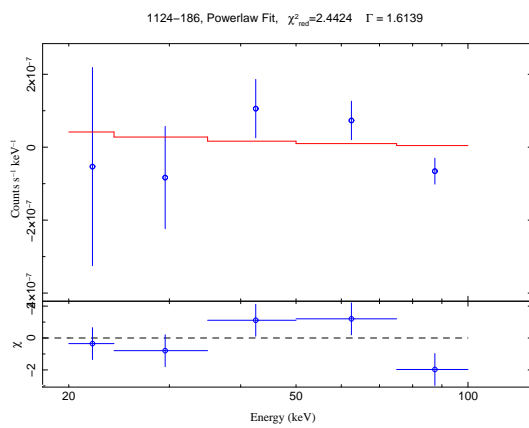
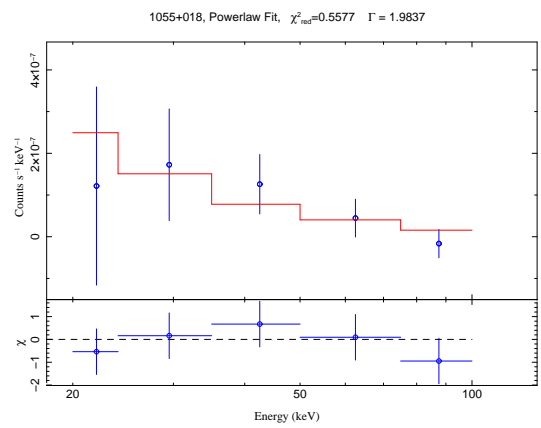
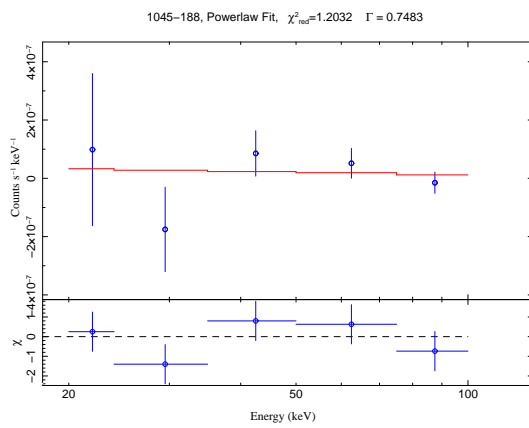
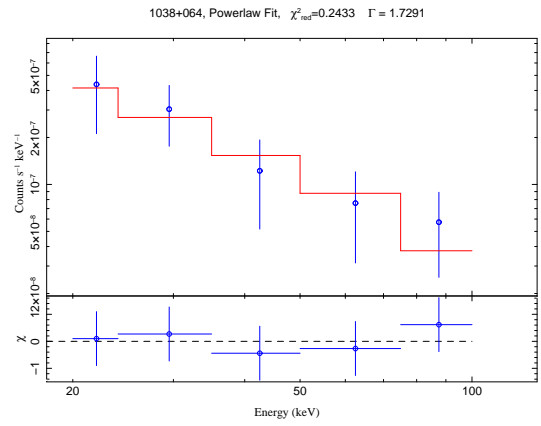
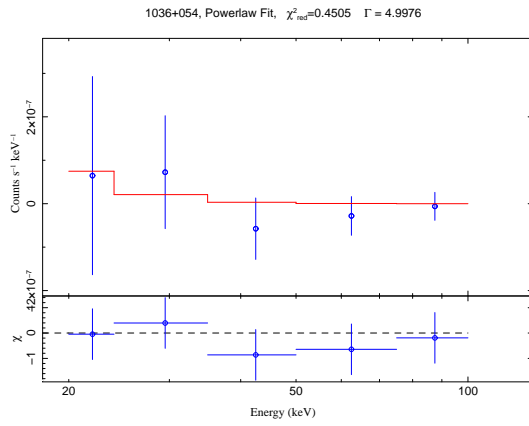


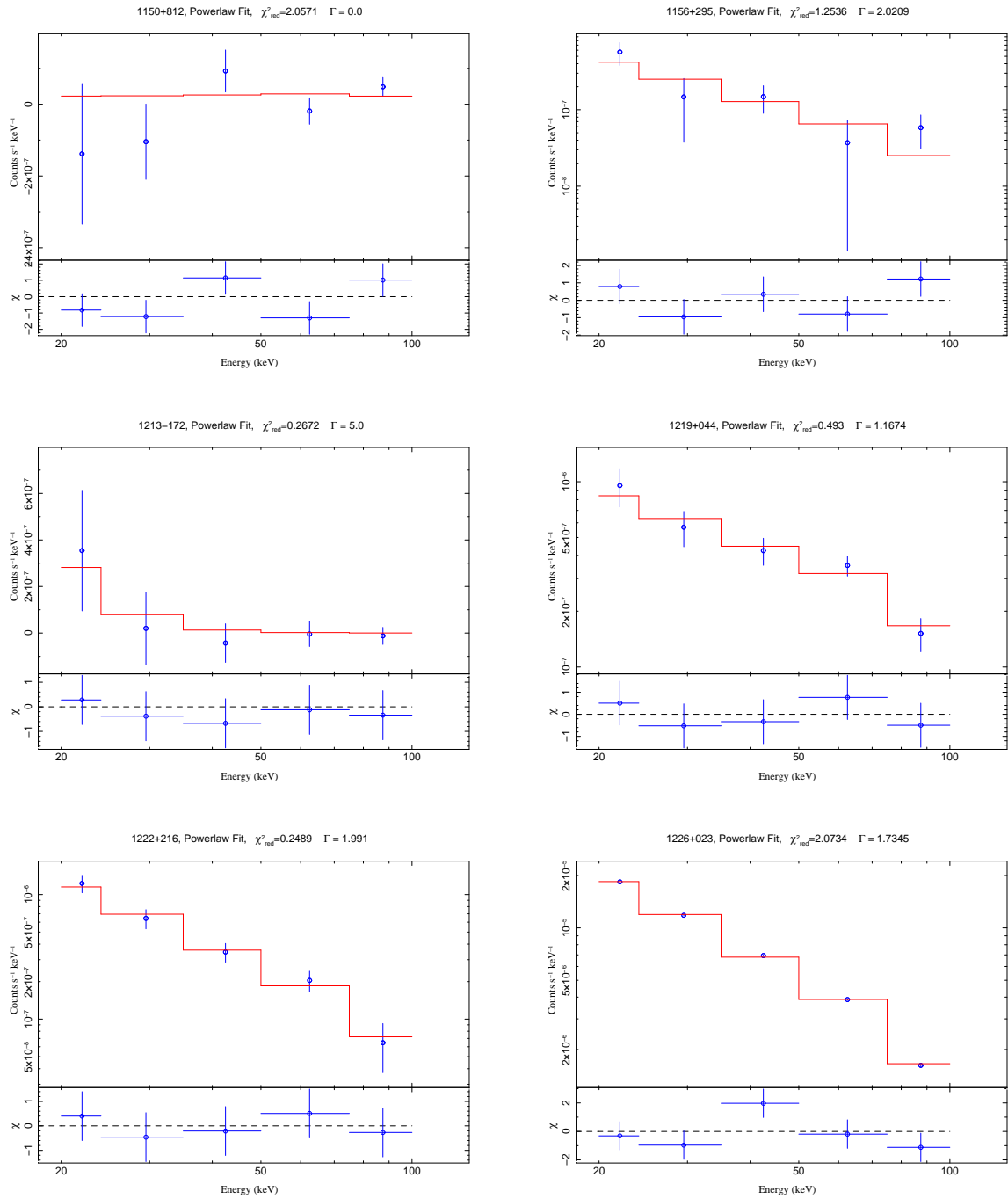


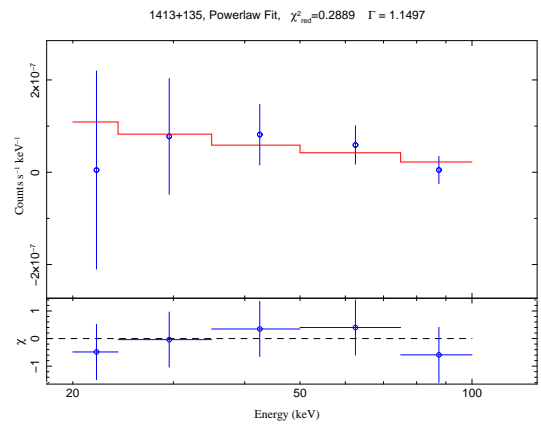
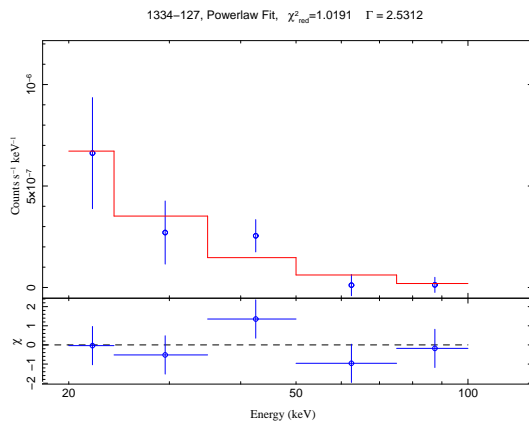
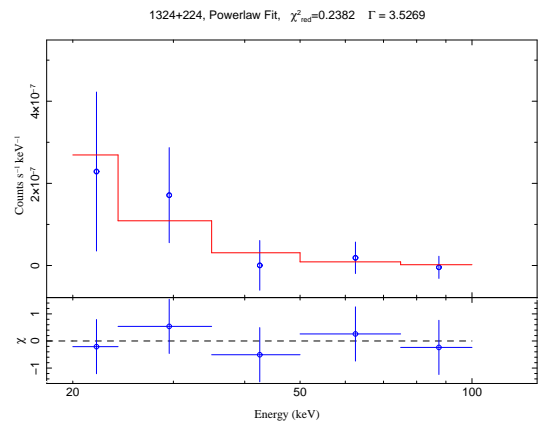
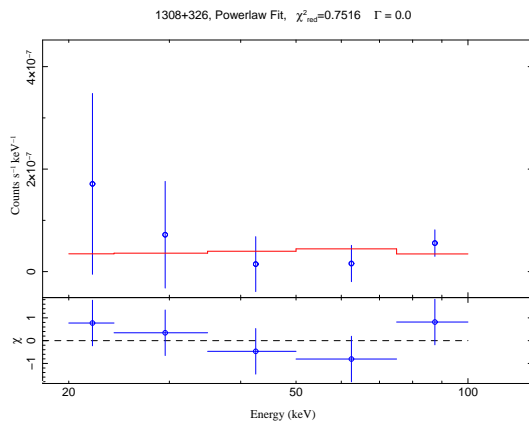
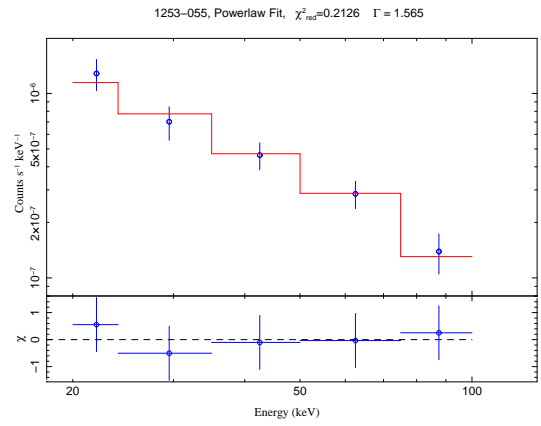
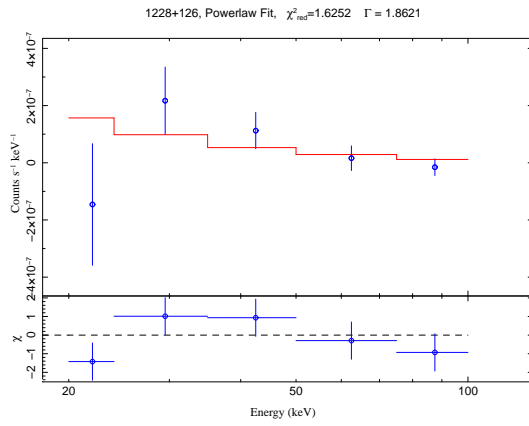


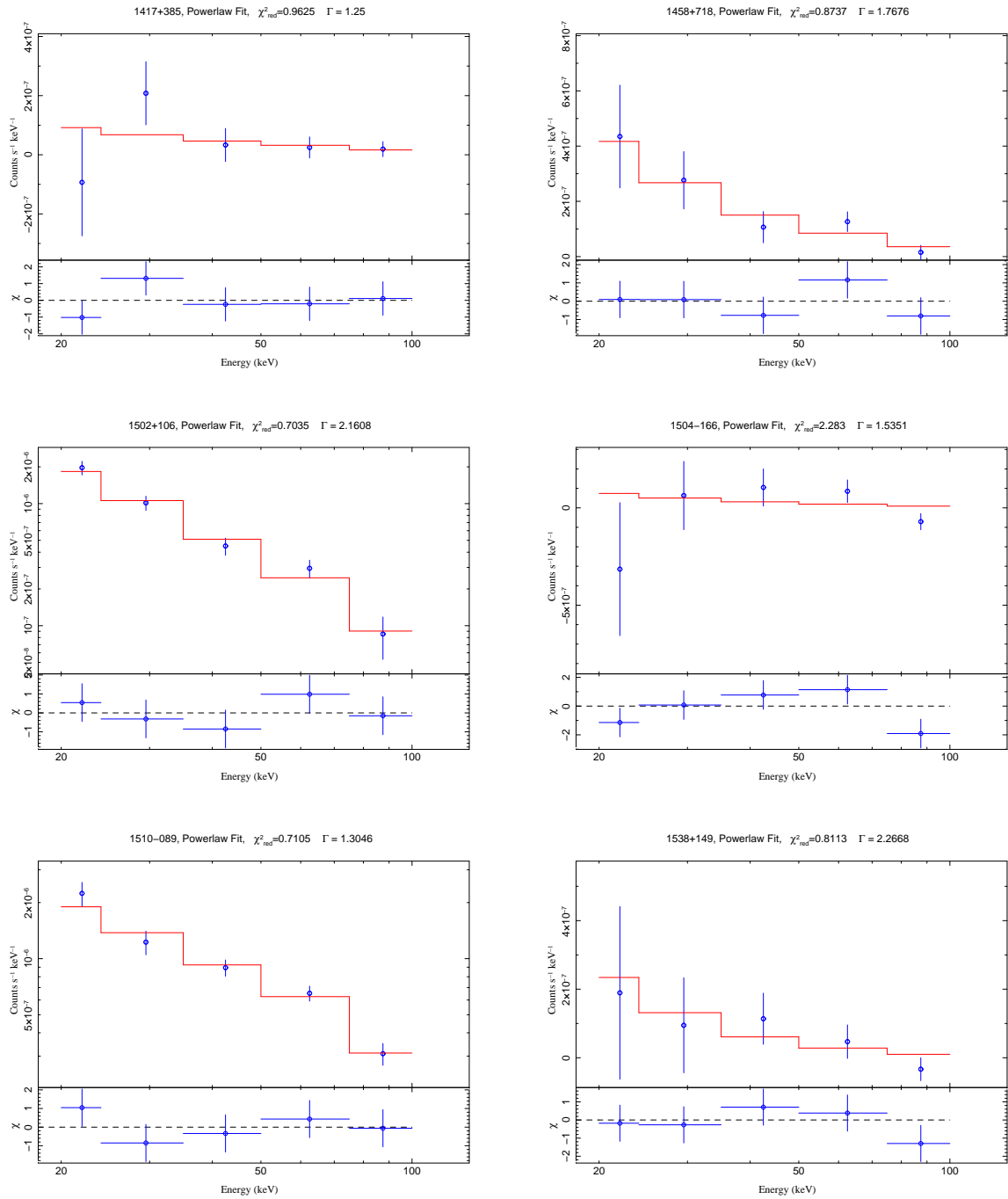


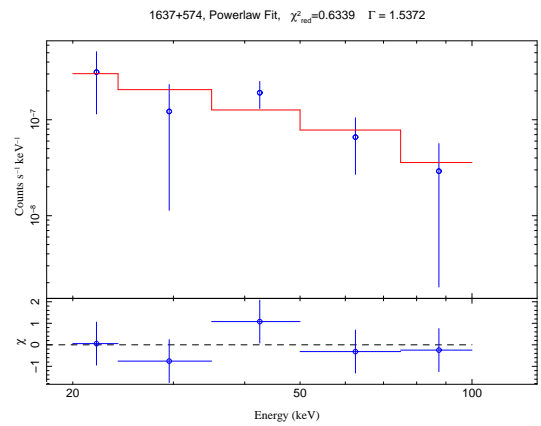
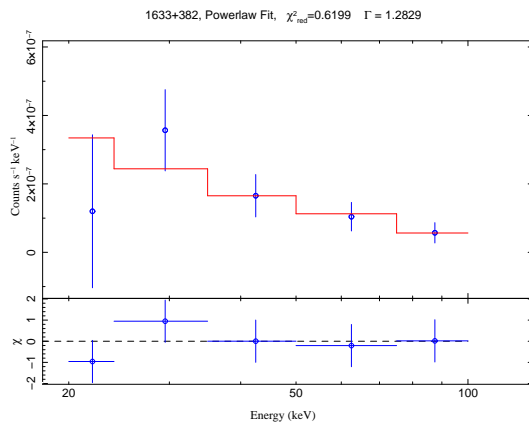
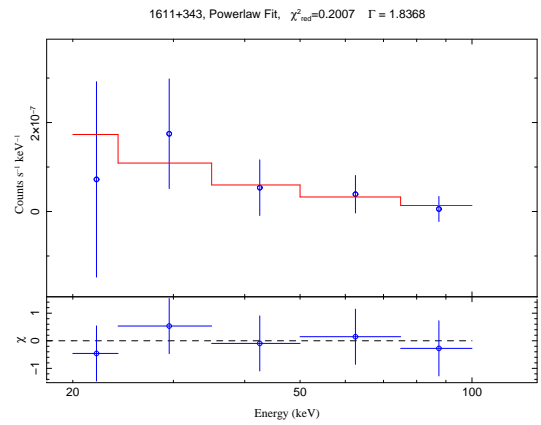
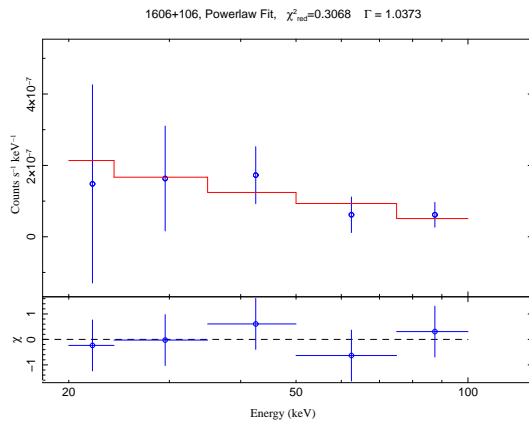
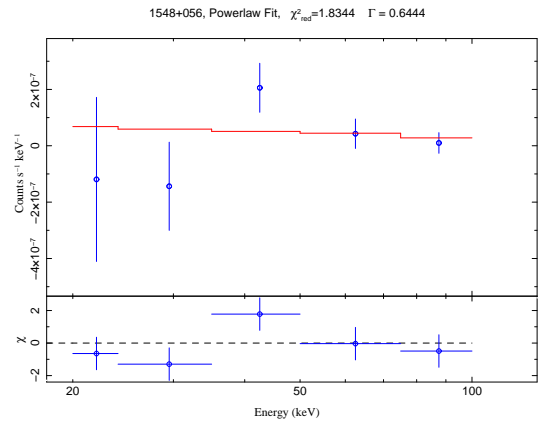
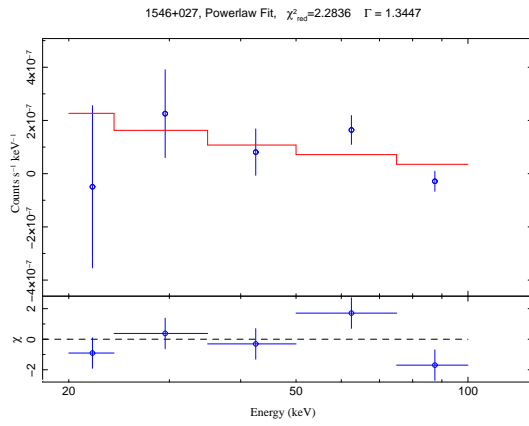


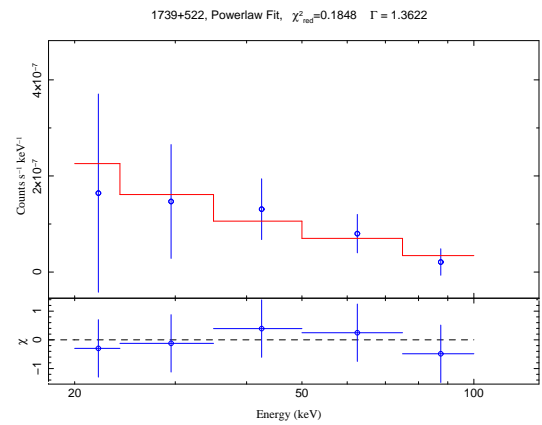
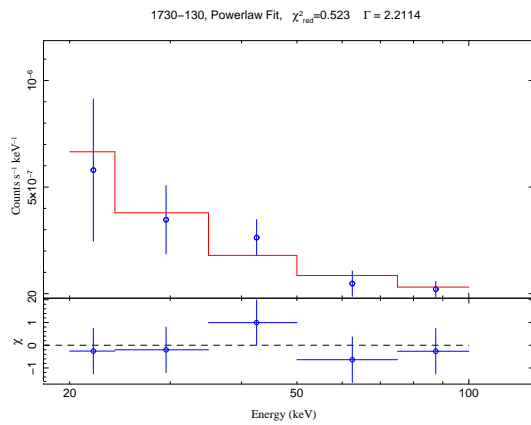
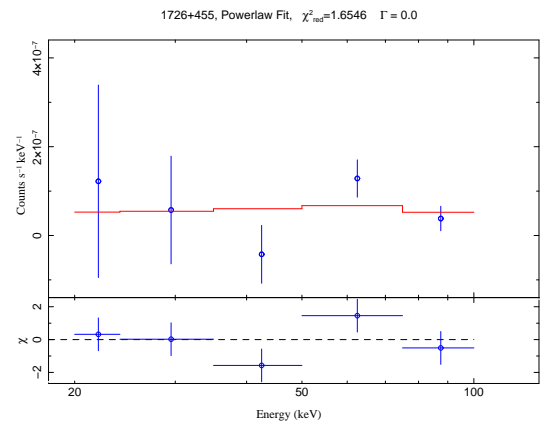
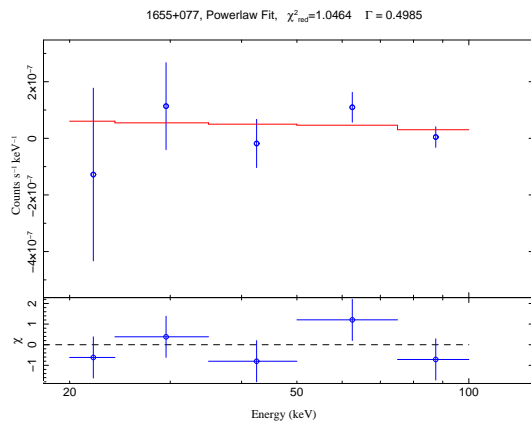
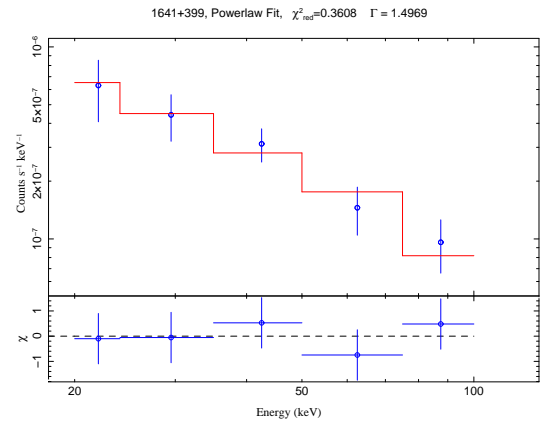
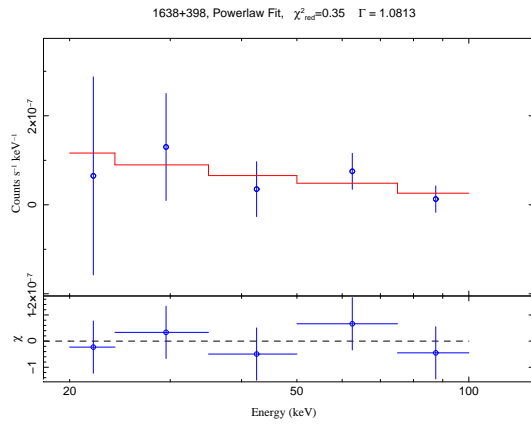


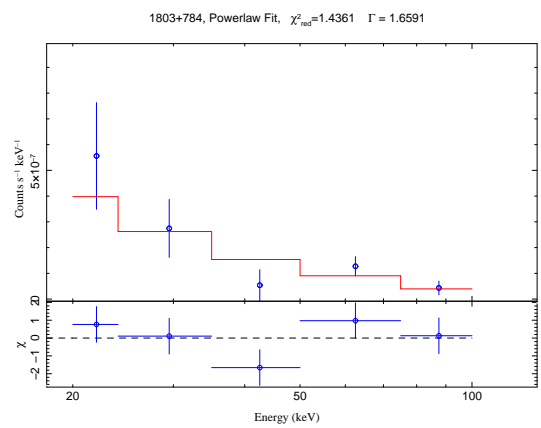
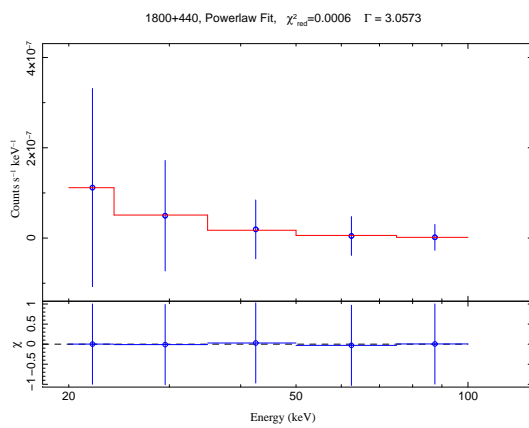
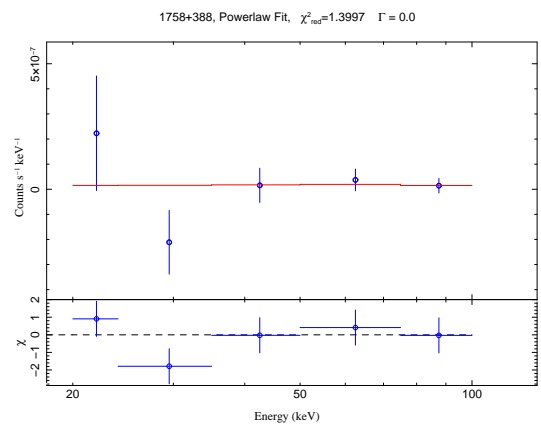
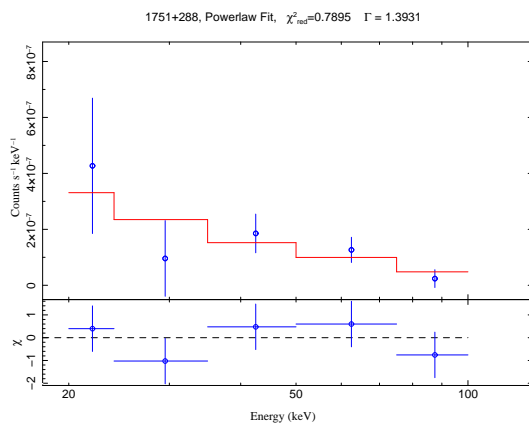
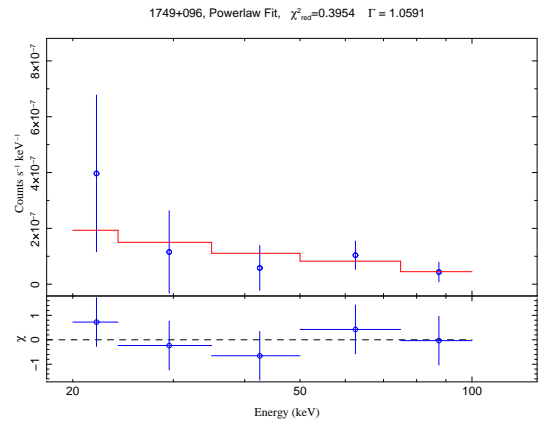
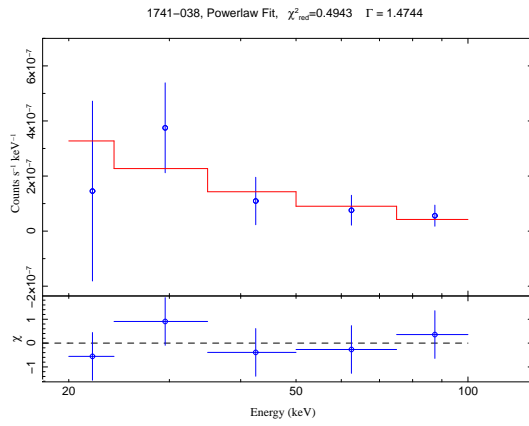


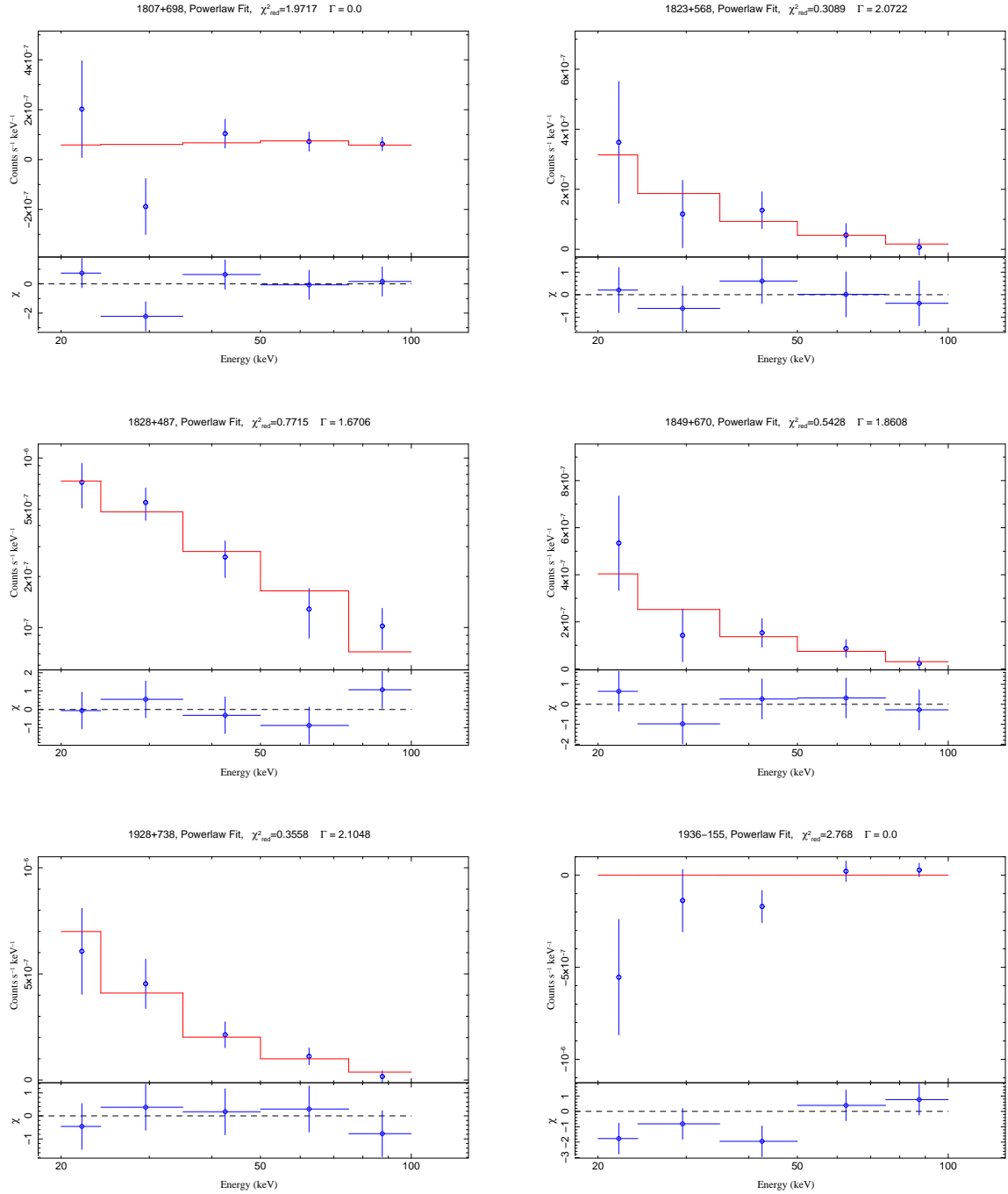


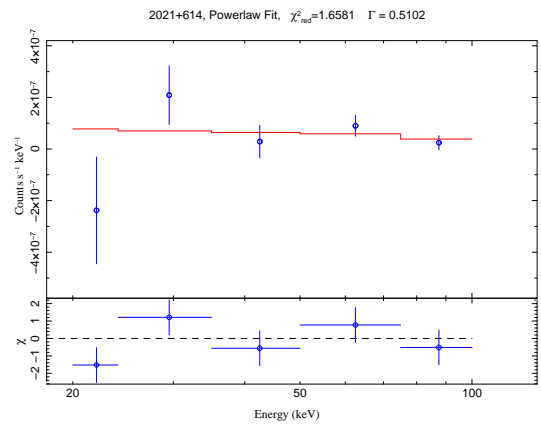
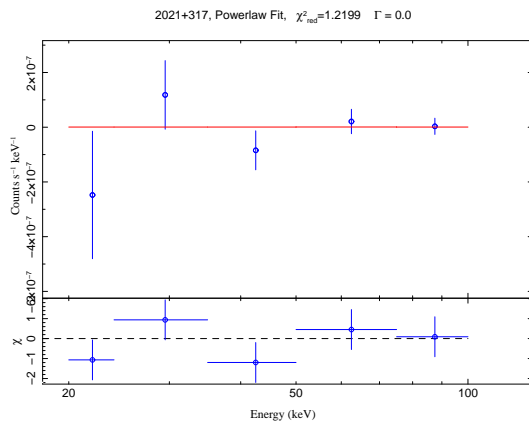
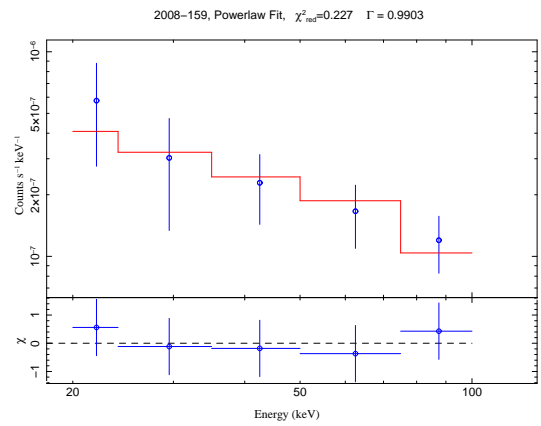
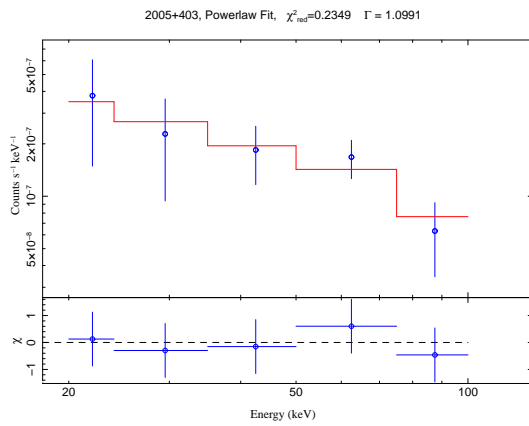
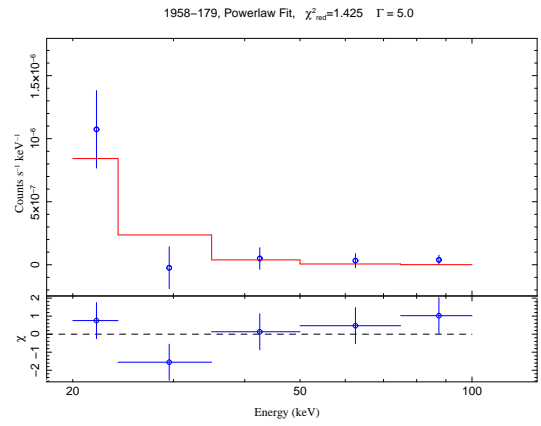
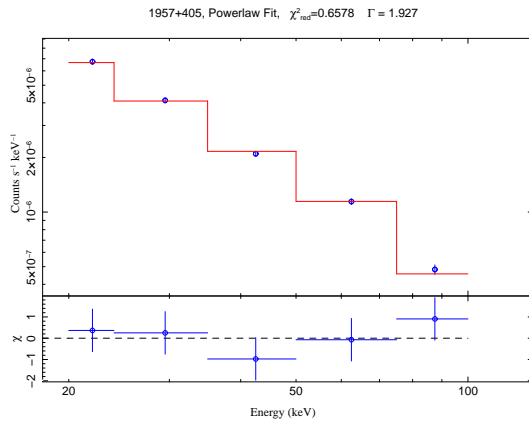


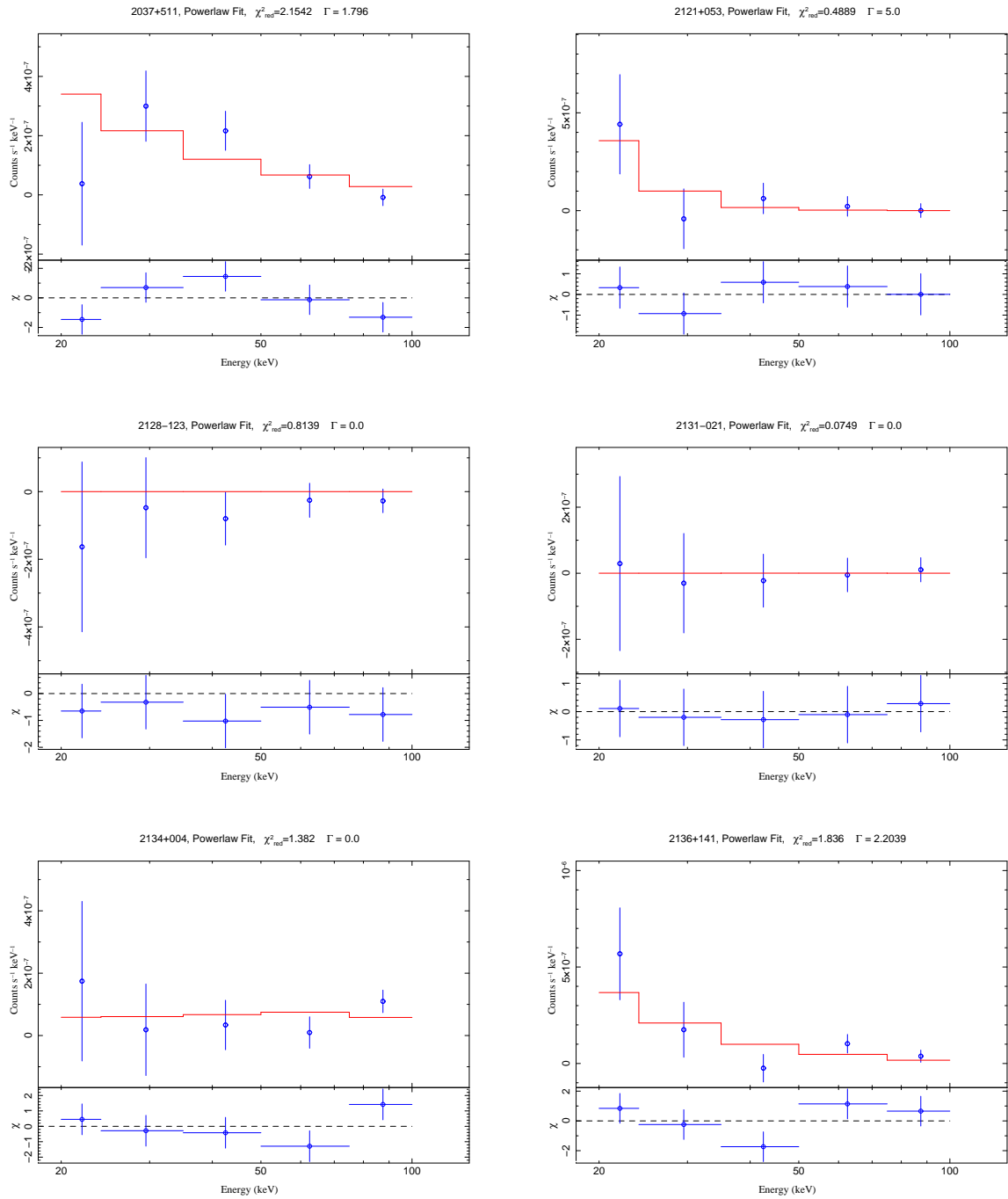


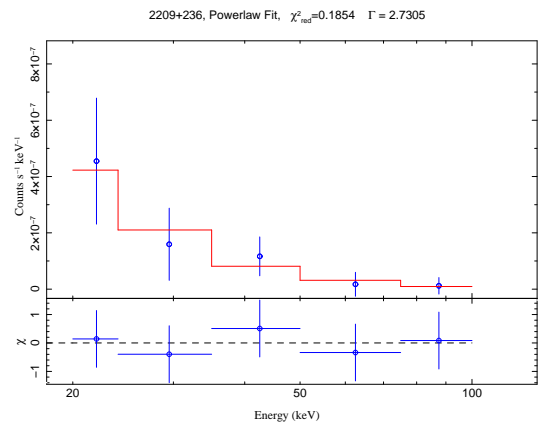
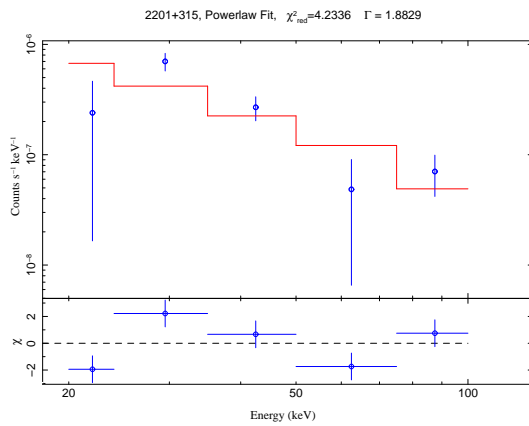
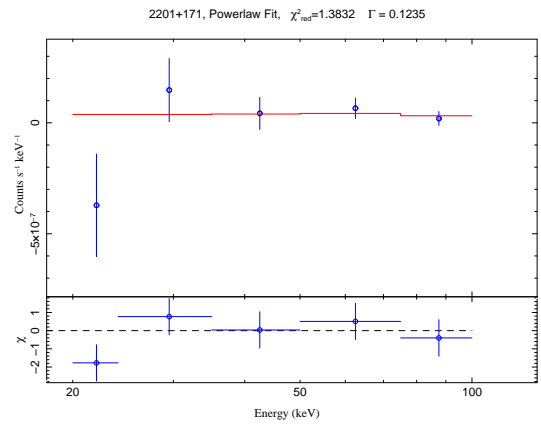
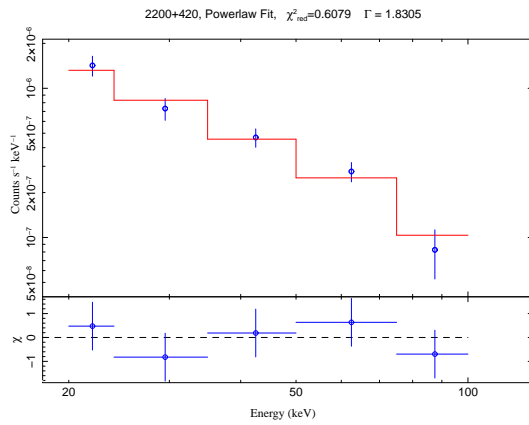
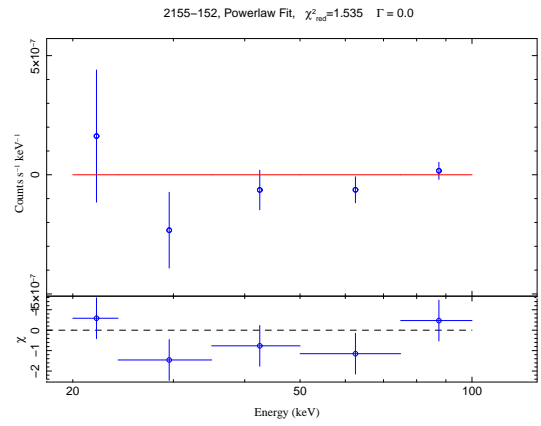
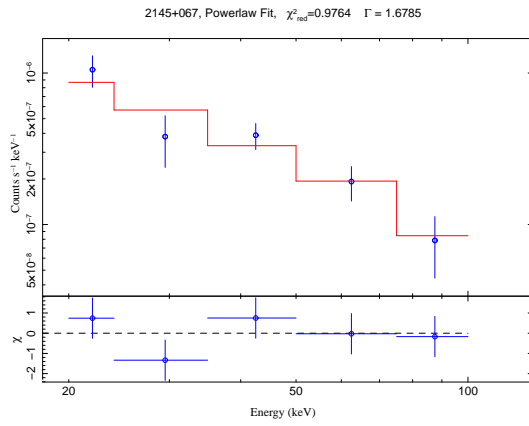




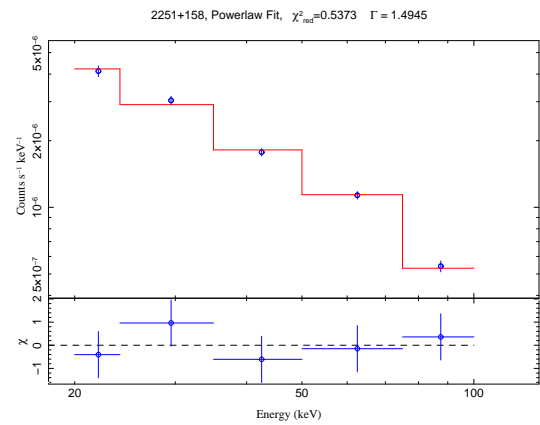
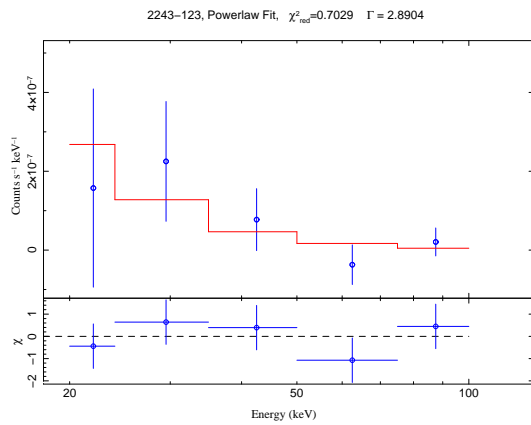
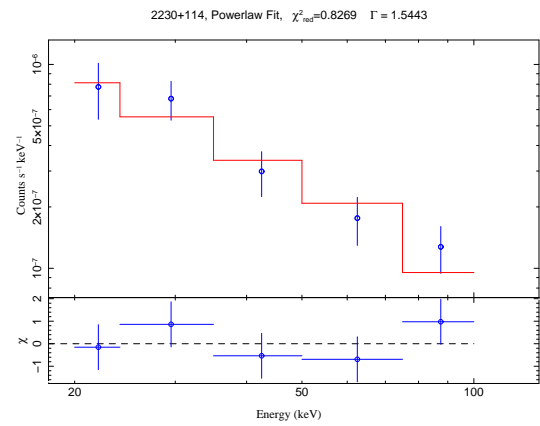
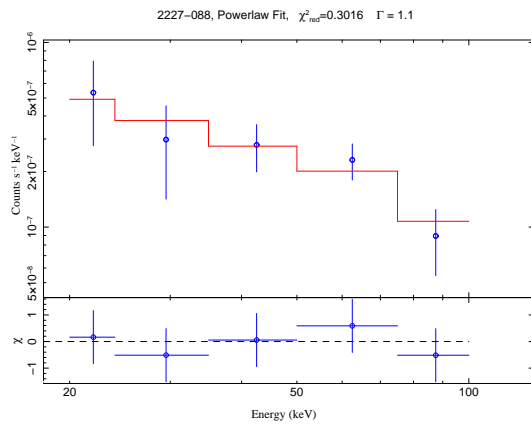
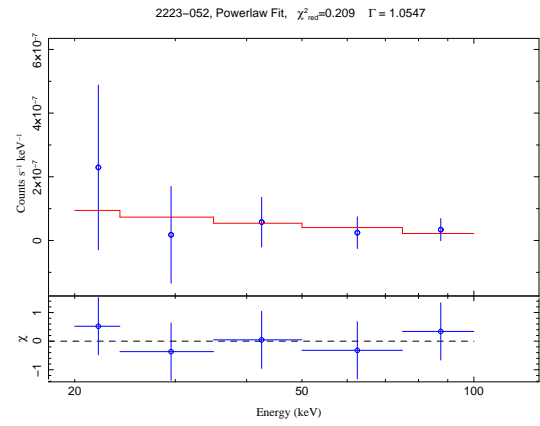
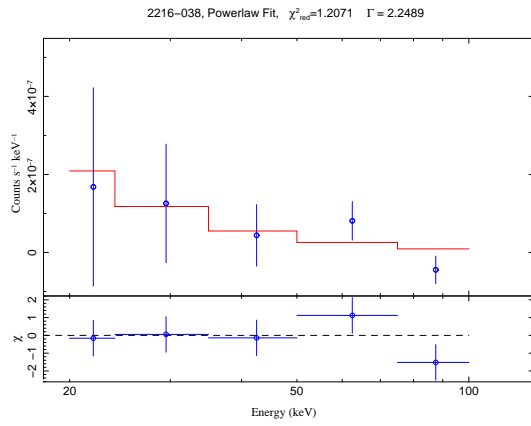


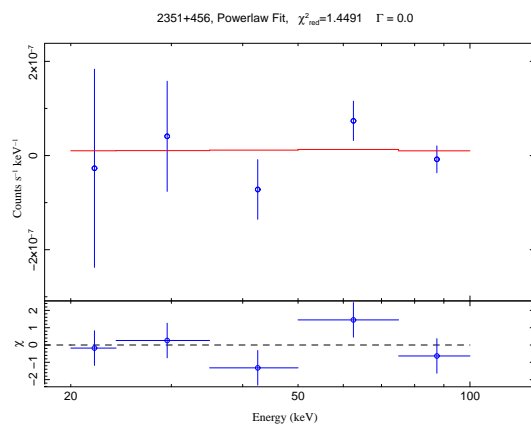
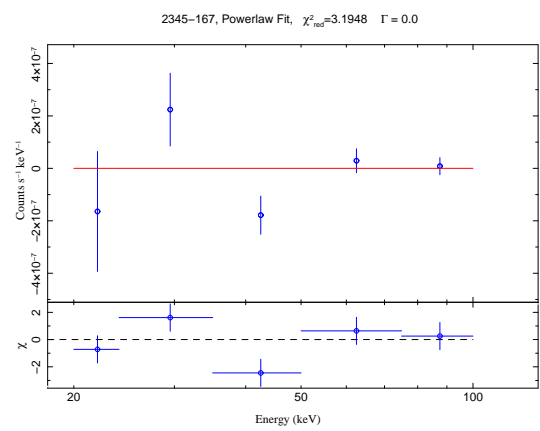
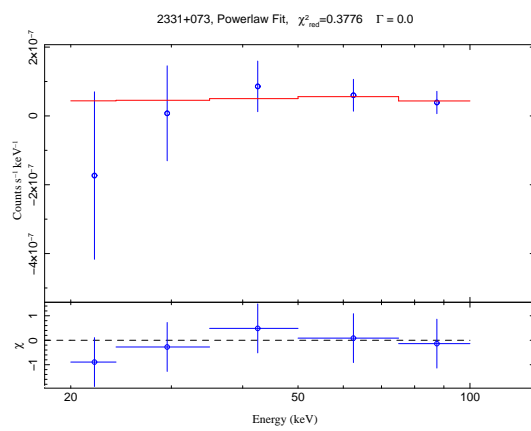






Notes. Power law fits etc....





List of Figures

1.1	The sky in Galactic coordinates	2
1.2	Photographs of NGC 4151	4
1.3	Fanaroff Riley I & II	6
1.4	Unification Model	8
1.5	Composite image of NGC 4261	10
1.6	Coded mask system principle	12
1.7	<i>Swift</i> /BAT schematic	13
2.1	Individual synchrotron spectra of electrons	16
2.2	SED of 3C273	18
2.3	SED of PKS 1510-089	19
2.4	Average blazar SEDs in different luminosity classes	20
2.5	Jet velocity vs. radio luminosity	21
3.1	Aitoff projection of 70-month BAT sources	25
4.1	Photon Index in dependence of BAT SNR	28
4.2	BAT spectrum of 2200+420 and 0607-157	29
4.3	Relation of hard X-ray flux to BAT SNR	31
5.1	Blank sky and MOJAVE-1 sample SNR distribution	36
5.2	BAT SNR distribution of MOJAVE-1 sample	37
5.3	Photon Index distribution of bright MOJAVE-1 sources	38
5.4	Hard X-ray flux distribution for bright MOJAVE-1 sources	40
5.5	Distribution of Redshift z	40
5.6	Hard X-ray luminosity distribution of the MOJAVE-1 sample	41
5.7	Relation of hard X-ray to VLBA radio flux	43
5.8	Residuals of lin. regression for X-ray vs. radio flux	44
5.9	Relation of hard X-ray to VLBA radio luminosity	46
5.10	Residuals of lin. regression for X-ray vs. radio luminosity	47
5.11	Jet velocity vs. radio and X-ray luminosity	50
6.1	Photon index of 0716+714 for XRT observations	52
6.2	Log(N)-Log(S) for radio, X-rays, gamma-rays.	55
6.3	Log(N)-Log(L) for hard X-rays	58
6.4	Photon indices of BAT vs XRT for the MOJAVE-1 sample	61
6.5	SEDs for 1FGL detected / non-detected MOJAVE-1 sources	62
6.6	Redshift distribution for 1FGL detected / non-detected MOJAVE-1 sources	63
A.1	X-ray vs. radio fluxes for the MOJAVE-1 sample	67
A.2	X-ray vs. radio luminosities for the MOJAVE-1 sample	68
A.3	Apparent jet velocity against radio luminosities	69

List of Tables

4.1	Number of optical classifications of MOJAVE-1 sources	30
5.1	Relation of X-ray to radio flux: correlation coef. and lin. regression	45
5.2	Corr. Coefficient, part. Kendall's Tau for X-ray radio luminosities	49
6.1	Results of V/V_{\max} for radio and hard X-rays	56
B.1	MOJAVE-1 sample: photon index, flux and luminosity values for 20–100 keV	72

References

- Abdo A.A., Ackermann M., Ajello M., et al., 2010a, *ApJ* 715, 429
Abdo A.A., Ackermann M., Ajello M., et al., 2010b, *ApJS* 188, 405
Abdo A.A., Ackermann M., Ajello M., et al., 2009, *VizieR Online Data Catalog* 218, 30046
Ajello M., Alexander D.M., Greiner J., et al., 2012, *ArXiv e-prints*
Ajello M., Rau A., Greiner J., et al., 2008, *ApJ* 673, 96
Akritas M.G., Siebert J., 1996, *MNRAS* 278, 919
Antonucci R., 1993, *ARA&A* 31, 473
Antonucci R.R.J., Miller J.S., 1985, *ApJ* 297, 621
Arnaud K.A., 1996, In: Jacoby G.H., Barnes J. (eds.) *Astronomical Data Analysis Software and Systems V*, Vol. 101. *Astronomical Society of the Pacific Conference Series*, p. 17
Atwood W.B., Abdo A.A., Ackermann M., et al., 2009, *ApJ* 697, 1071
Barthelmy S.D., Barbier L.M., Cummings J.R., et al., 2005, *Space Sci. Rev.* 120, 143
Baumgartner W.H., Tueller J., Markwardt C., Skinner G., 2010, *ApJS* 42, 675, submitted
Baumgartner W.H., Tueller J., Markwardt C.B., et al., 2012, *ArXiv e-prints*
Bennett A.S., 1962 68, 163
Bianchi S., Maiolino R., Risaliti G., 2012, *Advances in Astronomy 2012*
Bird A.J., Bazzano A., Bassani L., et al., 2010, *ApJS* 186, 1
Blandford R.D., Königl A., 1979, *ApJ* 232, 34
Blandford R.D., Payne D.G., 1982, *MNRAS* 199, 883
Boella G., Butler R.C., Perola G.C., et al., 1997 122, 299
Bottacini E., Ajello M., Greiner J., 2012, *ApJS* 201, 34
Brandt W.N., Hasinger G., 2005, *ARA&A* 43, 827
Burrows D.N., Hill J.E., Nousek J.A., et al., 2005, *Space Sci. Rev.* 120, 165
Casasola V., Brand J., 2010, *ArXiv e-prints*
Chang C.S., 2010, Ph.D. thesis, *Max-Planck-Institut für Radioastronomie*
Cohen M.H., Lister M.L., Homan D.C., et al., 2007, *ApJ* 658, 232
Cusumano G., La Parola V., Segreto A., et al., 2009, *VizieR Online Data Catalog* 351, 9048
Donato D., Ghisellini G., Tagliaferri G., Fossati G., 2001, *A&A* 375, 739
Fabian A.C., 2001, In: Laing R.A., Blundell K.M. (eds.) *Particles and Fields in Radio Galaxies Conference*, Vol. 250. *Astronomical Society of the Pacific Conference Series*, p. 471
Fanaroff B.L., Riley J.M., 1974, *MNRAS* 167, 31P
Feigelson E.D., Berg C.J., 1983, *ApJ* 269, 400
Fossati G., Maraschi L., Celotti A., et al., 1998, *MNRAS* 299, 433
Freyberg M.J., Egger R., 1999, *MPE Report* 278
Gehrels N., Chincarini G., Giommi P., et al., 2004, *ApJ* 611, 1005
Ghisellini G., Maraschi L., 1989, *ApJ* 340, 181
Ghisellini G., Maraschi L., Tavecchio F., 2009, *MNRAS* 396, L105
Gilli R., Comastri A., Hasinger G., 2007, *A&A* 463, 79
Giommi P., Padovani P., Polenta G., et al., 2012, *MNRAS* 420, 2899
Harrison F.A., Boggs S., Christensen F., et al., 2010, In: *Society of Photo-Optical Instrumentation Engineers (SPIE) Conference Series*, Vol. 7732.
Hartman R.C., Villata M., Balonek T.J., et al., 2001, *ApJ* 558, 583
Hasinger G., Burg R., Giacconi R., et al., 1993, *A&A* 275, 1

- Hasinger G., Zamorani G., 1997, *Exploring the Universe: A Festschrift in Honor of Ricardo Giacconi*, ed. H. Gursky, R. Ruffini, & L. Stella (Singapore: World Scientific)
- Haslam C.G.T., Salter C.J., Stoffel H., Wilson W.E., 1982
- Houck J.C., Denicola L.A., 2000, In: Manset N., Veillet C., Crabtree D. (eds.) *Astronomical Data Analysis Software and Systems IX*, Vol. 216. Astronomical Society of the Pacific Conference Series, p. 591
- Jansen F., Lumb D., Altieri B., et al., 2001, *A&A* 365, L1
- Kadler M., 2012, *Extragalactic Jets*, lecture handout
- Kanbach G., Bertsch D.L., Fichtel C.E., et al., 1988, *Space Sci. Rev.* 49, 69
- Kellermann K.I., Moran J.M., 2001, *ARA&A* 39, 457
- Kellermann K.I., Sramek R., Schmidt M., et al., 1989, *AJ* 98, 1195
- Kendall M.G., 1938, *Biometrika* 30, 81
- Kitchin C.R., 2007, *Galaxies in Turmoil - The Active and Starburst Galaxies and the Black Holes That Drive Them*, Springer, Berlin, Heidelberg
- Kovalev Y.Y., Kellermann K.I., Lister M.L., et al., 2005, *AJ* 130, 2473
- Krivonos R., Tsygankov S., Lutovinov A., et al., 2012, *A&A* 545, A27
- Krivonos R., Tsygankov S., Revnivtsev M., et al., 2010, *A&A* 523, A61
- Krolik J.H., 1999, *Active Galactic Nuclei - From the Central Black Hole to the Galactic Environment*, Princeton University Press, Kassel
- Kukula M.J., Dunlop J.S., Hughes D.H., Rawlings S., 1998, *MNRAS* 297, 366
- Laing R.A., Bridle A.H., 1987, *MNRAS* 228, 557
- Landy S.D., Szalay A.S., 1992, *ApJ* 391, 494
- Langejahn M., Kadler M., Wilms J., et al., 2013, *Hard X-Ray Properties of Blazars and Other Extragalactic Jets*, manuscript in preparation
- Lawrence A., 1987, *PASP* 99, 309
- Lind K.R., Blandford R.D., 1985, *ApJ* 295, 358
- Lister M.L., Aller H.D., Aller M.F., et al., 2009a, *AJ* 137, 3718
- Lister M.L., Cohen M.H., Homan D.C., et al., 2009b, *AJ* 138, 1874
- Lister M.L., Homan D.C., 2005, *AJ* 130, 1389
- Madau P., Ghisellini G., Fabian A.C., 1994, *MNRAS* 270, L17
- Maiolino R., Salvati M., Bassani L., et al., 1998, *A&A* 338, 781
- Malmquist K.G., 1922, *Lund Medd. Ser. I* 100, 1
- Maraschi L., Foschini L., Ghisellini G., et al., 2008, *MNRAS* 391, 1981
- Markwardt C.B., Barthelmy S.D., Cummings J.C., et al., 2007, *The SWIFT BAT Software Guide*
- Maselli A., Cusumano G., Massaro E., et al., 2010, *A&A* 520, A47
- Massaro E., Giommi P., Leto C., et al., 2009, *A&A* 495, 691
- Mitsuda K., Bautz M., Inoue H., et al., 2007, *PASJ* 59, 1
- Morgan W., 1968, *ApJ* 153, 27
- Müller C., Kadler M., Ojha R., et al., 2011, *A&A* 530, L11
- Nolan P.L., Abdo A.A., Ackermann M., et al., 2012, *VizieR Online Data Catalog* 219, 90031
- Ojha R., Kadler M., Böck M., et al., 2010, *A&A* 519, A45
- Padovani P., 2007, *Ap&SS* 309, 63
- Padovani P., Giommi P., Polenta G., et al., 2012, *ArXiv e-prints*
- Pestman W.R., 2009, *Mathematical Statistics -*, Walter de Gruyter, Berlin
- Peterson B.M., 1997, *An Introduction to Active Galactic Nuclei -*, Cambridge University

- Press, Cambridge
- Pucella G., Vittorini V., D'Ammando F., et al., 2008, *A&A* 491, L21
- Risaliti G., 2002, *A&A* 386, 379
- Roming P.W.A., Kennedy T.E., Mason K.O., et al., 2005, *Space Sci. Rev.* 120, 95
- Rybicki G.B., Lightman A.P., 1979, *Radiative processes in astrophysics*
- Salpeter E.E., 1964, *ApJ* 140, 796
- Sambruna R.M., Donato D., Ajello M., et al., 2010, *ApJ* 710, 24
- Schmidt G.D., Smith P.S., 2000, *ApJ* 545, 117
- Schmidt M., 1963, *Nat* 197, 1040
- Schneider P., 2008, *Einführung in Die Extragalaktische Astronomie und Kosmologie*, Springer DE, Berlin, 1. Aufl. 2005. korr. nachdruck edition
- Seyfert C.K., 1943, *ApJ* 97, 28
- Smith D.A., Done C., 1996, *MNRAS* 280, 355
- Tanaka Y., Inoue H., Holt S.S., 1994, *PASJ* 46, L37
- Tananbaum H., Avni Y., Branduardi G., et al., 1979, *ApJL* 234, L9
- Terashima Y., Wilson A.S., 2003, *ApJ* 583, 145
- Truemper J., 1982, *Advances in Space Research* 2, 241
- Tueller J., Baumgartner W.H., Markwardt C.B., et al., 2010, *ApJS* 186, 378
- Tueller J., Mushotzky R.F., Barthelmy S., et al., 2008, *ApJ* 681, 113
- Türler M., Paltani S., Courvoisier T.J.L., et al., 1999 134, 89
- Turner T.J., George I.M., Nandra K., Mushotzky R.F., 1997, *ApJS* 113, 23
- Ulrich M.H., Maraschi L., Urry C.M., 1997, *ARA&A* 35, 445
- Urry C.M., Padovani P., 1995, *PASP* 107, 803
- Vermeulen R.C., Ogle P.M., Tran H.D., et al., 1995, *ApJL* 452, L5
- Véron-Cetty M.P., Véron P., 2003, *A&A* 412, 399
- Wagner S.J., Witzel A., Heidt J., et al., 1996, *AJ* 111, 2187
- Weisskopf M.C., Tananbaum H.D., Van Speybroeck L.P., O'Dell S.L., 2000, In: Truemper J.E., Aschenbach B. (eds.) *Society of Photo-Optical Instrumentation Engineers (SPIE) Conference Series*, Vol. 4012., p.2
- Wilkes B., 2004, In: Richards G.T., Hall P.B. (eds.) *AGN Physics with the Sloan Digital Sky Survey*, Vol. 311. *Astronomical Society of the Pacific Conference Series*, p. 37
- Winkler C., Courvoisier T.J.L., Di Cocco G., et al., 2003, *A&A* 411, L1
- Wright E.L., 2006, *PASP* 118, 1711
- Zar J., 1972, *Journal of the American Statistical Association* 67, 578
- Zdziarski A.A., Fabian A.C., Nandra K., et al., 1994, *MNRAS* 269, L55
- Zeldovich Y.B., 1964, *Dokl. Akad. Nauk SSSR* 155, 67

Danksagung

Mein besonderer Dank gilt meinem Betreuer, Prof. Dr. Matthias Kadler, der immer sehr geduldig war und auf meine vielen Fragen zu meinem Projekt gern einging. Matthias konnte mir sein Arbeitsgebiet der Aktiven Galaxienkerne sowie die Röntgenastronomie nahe bringen und mich für dieses Gebiet interessieren, was ich nun als eine der spannendsten Bereiche moderner Astronomie sehe.

In diesem Sinne möchte ich mich auch bei Prof. Dr. Karl Mannheim dafür bedanken, dass ich Gelegenheit bekommen habe, am Lehrstuhl für Astronomie meine Diplomarbeit machen zu können.

Herzlich bedanken will ich mich auch bei meinen Arbeitskollegen und Mitstudenten Annika Kreikenbohm, Jonas Trüstedt, Robert Schulz und Till Steinbring, die stets bei organisatorischen wie fachlichen Fragen ein offenes Ohr hatten und mit denen ich eine tolle Zeit als Betreuer im Übungsbetrieb und dem Praktikum am Lehrstuhl und auch darüber hinaus hatte.

Weiterhin möchte ich gern mich für die wissenschaftliche Zusammenarbeit und Hilfe bei Eugenia Litzinger, Felicia Krauss und Cornelia Müller von der Sternwarte Bamberg / ECAP, wie auch für die fachlichen Betreuung bei Prof. Dr. Jörn Wilms, Dr. Dominik Elsässer und Moritz Böck bedanken, welche mir stets bei der Datenanalyse und praktischen Problemen beim Programmieren wertvolle Ratschläge geben konnten.

Mein Dank gilt außerdem Jack Tueller vom Goddard Space Flight Center, der mir die Röntgenspektren für meine Arbeit zur Verfügung gestellt hat.

Zuletzt möchte ich mich noch sehr bei meiner Familie und meinen Eltern bedanken, die es mir erst ermöglicht haben mein Studium auszuüben und schließlich zu absolvieren und mich jederzeit unterstützten.

Nachdem diese Wissenschaft schon immer so faszinierend für mich war, fand ich es eine großartige Erfahrung in den Prozess aktueller Forschung in der Astronomie mit eingebunden zu sein. Ich freue mich wirklich sehr, dass ich an dieser Stelle, an der ich jetzt stehe, angekommen bin, was ich ganz allein bestimmt niemals geschafft hätte.

Acknowledgements: This research has made use of data from the MOJAVE database that is maintained by the MOJAVE team (Lister et al., 2009a).